Mechanisms Underpinning Degradation of Protective Oxides and Thermal Barrier Coatings in High Hydrogen Content (HHC) – Fueled Turbines

FINAL SCIENTIFIC/TECHNICAL REPORT

Reporting Period Start Date: September 1st, 2010
Reporting Period End Date: August 31st, 2013

Principal Author

Prof. Daniel R. Mumm
Tel: (949) 824-3858; Email: mumm@uci.edu

Report Issued: June 28th, 2014

WORK PERFORMED UNDER AGREEMENT: DE-FE0004727

SUBMITTED BY
The Regents of the University of California, Irvine
5171 California, Avenue, Suite 150
University of California, Irvine
Irvine, CA 92697
DUNS: 04-670-5849

SUBMITTED TO
Patcharin Burke (Project Manager)
U. S. Department of Energy
National Energy Technology Laboratory
P.O. Box 10940, Pittsburgh PA 15236
Tel: (412) 386-7378; Email: patcharin.burke@netl.doe.gov

DISCLAIMER:

This report was prepared as an account of work sponsored by an agency of the United States Government. Neither the United States Government nor any agency thereof, nor any of their employees, makes any warranty, express or implied, or assumes any legal liability or responsibility for the accuracy, completeness, or usefulness of any information, apparatus, product or process disclosed, or represents that its use would not infringe privately owned rights. Reference herein to any specific commercial product, process, or service by trade name, trademark, manufacturer, or otherwise does not necessarily constitute or imply its endorsement, recommendation, or favoring by the United States Government or any agency thereof. The views and opinions of authors expressed herein do not necessarily state or reflect those of the United States Government or any agency thereof.

ABSTRACT

The overarching goal of this research program has been to evaluate the potential impacts of coal-derived syngas and high-hydrogen content fuels on the degradation of turbine hot-section components through attack of protective oxides and thermal barrier coatings. The primary focus of this research program has been to explore *mechanisms* underpinning the observed degradation processes, and connections to the combustion environments and characteristic non-combustible constituents. Based on the mechanistic understanding of how these emerging fuel streams affect materials degradation, the ultimate goal of the program is to advance the goals of the *Advanced Turbine Program* by developing materials design protocols leading to turbine hot-section components with improved resistance to service lifetime degradation under advanced fuels exposures.

This research program has been focused on studying how: (1) differing combustion environments – relative to traditional natural gas fired systems – affect both the growth rate of thermally grown oxide (TGO) layers and the stability of these oxides and of protective thermal barrier coatings (TBCs); and (2) how low levels of fuel impurities and characteristic non-combustibles interact with surface oxides, for instance through the development of molten deposits that lead to hot corrosion of protective TBC coatings. The overall program has been comprised of six inter-related themes, each comprising a research thrust over the program period, including: (i) evaluating the role of syngas and high hydrogen content (HHC) combustion environments in modifying component surface temperatures, heat transfer to the TBC coatings, and thermal gradients within these coatings; (ii) understanding the instability of TBC coatings in the syngas and high hydrogen environment with regards to decomposition, phase changes and sintering; (iii) characterizing ash deposition, molten phase development and infiltration, and associated corrosive/thermo-chemical attack mechanisms; (iv) developing a mechanics-based analysis of the driving forces for crack growth and delamination, based on molten phase infiltration, misfit upon cooling, and loss of compliance; (v) understanding changes in TGO growth mechanisms associated with these emerging combustion product streams; and (vi) identifying degradation resistant alternative materials (including new compositions or bi-layer concepts) for use in mitigating the observed degradation modes.

To address the materials stability concerns, this program integrated research thrusts aimed at: (1) Conducting tests in simulated syngas and HHC environments to evaluate materials evolution and degradation mechanisms; assessing thermally grown oxide development unique to HHC environmental exposures; carrying out high-resolution imaging and microanalysis to elucidate the evolution of surface deposits (molten phase formation and infiltration); exploring thermo-chemical instabilities; assessing thermo-mechanical drivers and thermal gradient effects on degradation; and quantitatively measuring stress evolution due to enhanced sintering and thermo-chemical instabilities induced in the coating. (2) Executing experiments to study the melting and infiltration of simulated ash deposits, and identifying reaction products and evolving phases associated with molten phase corrosion mechanisms; utilizing thermal spray techniques to fabricate test coupons with controlled microstructures to study mechanisms of instability and degradation; facilitating thermal gradient testing; and developing new materials systems for laboratory testing; (3) Correlating information on the resulting combustion environments to properly assess materials exposure conditions and guide the development of lab-scale simulations of material exposures; specification of representative syngas and high-hydrogen fuels with realistic levels of impurities and contaminants, to explore differences in heat transfer, surface degradation, and deposit formation; and facilitating combustion rig testing of materials test coupons.

TABLE OF CONTENTS

Abstract i

Table of Contents ii

Executive Summary iii

Report Details 1

1. *Vapor-Phase-Mediated Phenomena Associated with High pH_2O Oxidation of MCrAlX Bond Coats* 1
2. *Transient Stage Oxidation of MCrAlY Bond Coats in High Water Vapor Content Environments* 10
3. *In-situ TGO Development on NiCoCrAlY Studied by HTXRD* 18
4. *Impurity Deposition and the Corrosion, Infiltration and Phase Destabilization of TBC Top Coats* 18
5. *TBC Phase Destabilization Under Elevated Water Vapor Exposures* 23
6. *CMAF Infiltration into TBC Systems as a Function of TBC Microstructure* 27
7. *Volatility of TBC Stabilizers (Y_2O_3) in Elevated Water Vapor Environments* 28
8. *Alternative TBC Materials – Synthesis and Evaluation* 29
9. *Characterization of Alternative TBC Materials – $Sm_2Zr_2O_7$ TEC Determination by HTXRD* 30
10. *Thermal Gradient Testing and Thermo-Mechanical Behavior Modeling* 31

List of Tables 32

List of Figures 33

References 38

List of Acronyms and Abbreviations 43

Appendix: Tables 44

Appendix: Figures 47

EXECUTIVE SUMMARY

The overarching goal of this research program has been to evaluate the potential impacts of coal-derived syngas and high-hydrogen content fuels on the degradation of turbine hot-section components through attack of protective oxides and thermal barrier coatings. The primary focus of this research program has been to explore *mechanisms* underpinning the observed degradation processes, and connections to the combustion environments and characteristic non-combustible constituents. Based on the mechanistic findings of how these emerging fuel streams affect materials degradation, the ultimate goal of the program has been to advance the goals of the *Advanced Turbine Program* by developing materials design protocols leading to turbine hot-section components with improved resistance to service lifetime degradation under advanced fuels exposures.

To address possible hot-section materials stability concerns related to the use of syngas or HHC fuels, this program integrated research thrusts aimed at: (1) Conducting tests in simulated syngas and HHC environments to evaluate materials evolution and degradation mechanisms; assessing thermally grown oxide development unique to HHC environmental exposures; carrying out high-resolution imaging and microanalysis to elucidate the evolution of surface deposits (molten phase formation and infiltration); exploring thermo-chemical instabilities; assessing thermo-mechanical drivers and thermal gradient effects on degradation; and quantitatively measuring stress evolution due to enhanced sintering and thermo-chemical instabilities induced in the coating. (2) Executing experiments to study the melting and infiltration of simulated ash deposits, and identifying reaction products and evolving phases associated with molten phase corrosion mechanisms; utilizing thermal spray techniques to fabricate test coupons with controlled microstructures to study mechanisms of instability and degradation; facilitating thermal gradient testing; and developing new materials systems for laboratory testing. (3) Correlating information on the resulting combustion environments to properly assess materials exposure conditions and guide the development of lab-scale simulations of material exposures; specification of representative syngas and high-hydrogen fuels with realistic levels of impurities and contaminants, to explore differences in heat transfer, surface degradation, and deposit formation; and facilitating combustion rig testing of materials test coupons. Within these objectives, the tasks intended for the overall program included: (1) Evaluating the dynamics of TGO formation and the development of non-ideal oxides during high temperature exposure, as a function of the simulated combustion environments, with an emphasis on mechanisms affected by high water-vapor exposure; (2) Pursuing efforts to identify relevant deposit compositions to target for laboratory studies, and assess the variability in deposit-induced degradation processes due to the combustion environment and related variability in deposit behavior; (3) Building on efforts initiated previously to study TBC degradation under isothermal exposure to CMAF deposits applied to the surfaces, including comparative studies of thermo-chemical interactions and crystallization processes observed with representative alternative TBC materials and related rare-earth oxide systems; (4) Using volatilization, diffraction and spectroscopy techniques to explore the phase stability of YSZ top-coats as a function of water vapor content in the exposure environment, and (5) Continuing the development of thermo-mechanical treatments to isolate TBC microstructural effects that may be beneficial to CMAS mitigation.

In our studies of oxide growth in high water vapor environments, it has been shown that the extent of spinel formation during transient oxidation iss dependent upon the water vapor content in the exposure environment. In seeking a mechanistic explanation for this behavior, we have pursued refined experiments, focusing on quantifying the formation, volatilization and removal of spinel phases formed

during transient oxidation periods. For MCrAlX bond coats, high temperature, water-aided volatilization of oxides produced experimental artifacts in two distinct, systematic ways. First, samples with Al-depleted alloy surfaces grew large amounts of non-ideal oxides that evolved metal hydroxides, which re-deposited onto other surfaces as a function of proximity and water vapor content. Second, samples that grew a finite amount of transient spinel saw it volatilize away as a function of time and water vapor content, leaving behind a bare alumina surface. Studies of TGO development in water vapor without YSZ coatings should be undertaken cautiously, making sure that volatilization is considered along with growth. Conclusions drawn from work in the literature where volatilization artifacts were not accounted for should be reevaluated. No evidence was found that a high water vapor environment enhances the diffusion of divalent cations (e.g. Ni^{2+}) across an alumina TGO that contains REs. When volatilization artifacts were removed, taper-polish and re-oxidation experiments demonstrated that no new oxide – neither alumina nor spinel – grows on the surface of CoNi- or NiCoCrAlY TGOs. *The often-cited "Al-depletion of the bond coat" mechanism is deemed unlikely to explain spinel growth; experimental artifacts and the transient stage should be looked at more closely instead.*

In the early, transient stage of oxidation, development of MCrAlY TGO is found to be influenced by the amount of water vapor in the environment. In general, higher P_{H_2O} and P_{O_2} each promote the development of more $(Ni,Co)(Al,Cr)_2O_4$ spinel, measured by its percent area coverage of the TGO, but the most spinel coverage results from a combination of high P_{H_2O} and low P_{O_2}. These results hold for both NiCoCrAlY and CoNiCrAlY, in both the cast and sprayed morphologies. Microstructural evaluation of the same locations both before and after oxidation shows that spinel is most susceptible to grow on top of Ni/Co/Cr-rich alloy phases (notably γ), but that water vapor can enhance spinel growth on even the Al-rich β phase. When considering metastable alumina phases that evolve on the initial ramp to turbine inlet temperature, it was found that a five hour hold at 725 and 825 ^{0}C – corresponding to γ- and δ-alumina, respectively, each having a defect-spinel – resulted in appreciably more spinel coverage than the same hold at 950 or 1125 ^{0}C, which correspond to the more dense θ- and α-alumina phases. The presence of water vapor may keep alumina hydrated as it develops, thus elongating the γ- and δ-alumina stages and permitting the diffusion of spinel-forming cations to the surface. *The results have important implications for bond coat stability, TGO development and TBC durability in the high water vapor content combustion environments characteristic of syngas-fired turbines and IGCC turbine systems.*

As a core component of this program, we have explored possible routes for acceleration of hot-section materials degradation in syngas and high hydrogen content fueled turbine systems related to the formation of deposits that are molten at operating temperatures and cause corrosive degradation of TBCs. Primary outcomes of the program include (1) developing a rapid thermo-chemical compatibility test methodology, (2) examining an alternative pyrochlore (samarium zirconate) as a viable alternative to YSZ TBC systems; (and (3) *demonstrating that the TBC microstructure plays a crucial role in the kinetics of attack and coating degradation.* Isothermal tests that have been carried out to date, that the coating *microstructure* has a profound influence on the CMAS-related damage development. Whereas the APS coating has been fully infiltrated through-thickness and undergone extensive dissolution and thermo-chemical degradation, the segmented coatings show much less pronounced degradation, and only partial infiltration (partial penetration through-thickness of the coating material). Any potential for high water vapor content environments to accelerate the aging of TBC through the evolution of the t' phase to the equilibrium cubic and monoclinic phases has been assessed through Raman and X-ray spectroscopy. *Although additional verification is needed, the results generated in this program suggest an important role of fuel type on the kinetics of TBC degradation.*

REPORT DETAILS

1. Vapor-Phase-Mediated Phenomena Associated with High pH_2O Oxidation of MCrAlX Bond Coats

Background and Approach – Gas turbine engines are currently used in the production of approximately 30% of the electricity generated in the U.S. – a number that is expected to rise as the shale gas market matures – which dictates that the country's energy costs and policies will be significantly influenced by turbine efficiency and fuel. Integrated Gasification Combined Cycle (IGCC) power plants promise to improve both, as they transform coal, biomass and other carbon feedstocks into clean, synthetic gas (syngas) that can either be reprocessed into liquid fuel for use in aero turbines, or converted into electricity at the plant – via gas turbine – with ~45% efficiency and full carbon capture. From a materials standpoint, it is critical to understand how combusting syngas at IGCC turbine inlet temperatures (e.g. 1425^0C and rising) may affect degradation mechanisms of thermal barrier coating (TBC) systems that are used to protect hot section components [1]. In particular, it is important to understand how the degradation mechanisms might differ from ones associated with combusting natural gas, the conventional gas turbine fuel for which materials were originally optimized.

Higher water vapor levels in the combustion zone are one expected consequence of using high-hydrogen content fuels such as syngas. A study done by the National Energy Technology Laboratory (U.S. Department of Energy) [2] indicates that water vapor is expected to account for 12-14% of the turbine exhaust; industry use of steam injection to suppress NO_x may raise the total to 25-30%, representing as much as a four-fold increase over that derived from natural gas combustion. Results of industrial turbine field tests with MCrAlY bond coats show increased non-ideal oxide formation in the thermally grown oxide (TGO) layer when syngas is used, compared to natural gas (Figure 1) [3]. Instead of a thin (<5 μm), continuous, thermo-chemically protective α-Al_2O_3 film that forms between the metallic bond coat and the yttria-stabilized zirconia (YSZ) top coat with natural gas, a spinel-alumina bilayer presents itself with syngas. The spinel (AB_2O_4) is susceptible to cracking and associated with an unwanted volume expansion between TGO and YSZ, factors that make for a weak interface with the top coat [4]. The thicker and more continuous spinel is – it measures as thick as 30μm in Figure 1 – the greater the threat to long-term TBC stability.

Spinels are known to manifest in the so-called *transient* oxidation period, the first several hours of high temperature exposure. Phases such as Cr_2O_3, CoO and NiO grow first, before α-Al_2O_3 has fully formed, then undergo solid state reaction with alumina as it develops beneath, ultimately yielding $(Ni,Co)(Al,Cr)_2O_4$ spinels at the TGO surface [5,6]. Because the transient period is brief, spinel growth via this mechanism is limited [7-10] and therefore not expected to account for the 30μm thick domains seen in field testing.

A *steady state* mechanism (i.e. one that plays out over longer periods of time) may be responsible instead, as hypothesized by Shillington and Clarke [11] to explain similarly massive TGO spinel domains (100mm thick) observed over lengthy exposures (512 hours). They suggested that the bond coat becomes depleted of Al as alumina grows thicker, which increases the activity gradient across the TGO for other species (e.g. Ni, Co, Cr from the bond coat – or even Ti, Nb and Pd from the superalloy substrate beneath the bond cat), enough that they diffuse *through* the alumina, whereupon they participate in spinel formation. Citing that study, Maris-Sida *et al.* [12] postulated that water vapor might be responsible for enhanced divalent cation (e.g. Ni^{2+}) diffusion across the TGO by means of altering the defect structure of alumina via proton incorporation. More recently, Angle *et al.* [13] showed that water vapor enhances

inward diffusion of oxygen into α-Al_2O_3. They postulate that proton incorporation effectively converts O^{2-} species to OH^-, whose smaller size, increased polarity and decreased charge state allow it to penetrate more deeply into the ceramic along grain boundaries. At the onset of the current study, it was hypothesized that those same factors might allow α-Al_2O_3 to also accommodate larger and more negatively charged cations (e.g. 69pm radius Ni^{2+} vs. 53pm radius Al^{3+}) – the equal and opposite effect of having smaller and more positively charged OH^- anions in place of O^{2-} – thus leading to enhanced solubility. This, combined with the activity gradient from Al-depletion, might enhance diffusion to the TGO surface and subsequently promote spinel formation.

The hypothesis is tested using a taper-polishing and re-oxidation technique first developed by Tolpygo and Clarke [14] to observe steady state anion and cation flux through FeCrAlX alumina TGOs. Polishing the TGO into a wedge shape serves two purposes for NiCoCrAlX: (1) removes transient spinel from the surface, providing a fresh alumina surface on which new spinel growth may be observed, and (2) provides variable diffusion lengths across the TGO, corresponding to variable thickness along the wedge. If new spinel grows by a steady state, diffusion-based mechanism, then larger quantities of it should grow atop low wedge positions, where diffusion lengths are shortest, versus high positions, where diffusion lengths are longest. If water vapor aids cation solubility in alumina, then more spinel should also grow in wet versus dry environments. Most of the reports in the literature of TGO spinel – in *any* environment – have involved cyclic thermal exposures [12,15-17], which are useful for evaluating TBC life expectancy, but make it difficult to differentiate thermo-chemical transport processes from mechanisms dominated by thermo-mechanical effects (e.g. cracking). By eliminating transient contributions and also reducing the number of cycles to two, thereby mitigating thermo-mechanical effects, the steady state growth behavior of spinel is better isolated.

Water vapor is known to elicit anomalous behavior in TGO development [18], including but not limited to (1) changes in grain size [19,20], (2) thicker scales due to an extended transient period that delays protective oxide formation [21], (3) enhanced surface adsorption and reactions [22], (4) embrittlement from hydrogen incorporation [23-25], (5) scale cracking and delamination [26], and (6) changing transport processes within the underlying alloy [19,27].

Volatilization is another water vapor effect that has received much attention recently for its role in oxidation processes [22,28] and as a long-term degradation mechanism [29]. While the volatilization behavior of dozens of oxides have been quantified [30], there is still no data on AB_2O_4 spinels. Evaporation of Ni in the oxidation regime has long been deemed negligible for TBC-related lab experiments (due to the relatively low vapor pressure of nickel hydroxide ($Ni(OH)_2$) in that temperature range), but this current study will demonstrate that a non-negligible amount not only evolves from spinel, but also may then systematically *redeposit* elsewhere on a specimen. How this volatilization-redeposition phenomenon has played a hidden role in perpetuating the idea of steady state spinel growth, will be explained. Once the phenomenon is accounted for and mitigated, the main questions at hand – Does spinel grow at MCrAlX TGO surfaces by a steady state mechanism? Is this a long-term threat to TBC stability? – can be adequately addressed.

Experimental Methods: Oxidation Experiments – Metallic compositions (weight %) of all tested alloys are identified in Table 1. Two types of MCrAlX bond coat system were considered. One consisted of a "stand alone" bond coat that was never attached to a Ni Superalloy substrate; NiCoCrAlY-130 and CoNiCrAlY-127 bond coat powders from *Praxair, Inc.* were chill cast into ingots (150 mm long, 13 mm diameter), sectioned into discs (1mm thick) and cut into ~25 mm^2 coupons. The other system consisted of

a bond coat that was attached to a Ni Superalloy substrate; NiCoCrAlRe powder was thermally sprayed (~100 μm thick) onto the substrate (25 mm diameter, 3 mm thick) via the high velocity oxy fuel method, and the resulting button was cut into 5 mm x 5 mm coupons such that bond coat (top) and substrate surfaces (four sides and bottom) were all exposed to the oxidizing environment. For select samples from the second system, the substrate was removed via grinding and polishing to leave a ~100 μm thick "stand alone" NiCoCrAlRe bond coat. For all samples, the bond coat surface was polished flat to a 1 μm finish to eliminate surface morphology as a variable. Samples were ultrasonically cleaned in acetone, ethanol and water to degrease prior to oxidation.

Isothermal oxidation exposures were carried out for 0-300 h at 1125 °C in a sealed, environmentally controlled furnace tube. Ramp rates were fixed at 5 °C/min and the number of hours indicates the time held at temperature. A mixture of ultra-high purity N_2 (80 vol%) and O_2 (20%) gas flowed through the furnace tube at 40 mL/min, unless otherwise noted. Water vapor in the oxidation atmosphere was varied from 0 to 45 vol% by bubbling the starting gas mixture through a water bath having a controlled temperature; for 0% H_2O, the water tank was bypassed and dry gas was piped directly from the tanks into the furnace tube. To ensure that the environment had equilibrated to the desired P_{H_2O} before ramping into the oxidation regime, the furnace was first held at 150 °C for six residence times of gas flow.

For select samples, a taper-polishing and re-oxidation procedure [14,31,32] was utilized to vary diffusion lengths across a TGO. A polishing angle of less than 1° was achieved using a tripod polisher equipped with legs whose heights are adjustable on the order of microns. The amount of water vapor in the re-oxidation atmosphere ranged from 0 to 30 vol%. To ensure accurate comparisons, each taper-polished "wedge" was bisected to yield two halves with equal slopes that could be tested in separate environments. In addition to what this article refers to as the "original wedge geometry" (i.e. the geometry described by Clarke; see schematic [31]), a "modified wedge geometry" was developed here to test the effect of exposing an Al-depleted vs. Al-rich section of bond coat during re-oxidation (Figure 2). Where noted, YSZ top coats were simulated by embedding the sample in 4YSZ (ZrO_2 + 4 mol% Y_2O_3) powders and cold isostatically pressing (CIP) to achieve a 1 mm thick, 55% dense shell that encapsulated the specimen; the coatings could be mechanically removed following oxidation – without damaging the surfaces – to accommodate plan view observation. The YSZ shell does not simulate precisely the effects of a standard TBC, which is less porous and microstructurally different, but allows less direct water vapor contact with the surface than a bare specimen might.

Samples were analyzed with scanning electron microscopy (SEM) and electron dispersive spectroscopy (EDS) in plan and cross-sectional orientations; a backscatter electron (BSE) detector was used to visualize phase contrast, and a secondary electron (SE) detector to visualize morphology. Identification of phases was done by X-ray diffraction (XRD). Thin foil specimens were prepared using a focused ion beam (FIB) and SEM dual beam system with Omniprobe lift-out technology, and observed in an SEM with a scanning transmission electron microscopy (STEM) detector. Select video materials were produced in *Adobe Photoshop CS5*, using animation and transparency effects to fade from one still frame to another.

Experimental Methods: Transpiration Experiments – The general setup is a modified, combined version of the transpiration technique employed by Jacobson [33] and Stanislowski [34], and the "denuder" technique employed by Froitzheim [35]. It utilizes the principles of condensing volatile species onto a cool quartz tube, described by the former, and an easily detachable collection tube, described by the latter. The apparatus is identical to that of Froitzheim with the following modifications: (1) rather than coating

the collection tube with a chemical species, the tube is stuffed with 0.5 g of quartz wool, and (2) quartz wool is used as the flow restrictor instead of a SiC disc.

$NiAl_2O_4$ spinel powders were produced via solid state reaction of NiO and Al_2O_3 [36] at 1300 °C in dry N_2. Multiple short exposures were carried out – and powders were ground with a mortar and pestle between each – until no traces of the parent oxides could be detected by XRD. Powders were pressed into discs (13 mm diameter, 1 mm thick) and bisque fired at 1125 °C in dry air to ensure mechanical stability. Using slits cut into a ZrO_2 plate, four discs were stood upright, parallel to the gas flow. The method of gas humidification and introduction into the furnace was the same as for oxidation experiments. Water vapor content ranged from 0 to 30%, with the flow rate constant at 200 sccm and exposure times limited to 25 h. Condensed species were washed from the outlet quartz wool and condenser tube with 36.5-38.0% Assay HCl. The liquid was vacuum-filtered and distilled before analyzed for Ni content using a Thermo Scientific S4 Atomic Absorption (AA) Spectrometer. Multiple washes were performed for each experiment until the final wash yielded a signal below the AA's detection limit. Evaporation rates are reported in terms of mass loss per unit time per unit area (kg-s^{-1}-m^{-2}), factoring in the collection time and the surface area of discs.

Results and Discussion: Isothermal Oxidation – NiCoCrAlRe bond coats (with superalloy substrate attached) were exposed for 300 h at 1125 °C in 0, 15, 30 and 45% H_2O. Cross-sectional BSE micrographs (Figure 3) show a continuous alumina base layer in all environments and a top layer of spinel that is ever-thicker with increasing H_2O; the spinel sporadically dots the surface at 0% H_2O, but forms a continuous layer in all wet environments. These results corroborate literature trends of water vapor increasing spinel growth [37,38], and the copious amounts of spinel – as much as 6 μm thick at 45% H_2O – are surpassed only by Shillington and Clarke's [11] findings (100 μm in 512 h at 1121 °C).

When the superalloy substrate is not present, however, either because it has been removed from sprayed NiCoCrAlRe specimens or avoided completely with cast NiCoCrAlY specimens, the opposite effect on spinel growth is observed – *less* spinel is found on the TGO surface following wet exposures. Spinel never grows continuously across these TGO surfaces, so rather than evaluating spinel thicknesses in cross-section, it is more useful to evaluate spinel surface area coverage with plan view BSE images (Figure 4). For both specimen types, spinel is visible after 100 h exposure in 0% H_2O, but virtually absent following 100 h in 30% H_2O. The distribution of alumina and spinel is tied to the distribution of β and γ' alloy phases – fine β/γ' dispersion, characteristic of the bond coat spraying process, yields fine alumina/spinel dispersion (Figure 4a), while coarse β/γ' dispersion, characteristic of cast bond coat (Figure 4d), yields coarse α-alumina/spinel dispersion.

To better investigate the Figure 4 trend of less spinel at higher P_{H_2O}, tests were carried out on cast NiCoCrAlY specimens over a range of time and water vapor conditions. Plan view BSE images were taken at lower magnification than in Figure 4 to assess a larger surface area (400 μm x 227 μm). Multiple images from each sample set were captured and thresholded so that the coverage of alumina and spinel (measured as % area) could be quantified. For wet environments, spinel coverage is highest between 0 and 10 h – corresponding to the transient oxidation period when spinel is definitively known to grow – then diminishes with longer exposure times; for a dry environment, spinel coverage is constant with respect to time (Figure 5). The α-alumina and spinel phases were confirmed using glancing angle XRD at a 1° incident angle. On some samples, NiO grains appear nestled into patches of spinel (as in Figure 4e). This NiO area is counted as "spinel coverage" under the assumption that NiO eventually undergoes reaction with alumina to form spinel, which was observed (Figure 6a-d). Yttria grew as sub-surface pegs

in cast NiCoCrAlY specimens. Detectable with XRD, the pegs could be observed peeking through the surface in plan view images (Figure 4f) as well as in cross-section (not pictured). The pegs are typical of NiCoCrAlY bond coats with coarse dispersion of β, γ' and M,Y-rich phases [39,40].

The presence of an exposed superalloy substrate is correlated with increasing amounts of spinel at higher P_{H_2O}. The opposite is true when a superalloy substrate is absent – spinel *decreases* at higher P_{H_2O}. The contradiction may be explained by artifacts that arise via interaction of water vapor with the different specimen geometries. Spinel *accumulation* results from the volatilization of non-ideal oxides – which grow on exposed, Al-depleted superalloy substrate surfaces – and the subsequent material *redeposition*, from the vapor phase, onto the bond coat's TGO surface as spinel; higher P_{H_2O} exacerbates the process. Spinel *loss*, on the other hand, is simply material removal by water vapor-aided volatilization; no redeposition takes place because, lacking superalloy substrate, the only non-ideal oxide present is the small amount of transient spinel; given enough time, it all evaporates from the TGO surface. Evidence to support these claims will be presented in the following two sections. Once the nature of the artifacts are identified and accounted for, experiments that target the true nature of steady state TGO development in water vapor can be described.

Results and Discussion: Spinel Volatilization – Discussion of a volatilization-redeposition phenomenon must start by verifying that spinel can indeed volatilize in appreciable quantities. This is done observationally by evaluating TGO microstructure, and more directly by measuring evaporation of pre-fabricated spinel discs. For the former, cast CoNi- and NiCoCrAlY coupons were exposed to variable water vapor environments (0, 15 and 30%) first for 5 h, then again for four separate 25 h increments. After each exposure, the same locations on the TGOs were evaluated with SEM to allow for site-specific, time-lapse evaluation at high magnification. The results demonstrate that in a dry environment (Figure 6a-d), both alumina and spinel grains are unchanged, but in a wet environment (Figure 6e-h), spinel coverage decreases over time while alumina grains are unchanged. The same trends play out macroscopically – by plotting thresholded data – and are equal to those in Figure 5, but the plots are withheld due to space considerations.

One might suggest that spinel cations are leaving the surface by *internally* reincorporating into the alumina TGO, rather than by *externally* vaporizing. This possibility was tested using XRD and cross-sectional analysis. Bragg-Brentano XRD optics were used to macroscopically evaluate TGO phase composition at the beginning (5 h) and end (105 h) of the time-lapse, in both 0% and 15% H_2O. In each environment, α-alumina peaks shifted leftward with respect to time, indicating more strain in the lattice caused by increased doping. The magnitude of the shift (e.g. 0.04° 2θ for the *(104)* peak) is equivalent in a dry vs. wet environment, suggesting that doping is the same regardless of whether spinel stays on top of – or leaves – the TGO surface. No new precipitates of Ni-, Co- and/or Cr-oxides were detected in the bulk – either by XRD or cross-section analysis – when spinel left the surface, which belies expectations associated with reincorporation of spinel cations. Based on the amount of spinel coverage and thickness following the transient stage at e.g. 15% H_2O, full incorporation would require, conservatively, 2.1 mol% solubility of NiO/CoO in α-Al_2O_3, which exceeds the solubility limit (1.7 mol% at 1100 °C, 1.8 mol% at 1200 °C for NiO in α-Al_2O_3 [41]). Lacking new precipitates, it is unlikely that all surface spinel is incorporating into the bulk; it is volatilizing.

To confirm the feasibility of spinel volatility, a chart plotting the evaporation rate of Ni from $NiAl_2O_4$ pellets as a function of water vapor is provided in Figure 7. The trend indicates that heightened water vapor levels increase Ni volatility from $NiAl_2O_4$. Notably, no evaporation is detected at 0% H_2O, which

was expected since the volatile species – metal hydroxides – cannot form without the presence of hydrogen-containing species (e.g. water). These evaporation rates are low estimates of true values because a Ni residue accumulated on the inside of the reactor tube (confirmed by AA). The residue could not be completely removed, so an exact accounting of it is excluded from the reported evaporation rates. This highlights the limitation of using a quartz tube versus the Pt/Rh-lined tubes employed in more robust transpiration experiments [33,34]. While quartz is orders of magnitude cheaper than a Pt-Rh-lined tube and provided a check on observations of microstructure volatilization, the results are only qualitatively significant. Even so, the measured Ni evaporation rates here at 1125 °C and 200 sccm are the same order of magnitude (1E-11 to 1E-10 kg-m^{-2}-s^{-1}) as Cr evaporation rates measured by Froitzheim at 800 °C and 200 sccm [35], demonstrating that they are non-negligible.

The calculated vapor pressures of $Ni(OH)_2$ [42] at these experimental conditions fall in the high 10^{-9} atm range (e.g. 8.5E-9 atm at 30% H_2O), more than two orders of magnitude lower than the expected value for $Ni(OH)_2$ from NiO at 1200 °C (1.5E-6 atm), and also lower than that of $Al(OH)_3$ expected from Al_2O_3 at the same conditions (2.3E-8 atm). Given a more complete accounting of volatile species, however, it is believed that $NiAl_2O_4$ would prove to be more volatile at these conditions than Al_2O_3 and NiO. This is based on time-lapse microstructural observations of spinel evaporating while (1) Al_2O_3 remains unchanged and (2) NiO undergoes solid state reaction rather than evaporating (Figure 6). The observations must be better reconciled quantitatively using more robust transpiration experiments with Pt-Rh-lined tubes.

Results and Discussion: Spinel Redeposition from the Vapor Phase – The case for spinel redeposition from the vapor phase is made using taper-polishing and re-oxidation experiments. These were first carried out on FeCrAlZr to ensure that methods were refined to the point of being able to reproduce data in the literature [14,31,32]. Whereas new alumina grows immediately above alumina grain boundaries on cast FeCrAlZr – a function of outward Al cation flux – similar grain boundary ridges (GBRs) do not grow in equivalent experiments performed on cast CoNi- and NiCoCrAlY. GBRs are not observed in any environment – dry or wet – after any length of time, or anywhere on the wedge. Instead, spinel grains that have *no correlation to grain boundaries* grow as a function of wedge position, water vapor and, most notably, sample geometry.

Figure 8 depicts re-oxidation on both an original and modified wedge in 15% H_2O for 4 h. Plan view BSE images were captured before and after re-oxidation and are superimposed as a split-screen to show where new oxide products do or do not form. Before re-oxidation, the original and modified geometries each have a band of taper-polished TGO that is several hundred microns wide – the wedge itself. Immediately adjacent to it, the original geometry has a patch of exposed bond coat metal, which is created when the taper-polish extends below the TGO-bond coat interface; this patch of metal is removed in the modified geometry such that the wedge terminates at the edge of the sample (Figure 2). After re-oxidation, spinel grains grow on the surface of the original wedge. These can be seen at higher magnification in plan (Figure 8c) and cross-section views (Figure 9); EDS confirms spinel by demonstrating the existence of A^{2+} (Ni and Co) and B^{3+} (Al and Cr) cations in the proper 1:2 ratio for AB_2O_4 (Figure 9b). Spinel grows more densely at the bottom of the wedge and more sparsely at the top (Figure 8a). One might be tempted to ascribe this to shorter diffusion lengths across the TGO at low wedge positions – as is the case with FeCrAlZr GBRs – if not for the complete lack of spinel in the same conditions when the modified sample geometry is used instead (Figure 8b). The grain boundaries of the native alumina, seen at the surface, are merely etched (Figure 8d), with dots of Y-rich phase being the only other phase present (the Y comes from sub-surface yttria pegs and can also be seen at the wedge surface before re-oxidation).

As in Figure 4, the absence or presence of spinel is correlated directly to sample geometry, indicating that an experimental artifact – not cation diffusion through the TGO – is responsible. The source of the artifact is the patch of exposed bond coat metal. Since the polishing angle is so shallow (<1°), the exposed metal is from just beneath the TGO-bond coat interface and is thus Al-depleted (a result of alumina formation during the original oxidation step). Upon re-oxidation, it lacks enough Al to form a new, protective alumina coating and instead grows copious amounts of non-ideal oxides (identified as $(Ni,Co)(Al,Cr)_2O_4$ spinels and NiO by XRD). It is thought that the non-ideal oxides – particularly spinels – volatilize in a water vapor environment to yield metal hydroxides, a fraction of which recombine and precipitate on the wedge, via heterogeneous nucleation, as spinel. Using $NiAl_2O4$ as an example, the volatilization-redeposition reaction can be written as a reversible hydrothermal synthesis [43,44],

$$NiAl_2O_4(s) + 4\,H_2O(g) \rightleftharpoons Ni(OH)_2(g) + 2\,Al(OH)_3(g)$$

where volatilization takes place in the forward direction and synthesis in the reverse. Larger amounts of spinel redeposit at lower wedge positions because they are closer to the volatilization source (see the "dense spinel zone" immediately adjacent to the non-ideal oxides in Figure 8a) and thus have a higher concentration of metal hydroxides in the adjacent gas boundary layer. Spinel deposits preferentially along scratches on the wedge because these flaws, which may be introduced during the taper-polishing step, provide favorable heterogeneous nucleation sites.

If wedge spinel growth is indeed happening according to a volatilization-redeposition mechanism, then the presence of both water vapor and a volatilization source are required; if either or both are absent, spinel would not be expected to manifest. Figure 8b demonstrates that no spinel grows when there is water but no volatilization source. Critically, spinel also does not grow on an original wedge during a 0% H_2O re-oxidation (not pictured), despite non-ideal oxides growing above the Al-depleted zone (volatilization source); there is no water vapor to induce the volatilization, thus there can be no redeposition.

It is difficult to definitively claim a vapor phase transport mechanism when the volatilization source and redeposition landing spot are on the same physical specimen. To verify that transport is airborne, original and modified wedge specimens were positioned in the furnace with their wedges facing one another and a ~100 μm gap between them. When re-oxidized for 4 h in 15% H_2O, spinel was able to "jump the gap" and nucleate on the modified wedge in the same manner as on the self-contaminated original wedge, confirming airborne transport.

There are several other anecdotal observations of a volatilization-redeposition phenomenon in the literature that support the present claim. Zaplatynsky [45] noted volatilization of Ni, Cr and Co from TBC superalloy oxides (e.g. Cr_2O_3 and $NiCr_2O_4$ spinel) in static air at 1200 °C, and observed their ability to form Ni-, Co- and Cr-oxide vapor deposits (among others, including Nb-, Ti-, Mn-, Fe-, W- and Mo-oxides) on a nearby platinum foil collector, hinting at a redeposition mechanism. Water vapor-aided volatilization and redeposition of nickel has also been hypothesized based on observations made in solid oxide fuel cell (SOFC) [46,47] and steam-reforming catalyst [48] systems. There are four characteristics common to each case: (1) elevated temperature [all examples are above 600 ^{0}C; in this study, spinel deposits began forming on original wedges at 900^{0}C]; (2) abundant source of metal oxides, i.e. the "volatilization source"; (3) water vapor, even if only that of ambient lab environment; and (4) low flow rate [all examples are 100 sccm or less].

Flow rate is pivotal because at low flow, the gas boundary layer becomes thicker, as does the residence time of metal hydroxide species within it. A higher concentration of metal hydroxides in the gas should result in more redeposition away from the volatilization source, on surfaces otherwise not coated by spinel, where the solid-gas equilibrium is tilted in favor of forming solid. This highlights the need to be aware of volatilization-redeposition artifacts in humidified laboratory experiments, where low flow rates are likely to be used. At sufficiently high flow rates, as in many industrial turbine and SOFC applications, redeposition is likely negligible, but the volatilization rate is expected to increase as a function of gas velocity [49].

Redeposition is undoubtedly responsible for spinel deposits that increase as a function of H_2O in Figure 3. The volatilization source is the abundance of non-ideal oxides that grow on the exposed, Al-depleted superalloy substrate (e.g. Cr_2O_3 and $NiCr_2O_4$, same as those reported by Zaplatynsky [45]). Increasing P_{H_2O} accelerates volatilization and contributes to a higher metal hydroxide concentration in the gas boundary layer, resulting in enhanced redeposition and a thicker spinel layer. Removing the volatilization source, as in Figure 4, leaves only the small amount of transient spinel – present on the TGO surface – available to volatilize, and thus yields a lower concentration of metal hydroxides in the gas. After 100 h, when nearly all transient spinel is gone, the engine that drives redeposition is gone with it, and only a bare alumina surface remains (Figure 6).

Redeposition may also be responsible for the thick spinel deposits reported by Shillington and Clarke [11], whose experimental procedure meets the four criteria outlined above: (1) 1121 °C exposure temperature; (2) the TBC buttons used were subjected to a taper-polish that removed at least some of the YSZ coating, which exposed bond coat and, given that Nb, Ti and Pd were detected in the TGO, likely exposed Al-depleted superalloy substrate metal as well (this and/or the superalloy exposed via the hole drilled through the specimen, may have oxidized to provide the volatilization source, similar to Figure 3 and Zaplatynsky); (3) ambient lab humidity; and (4) a static atmosphere without a flow rate, providing the requisite thick gas boundary layer. Given these conditions, it is possible that the massive amount of spinels reported in that study – attributed at the time to steady state cation diffusion through an alumina TGO, which indeed motivated this current study – could be attributed to vapor phase redeposition instead.

To be clear, volatilization and volatilization-redeposition are not expected to play out on actual, in service TBC components, where superalloy substrates are not exposed and YSZ top coats make volatilization from – and redeposition onto – the TGO surface impossible. For laboratory observations, however, where YSZ top coats are often omitted to ease the study of TGO, precautions should be taken to account for or mitigate the phenomena. Any specimen surfaces that are or may become Al-depleted can lead to the artifact. This includes exposed superalloy (even on the bottom of a button) and areas where the TGO spalls, laying bare the Al-depleted bond coat beneath it, as might occur during prolonged cyclic oxidation experiments.

Results and Discussion: Evaluating New MCrAlY Oxide, Free of Artifacts – Understanding water vapor-related artifacts makes it possible, by mitigating them, to target true oxide growth in steady state oxidation behavior. Volatilization-redeposition is mitigated by using (1) standalone bond coats (i.e. no superalloy substrate attached), (2) the modified wedge geometry for re-oxidation experiments, and (3) 4YSZ coatings to prevent volatilization of new oxide – were it to develop – in the case of long exposures.

The result from Figure 8b hinted that new oxide will not form on the surface of the TGOs. Exposures of 100 h for the initial oxidation and only 4 h for the re-oxidation, however, might not be considered enough

time to induce sufficient Al-depletion of the alloy beneath the bond coat, or to grow new oxide, respectively. Follow-up experiments extended exposure times, increasing the initial oxidation and re-oxidation times to as many as 300 and 200 h, respectively, in dry and wet environments. The total time (500 h) was chosen to approximately equal the longest time (512 h) that Shillington and Clarke oxidized CoNiCrAlY, which resulted in a 100 μm thick top layer of spinel.

No new spinel was observed after 200 h re-oxidations in any environment (0%, 15% or 30% H_2O) on either NiCoCrAlY or CoNiCrAlY wedges. For example, Figure 10 shows that following 200 h re-oxidation in 30% H_2O – both with and without a 4YSZ coating – wedge surfaces remained composed of only the original α-alumina. The only other phase detected, 4YSZ, was present as sub-micron grains that remained sintered to wedge surfaces after the coating was detached. Note that alumina grains were etched by water vapor when the coating was omitted, but remained unetched when used, indicating that the coating blocked the type of direct water vapor contact that could also have resulted in volatilization of any new oxide. The possibility that new spinel did grow but was wiped away by volatilization before it could be inspected, is therefore unlikely, especially considering that re-oxidations for other durations (e.g. 1, 2, 4, 25 h in humid *and* dry conditions, where no volatilization is expected) do not show evidence of new spinel, either. The authors acknowledge that the simulated coatings are not an ideal replica of true TBCs in either density (55% vs. 75-85%, respectively) or microstructure (compacted powder vs. sprayed or vapor deposited powder), but being that they offer some approximation of a YSZ barrier (more so than being left bare, at the very least) and can be conveniently and cleanly detached in post-test to allow for plan view observation of the TGO surface, which is not possible with true TBCs, the results are presented as the best available demonstration of long-term re-oxidation.

Instead of ridges, *depressions* were observed at Figure 10 alumina grain boundaries, suggesting that the mode of new oxide growth for these materials is based on the inward flux of oxygen anions, not the outward flux of aluminum (or any other) cations [31,50]. Consequently, there is no expectation that thick spinel layers will naturally manifest on a TGO surface as a result of Al-depleted bond coat beneath it. This plainly contradicts Shillington and Clarke's conclusion that Al-depletion drives steady state spinel growth. Combining the results from this section with those from previous sections, it seems fair to suggest that Al-depletion only drives new spinel growth if such an alloy composition is permitted to be exposed to the environment, as with faulty specimen preparation or, quite possibly, spalled TGO. As a mechanism for problematic, natural spinel growth in a real TBC system, where top coats would necessarily prevent those scenarios, it is unlikely. MCrAlX studies that cite this mechanism as responsible for spinel growth may need to have their conclusions reevaluated, even if specimen preparation was free of the outlined pitfalls.

Concerning proton incorporation, whereas Angle *et al.* [13] suggested it may enhance inward oxygen anion penetration into an alumina body, the equal-and-opposite effect of enhancing outward divalent cation transport across an alumina TGO, as initially hypothesized in this study, cannot be similarly confirmed because there is no new oxide to evaluate. The role of reactive elements (REs, e.g. Re and Y) should not be overlooked. Tolpygo and Clarke [14] concluded in their FeCrAlX taper-polish and re-oxidation experiments that REs segregate to grain boundaries, where, depending on the species present and their relative concentrations, they control the overall flux of ions by, for example, blocking outward cation transport. Ultimately, the effects of proton incorporation on cation solubility and mobility may be present in this work to some degree, but dominant RE grain boundary blocking effects do not permit them to manifest on observable scales, rendering them negligible. (Attempting the same experiments without REs is exceedingly difficult because the scales do not stand up to taper-polishing when REs are not there

to improve TGO-bond coat adhesion.) Practically speaking, water vapor-aided proton incorporation is not expected to impact long-term TGO growth of commercial MCrAlX bond coats in any meaningful way.

The inability to grow spinel at the TGO surface by a steady state mechanism leaves the troubling 30 μm spinel domains grown in syngas field tests – under the cover of YSZ, where redeposition artifacts are not expected – as yet unexplained. Revisiting the transient stage to evaluate massive spinel development may be fruitful, however, given the trend observed in the first 5 h of NiCoCrAlY oxidation (Figure 5), where humid environments yielded considerably more transient spinel coverage than dry ones. This might offer an alternative explanation for studies that cite steady state Al-depletion, and is the subject of an ongoing study.

Conclusions – For MCrAlX bond coats, high temperature, water-aided volatilization of oxides produced experimental artifacts in two distinct, systematic ways. First, samples with Al-depleted alloy surfaces grew large amounts of non-ideal oxides that evolved metal hydroxides, which redeposited onto other surfaces as a function of proximity and water vapor content. Second, samples that grew a finite amount of transient spinel saw it volatilize away as a function of time and water vapor content, leaving behind a bare alumina surface. Studies of TGO development in water vapor without YSZ coatings should be undertaken cautiously, making sure that volatilization is considered along with growth. Conclusions drawn from work in the literature where volatilization artifacts were not accounted for should be reevaluated.

No evidence was found that a high water vapor environment enhances the diffusion of divalent cations (e.g. Ni^{2+}) across an alumina TGO that contains REs. When volatilization artifacts were removed, taper-polish and re-oxidation experiments demonstrated that no new oxide – neither alumina nor spinel – grows on the surface of CoNi- or NiCoCrAlY TGOs. The often cited "Al-depletion of the bond coat" mechanism is deemed unlikely to explain spinel growth; experimental artifacts and the transient stage should be looked at more closely instead.

2. Transient Stage Oxidation of MCrAlY Bond Coats in High Water Vapor Content Environments

Background and Approach – As discussed earlier, spinels are known to manifest on MCrAlYs in the so-called transient oxidation period, the first several hours of high temperature exposure. Phases such as Cr_2O_3, CoO and NiO grow first, before α-Al_2O_3 has fully formed, then undergo solid state reaction with alumina as it develops beneath, ultimately yielding $(Ni,Co)(Al,Cr)_2O_4$ spinels at the TGO surface [5,6]. Because the transient period is brief, spinel growth via this mechanism is observed to be limited [7-10]; conventional wisdom would not expect transient oxidation to account for 30μm thick layers seen in field testing or laboratory experiments [51,52].

Possible explanations for the surplus have been staked to long-term, steady state growth hypotheses. Since spinel is observed at the TGO surface, any such hypothesis must explain how the Ni, Co and/or Cr constituents of the bond coat might transport across the TGO, whereupon they oxidize. The most often cited mechanism postulates that Al-depletion of the bond coat leads to severe Ni, Co and Cr activity gradients that propel the species across alumina [11], but this was recently shown to be unlikely [53]. Another postulates that cracks in alumina, resulting from thermal cycling, provide the necessary short-circuit pathways for Ni, Cr and Co cations to cross the alumina layer [54], but experiments run under such conditions do not validate this mechanism [15,55-56]. Considering the efficacy of alumina as a diffusion barrier to spinel-forming cations – indeed, bond coats are specifically designed to take advantage of this property – a steady state mechanism of any kind is considered improbable.

The focus thus swings back to the transient stage. Could it be solely responsible for all spinel growth, even the most copious amounts? If the answer is yes, environmental conditions may be the key, specifically water vapor, which has been shown to increase the amount of spinel at the TGO surface of both NiCoCrAlY [12,17,37-38] and the analogous alumina-former, FeCrAlY [21]. Enhanced oxidation kinetics have been observed in the transient stage, when less dense metastable aluminas (e.g. δ, γ and θ phases) develop before later transforming into stable α-alumina, a more robust diffusion barrier. One study attempted to connect these concepts for MCrAlY, postulating that water vapor extends the transient stage, thus allowing more diffusion of spinel-forming cations to the TGO surface [38]. The conclusions were drawn from limited exposures (24 h, 0-8% H_2O) that extend past the transient stage, and on only one sample type (thermally sprayed NiCoCrAlY); additional evidence is thus needed to validate the mechanistic connections.

Such is the aim of the present study, which explores a wide range of sample types (NiCoCrAlY and CoNiCrAlY, each sprayed and cast) in a wide range of IGCC-relevant P_{H_2O} and P_{O_2} environments (10-50 vol%), using short exposures (0-5 h) that specifically target the transient stage. By emphasizing plan view microstructural analysis in addition to the more traditional cross-section analysis, the extent to which spinel covers the TGO is evaluated in terms of area coverage (i.e. amount of interfacial weakness to the YSZ), not just thickness. This allows for better insight into how environmental conditions impact the kind of extensive transient stage growth that might, in only a few hours, present a serious threat to the long-term stability of a TBC system.

Experimental Methods: Oxidation Experiments – Metallic compositions (weight %) of all materials investigated in this study are identified in Table I. Bond coat specimens were prepared from commercial powders in two ways – thermal spraying and chill casting. Spraying was conducted with *Sulzer Metco* powders using the high velocity oxy fuel method at the Forschungszentrum in Jülich, Germany; a 3 mm thick layer was coated onto – then cleanly removed from – a Ni-based superalloy substrate before being cut into 5 mm x 5 mm coupons. Chill casting of *Praxair, Inc.* powders took place at the U.S. Dept. of Energy Ames Laboratory in Ames, IA; the resulting ingots (150 mm long, 13 mm diameter) were sectioned into discs (1 mm thick) and cut into coupons also having ~25 mm^2 surface area. Ni-rich NiCoCrAlY and Co-rich CoNiCrAlY compositions were considered for each sample type. Coupons were ultrasonically cleaned in acetone, ethanol and water to degrease prior to oxidation.

Oxidation exposures were carried out for 0-100 h at 725-1125 °C in a sealed, environmentally controlled furnace tube. Ramp rates were fixed at 5 °C/min and the number of hours indicates the time held at temperature (for a "zero hour" hold, the furnace is ramped up to temperature and then immediately back down). A mixture of ultra-high purity N_2 (80 vol%) and O_2 (20%) gas flowed through the furnace tube (45 mm internal diameter) at 40 mL/min. Water vapor in the oxidation atmosphere was varied from 0 to 50 vol% by bubbling the starting gas mixture through a water bath having a controlled temperature; for 0% H_2O, the water tank was bypassed and dry gas was piped directly from the tanks into the furnace tube. To ensure that the environment had equilibrated to the desired P_{H_2O} before ramping into the oxidation regime, the furnace was first held at 150 °C for six residence times of gas flow.

YSZ top coats were not applied to specimens in this study. For short exposures, bare specimens were expected to behave similarly to coated specimens given the transparency of YSZ with respect to species that affect oxidation in dry or wet environments (e.g. O^{2-}, OH^-, H^+) [57]. Without a top coat concealing the TGO, critical analyses were possible, such as plan view imaging and site-specific comparisons of

TGO microstructure before versus after oxidation. 1125 °C was selected to represent a high-boundary temperature felt by the bond coat in an actively cooled, YSZ-coated blade at inlet turbine temperature.

Identification of phases was done by X-ray diffraction (XRD). Electron dispersive spectroscopy (EDS) and scanning electron microscopy (SEM) were used to analyze specimens in planar and cross-sectional orientations. A backscatter electron (BSE) detector was used to visualize phase contrast. Low magnification (400 μm x 227 μm) plan view BSE images were used to assess the percent coverage of non-ideal oxides (predominantly spinel) versus alumina over a large surface area; five to ten images per sample were thresholded using batch processed actins is *Adobe Photoshop CS5* to obtain percent coverage values. The magnification was selected to be as large as possible – so that each measurement could be considered representative of the overall specimen microstructure – yet still small enough to detect sub-micron-sized spinel grains. Capturing images with a pixel density of 1536 x 768 permits each pixel to effectively canvas a 0.26 x 0.26 μm area, theoretically allowing for the inclusion of spinel grains as small as 250 nm in diameter. Figure 11 provides an example of how the method quantifies microscopic coverage using a macroscopic, 400 μm horizontal field width (HFW) image. A 30 x 20 μm^2 area cropped from the low magnification image yields a coverage value within 1% of a high magnification, 30 μm HFW image of the same area.

Results and Discussion: Microstructural Observation – The "zero hour" time point was chosen for the majority of transient oxidation exposures. Past results indicated that, in wet environments with no YSZ top coat, spinel surface area coverage peaks between zero and ten hours before diminishing due to volatilization [53]. A median time point (e.g. 5 h) was not featured here, however, because it is observed that the longer samples are held at temperature, the more volatilization – itself a function of P_{H_2O} – is expected to affect the final coverage values. A zero hour hold, while not exempt from volatilization during the ramp to and from temperature, necessarily mitigates spinel loss better than a hold of any longer duration, allowing for spinel growth to be best evaluated when top coats are not present.

A comparison of dry (0%) vs. wet (15% H_2O) zero hour exposures of sprayed (rough) and cast (flat) CoNiCrAlY is presented in Figure 12. For both specimen types, a dry environment promotes sparse NiO (bright white in a BSE image) and spinel (light gray) outcrops against a backdrop of α-alumina (dark gray). A wet environment yields distinctively larger swaths of non-ideal oxide surface area coverage, which is composed mainly of spinel. Quantifying the percent area covered by each oxide phase is difficult for sprayed bond coat TGOs because the BSE detector conveys deep topographical grooves as dark areas, effectively removing them from the realm of characterization by the thresholding technique. Conversely, the flatness of polished, cast bond coats makes the entire surface area available for quantification. The ease of measurement with cast bond coats made them an attractive candidate to serve as a proxy for evaluating the more commercially-relevant sprayed bond coat behavior; the similarities in microstructural trends between the two, as seen in Figure 12, allowed this path to be pursued with more confidence.

While the coarse alloy phase dispersion inherent to cast MCrAlY is not a commercially relevant microstructure, it can be parlayed into a clear demonstration of how oxidation proceeds on each given alloy phase, by observing the same locations both before and after oxidation. This technique has been used previously to correlate transient growth of α-alumina and θ-alumina with the β and γ' phases, respectively, using a secondary electron detector to perceive topographical differences in the two oxides (Ar-O_2 environments, 6 h exposure) [58]. In the present study, the before-after technique is employed with a BSE detector instead, to differentiate alumina from spinel and other non-ideal oxides by atomic number contrast – and to correlate each with the alloy phases that gave rise to them – as a function of the

environment. Cast NiCoCrAlY, with interlocking β and γ' phases that are continuous on the order of tens of microns, and punctuated islands of M,Y-rich phase that are typically less than five microns across (Figure 12a-c), is particularly well-suited for this [phase microstructures of cast CoNiCrAlY are more finely dispersed].

As in Figure 12, the "after" micrographs in Figure 13 demonstrate a clear increase in spinel coverage with increasing water vapor content. By comparing them to the "before" micrographs, more context can be added to the observed trend. As one might expect, alloy phases that are increasingly richer in Ni/Co/Cr yield oxide products that are increasingly richer in those elements as well. At 0% H_2O, for instance, the Al-rich β phase yields α-alumina, the relatively Al-poor γ' phase yields α-alumina that is faintly dotted with spinel, and the M,Y-rich phase yields outcrops of NiO that are surrounded by spinel.

As water vapor is added, the amount of non-ideal oxide increases above each alloy phase. Al-poor γ' yields alumina that is more heavily dotted with spinel at 5% H_2O (Figure 13e) and nearly covered with spinel at 15% H_2O (Fig.3f). Al-rich β also sees an uptick in small spinel grains above alumina at 5% H_2O, and even nucleates some larger islands of spinel at 15% H_2O. In Figure 13, it can be seen that spinel not only spans β/γ' interfaces at 15% H_2O, but actually grows in the center of some larger β patches, too. Spinel spanning β/γ' interfaces is further demonstrated in Figures 14a-f, which show before-versus-after, higher magnification micrographs of locations indicated by rectangles on Figure 13. A needle-like morphology indicative of metastable alumina that has been converted to α-alumina [58] is seen above β after 0% H_2O exposure, while continuous spinel spans the interface after 15% H_2O exposure, transitioning to intermixed alumina/spinel toward the center of β.

Site specific cross-sections (Figures 14e and f) confirm that the metal phases that appear on the surface really do extend appreciably below the surface and are therefore responsible for the oxides that grow above them; that is, the presence of spinel above β at 15% H_2O is not a fluke created by, e.g., a thin layer of surface β with γ' beneath it. The β phase undergoes similar Al-depletion in both cases, indicating that the varying amounts of surface spinel produced by each environment are truly H_2O-dependent.

Figures 14g and h, showing cross-sections prepared via grinding and polishing of equivalent 0% and 15% H_2O specimens, respectively, are included to show TGO morphologies in higher resolution. Both are representative of TGO that grows above γ' phase. In either environment, the total thickness is typically between 0.5 and 1.0 μm total. A high-P_{H_2O} environment promotes an α-alumina/spinel bilayer (Figure 14h), whereas α-alumina is present as the full thickness in a dry environment, with only nano-sized grains of spinel scattered across the surface (Figure 14g).

Cross-sections demonstrate that while the surface area coverage of spinel may differ dramatically depending on the water vapor content, the *thickness* of the TGO is nearly equivalent across environments. Therefore, evaluating thickness – or mass gain, correlatively – as a function of environment, as is often done in TGO studies, does not fully capture relevant behavior. It may not even elucidate the most important mechanistic aspects of the TGO development: While understanding the effect of the exposure environment on overall oxide growth kinetics is important (as has been addressed elsewhere [38]), when one considers that TGO-YSZ interfacial weakness is a known mode of TBC failure, it is also critically important to quantify the *amount* of interface that is further compromised by the presence of spinel. Having provided spatial context to plan view BSE data in this section – both in terms of TGO thickness and alloy-to-oxide phase relationships – even lower magnification BSE images (400 μm HFW vs. the 150

μm HFW images in Figure 13) may now be thresholded into "spinel coverage" numbers as a way to evaluate a large amount of surface area across many different environmental conditions.

Note that the M,Y-rich phase sustains complete non-ideal oxide surface coverage in *all* environments, though its composition shifts from NiO to spinel as the environment shifts to higher P_{H_2O}; water vapor appears to accelerate the solid state reaction of NiO with alumina to form spinel, as Bolt *et al*. postulated [59]. M,Y-rich phase also yields the thickest bilayer oxide above it – as thick as 5 μm total, 4 μm of which is spinel – but again, the thickness itself does not vary as a function of environment. Representative images of thick TGO growing above this phase in cast alloys, often associated with reactive element-induced pegs, can be found in the previous literature [8].

Results and Discussion: Spinel Surface Area Coverage Measurements at 1125°C – Zero hour exposures for a wide range of P_{H_2O} were evaluated by the thresholding technique. Results for cast CoNiCrAlY and NiCoCrAlY are displayed in Figure 15. For each material, spinel coverage increases as a function of water vapor content before plateauing in the 15-30% H_2O range, then falling off slightly by 50% H_2O, the highest value tested. CoNiCrAlY yields more spinel coverage than NiCoCrAlY at every P_{H_2O}, likely due to its lower overall Al content (8.0 wt% versus 12.5% for NiCoCrAlY) and corresponding higher volume ratio of γ' phase in the alloy, which was demonstrated in the previous section to yield more spinel than the relatively Al-rich β phase. This result is not surprising; CoNiCrAlYs are commonly known to be the poorer option for oxidation resistance and are responsible for the most spinel-laden MCrAlY TGOs in the literature [51,52].

The same thresholding analysis was performed for TGOs grown in varying P_{O_2} (Figure 16). When there was no water vapor present in the exposure environment, increasing the amount of oxygen enhanced spinel surface coverage, modestly for CoNiCrAlY and more notable for NiCoCrAlY; a similar result for dry environments was found by Nijdam *et al*. [56], who also conducted tests on NiCoCrAlY without the cover of a YSZ top coat. In the presence of a constant, 15% H_2O environment, however, increasing P_{O_2} produced the opposite effect: *less* spinel coverage was observed at higher P_{O_2}values. The greatest amount of spinel coverage was produced at high P_{H_2O} and low P_{O_2} for both CoNiCrAlY and NiCoCrAlY. A wet environment yielded more spinel coverage than a dry environment at any P_{O_2} tested on either material.

A mechanistic explanation for water vapor- and oxygen-related effects on spinel development must be tied to the partial pressure of gas species, since alloy microstructures from specimen to specimen are nominally equivalent. In a series of papers, Nijdam *et al* [56,60] showed that the amount of spinel formation on NiCoCrAlY TGOs increases as a function of P_{O_2} by running tests over a wide range of values – 0.1Pa, 100Pa and 20% O_2. Results indicated that prior to YSZ deposition, pre-oxidation treatment of the bond coat in progressively higher P_{O_2}increased the amount of transient spinel (and, in turn, decreased lifetime). This was attributed to P_{O_2}enhancing the growth kinetics, which tipped the Al-poor γ' phase across the threshold from sustaining α-alumina development exclusively, to forming α-alumina along with appreciable amounts of spinel. While these Nijdam *et al*. studies only tested one value in the "high P_{O_2}" regime (20% O_2), the expectation for this study was that changes on the order of 5 or 10% O_2 – realistic variations in a turbine combustion zone – might likewise be significant to spinel formation on (NiCo)CrAlY alloys during transient oxidation. Figure 16 bears this out, correlating an increase in $P_{O_2}$from 10% to 50 vol% to more spinel coverage on the TGO surface.

Given that H_2O molecules dissociate into OH^- and H^+ on a TGO surface at high temperature **[61,62]**, an increase in the total amount of free oxygen (in the form of OH^-) might explain why spinel coverage

increases with higher P_{H_2O} (particularly considering that oxygen transfer to the oxide is quicker coming from H_2O than from O_2 molecules [63]). Were spinel formation a simple matter of increasing the overall moles of oxygen species in the environment, however, one would expect the most spinel to grow at the combination of peak P_{H_2O} and peak P_{O_2}; instead, when water vapor is present, the most spinel is formed at *low* P_{O_2}. This is a curious result, but has precedent in the literature. Hansel *et al* [64] found that, for some oxide dispersion strengthened chromia-forming alloys, the oxidation rate should increase as a function of P_{H_2O} at low P_{O_2}, but yield a negligible P_{H_2O} effect at high P_{O_2}. It has been suggested that a "competitive adsorption process" is at play in water vapor environments, where $H_2O_{(g)}$ strongly adsorbs early in oxidation and promotes a scale that remains highly permeable to gas species as long as a wet environment is maintained; O_2 transfer is facilitated within the scale through operation of the H_2O/H_2 couple, which accelerates oxide growth [22]. Such processes may explain the spinel growth trend in Figure 15.

It must be noted that the models discussed in the previous paragraph rely on interactive effects between H_2O and other species – O^{2-}, OH^- and H^+ – at the specimen surface. These interactions may play out when the TGO surface itself is exposed to the environment, as was the case in this study. In top-coated TBC systems, however, the dense YSZ coating is expected to eliminate the presence of H_2O molecules from directly interacting with the bond coat surface, allowing only its dissociated constituents – OH^- and H^+ – to penetrate, along with O^{2-}. There is a need, therefore, to evaluate transient spinel growth when dense coatings are in place, to determine how applicable the present results are to full TBC systems. Preliminary experiments indicate that water vapor also increases spinel coverage when a coating is in place, which suggests that the present results from uncoated specimens do have practical applicability. More rigorous studies involving TBC top coats and water vapor-aided transient spinel growth are underway.

Results and Discussion: Conditions Which Maximize Spinel Development and Lessons Learned – Cast NiCoCrAlY and CoNiCrAlY specimens may be useful for elucidating transient spinel trends as a function of environmental conditions, but lacking the roughness and fine alloy phase dispersion of commercially relevant, sprayed bond coats, it is not immediately clear if the results have practical value for real TBC systems. In particular, the polished flat specimens, which consistently yield TGO thicknesses under 5 μm, cannot duplicate the observations of worrisome, 30 μm thick non-ideal oxide layers (Figure 1) that initially prompted this study.

A bridge can be built between the fundamental and practical, however, by subjecting sprayed bond coats to conditions that yield the most spinel coverage on cast bond coats. Spinel coverage peaks: (1) for Co-rich CoNiCrAlY (Figure 15), (2) at roughly 30% H_2O (Figure 15), (3) at low P_{O_2} (Figure 16), and (4) following approximately a five hour exposure [53]. The confluence of these parameters produced the most severe example of spinel growth (Figure 17). In plan view, it can be seen that the entire TGO surface is covered by spinel (compare Figure 17a to Figure 12b); in cross-section, the thickness of spinel ranges from 1 μm to a maximum of 33 μm, which is roughly equivalent to results from syngas-based field tests (Figure 1). Significantly, 10 vol% is an average combustion environment P_{O_2} and 30 vol% represents the highest P_{H_2O} expected for IGCC turbines operated with syngas and steam addition for NO_x reduction [2]. Dauntingly, therefore, these numbers not only represent a worse-case scenario for transient spinel production in the lab, they are also commercially realistic. (For *cast* CoNiCrAlY and NiCoCrAlY, the same conditions yielded 91% (+/- 4%) and 45% (+/-3%) spinel coverage, respectively – both higher than any values in Figures 15 and 16.)

It is important to note that in Figure 17b, the thickest spinel may be the result of the cross-section slicing through the edge of a large bond coat protrusion – cutting parallel to the TGO rather than perpendicular to it – which, in a two-dimensional image, would give the appearance of a thicker layer than exists in three-dimensional reality. The same would be true for the cross-section images taken from field tests, however, which means the results here may be considered a fair duplication of Figure 1. Regardless of the thickness, however, complete spinel coverage is a troubling result for TBC stability. Also note that there is more internal oxidation and Al-depletion of the bond coat in the field test image, which indicates that particular specimen was likely run for many hours (perhaps hundreds or thousands), whereas the lab specimen presented in Figure 17 was made in less than one day, including ramp times. Based on these results – and previous results that indicate a steady state spinel growth mechanism may be unlikely [53] – transient oxidation may indeed be wholly responsible for the troubling amounts of spinel observed in TBC field tests with syngas.

Results and Discussion: Spinel Development Below 1125°C – Water vapor effects on TGO spinel are dramatic enough in the time it takes to ramp to and from 1125 °C (~7.5 h at 5 °C/min) that an examination of TGO evolution at lower temperatures is warranted. Notably, alumina transitions from its metastable phases (γ to δ to θ) to its final, stable phase (α) roughly between 600 and 1125 °C [65]. The amount of time that elapses before the onset of α-alumina may vary from study to study, depending on such factors as alloy composition, surface finish, ramp rate and environmental conditions [66].

In the present study, exposure to 1125 °C for zero hours with 5 °C/min ramp rates – in any N_2-O_2-H_2O environment tested – yielded α-alumina in post-mortem analysis, as identified by Bragg-Brentano (BB) and parallel beam (PB) XRD optics. To evaluate transient oxide phases as they grew *in situ*, high temperature x-ray diffraction (HTXRD) was used. Cast NiCoCrAlY was placed in the furnace and ramped to 600 °C at 5 °C/min. The temperature was held for one hour while a 1° glancing angle PB scan was performed; subsequent scans were taken at 100 °C increments up to 1100 °C, with one final scan at 1125 °C. The first oxide phase detected was $(Ni,Co)(Co,Cr)_2O_4$ spinel at 600 °C. Alumina followed at 1000 °C, after which the first Al-containing spinel, $(Ni,Co)(Al,Cr)_2O_4$, developed via solid state reaction before 1100 °C. By the time alumina was detected at 1000 °C, it had already transitioned to α-alumina. Metastable aluminas could not be detected with this *in situ* method below 1000 °C due to a low signal-to-noise that is both (1) inherent to the furnace used, and (2) a function of developing, metastable aluminas being textured and thin. Pole figure measurements, capable of revealing textured, metastable phases, could not be performed *in situ* with the available equipment. The HTXRD furnace also could not accommodate humid environments.

An indirect measurement of the effect of metastable alumina phases on spinel growth was therefore pursued as an alternative to *in situ* or post-mortem XRD, again utilizing the plan view thresholding technique. Cast NiCoCrAlY and CoNiCrAlY specimens were subjected to 15% and 5% H_2O, respectively (so selected because they yielded roughly similar spinel quantities in the standard 0 h tests). The furnace was ramped to and from 1125 °C at 5 °C/min, with a 5 h hold initiated at different temperatures before each ultimately was ramped to 1125 °C for an additional 0 h, then returned to room temperature. Each hold temperature was selected to represent a different stage of alumina development [65]. The expectation was that holding at different temperatures might yield varying amounts of spinel growth, a function of the diffusion rates of relevant spinel cations (Ni^{2+}, Co^{2+} and Cr^{3+}) through the different alumina crystal structures.

The most spinel coverage occurs when the samples are held at 725 and 825 °C (Figure 18), corresponding to the γ- and δ-alumina phases, respectively, which are cubic, defect-spinel structures. The spinel coverage is 10-20% less when the samples are held in the temperature regimes of the more densely packed θ- (monoclinic) and α-alumina (rhombohedral) structures, despite the general expectation that oxidation kinetics and Ni-Co-Cr diffusion should increase at higher temperature. By allowing each experiment to reach 1125 °C regardless of the hold temperature, the total exposure time was kept constant so that the time-dependent element of kinetics and diffusion could not be cited as cause for the measured results. It was also checked that an alumina/spinel bilayer exists after ramping to 725 °C then immediately back down. This confirmed that spinel coverage is not high because it is the only phase growing during low temperature holds; an alumina sub-layer exists at the start of every hold, indicating that diffusion across alumina is a constant component to spinel growth in this experiment.

Figure 19 micrographs provide visual, qualitative confirmation of the quantitative Figure 18 NiCoCrAlY data. It is clear from low magnification images (HFW = 400 μm, Figs.10a and b) that the 825 °C specimen has more non-ideal oxide on its TGO surface than does the 1125 °C specimen, owing to spinel encroaching past the original alloy's γ'/β phase boundaries, creating wider patches (as in Figure 13f). High magnification images (HFW = 15 μm, Figures 19c and d) show that even the center of the dark patches – alumina growing above the bond coat's β alloy phase – are punctuated by more spinel grains after the 825 °C hold than the 1125 °C hold. Together, the macro and micro views indicate where the 10-20% difference in spinel coverage is accounted for between the two specimens.

It is thought that denser alumina structures, formed at higher temperatures, provide a greater barrier to Ni, Co and Cr diffusion during the 5 h hold, and thus yield less spinel formation on the TGO surface. Conversely, by staging a hold at lower temperatures (725 or 825 °C) – when alumina exists as a cubic, defect-spinel structure – cations diffuse more freely through alumina and thus more readily participate in the formation of surface spinel during the transient stage.

Sohlberg **[67]** describes how water vapor prolongs the lifetime of the defect-spinel metastable aluminas (γ and δ), in particular. The phases are described as "reactive sponges" for hydrogen, which alumina can store or release to stay at equilibrium with the P_{H_2O} of the system. The α phase can be thought of as a dehydrated alumina, which becomes so as the temperature rises and water – more technically, protons – is driven from the structure's octahedral and tetrahedral interstitial sites. Therefore, the more water vapor that is present in the system, the longer the metastable phases stay hydrated and stave off formation of the denser θ and α phases. All the while, the higher diffusion rates characteristic of those phases' crystal structures permit the continued participation of Cr, Co and Ni in surface oxidation. This may be the mechanism by which water vapor promotes the growth of spinel during the transient oxidation stage.

Conclusions – In the early, transient stage of oxidation, development of MCrAlY TGO is influenced by the amount of water vapor in the environment. In general, higher P_{H_2O} and P_{O_2} each promote the development of more $(Ni,Co)(Al,Cr)_2O_4$ spinel, measured by its percent area coverage of the TGO, but the most spinel coverage results from a combination of high P_{H_2O} and low P_{O_2}. These results hold for both NiCoCrAlY and CoNiCrAlY, in both the cast and sprayed morphologies. Microstructural evaluation of the same locations both before and after oxidation shows that spinel is most susceptible to grow on top of Ni/Co/Cr-rich alloy phases (notably γ′), but that water vapor can enhance spinel growth on even the Al-rich β phase. When considering metastable alumina phases that evolve on the initial ramp to turbine inlet temperature, it was found that a five hour hold at 725 and 825 °C – corresponding to γ- and δ-alumina, respectively, each having a defect-spinel, relatively open cubic crystal structure – resulted in appreciably

more spinel coverage than the same hold at 950 or 1125 °C, which correspond to the more dense θ- and α-alumina phases. The presence of water vapor may keep alumina hydrated as it develops, thus elongating the γ- and δ-alumina stages and permitting the diffusion of spinel-forming cations to the surface. The results have important implications for bond coat stability, TGO development and TBC durability in the high water vapor content combustion environments characteristic of syngas-fired turbines and IGCC turbine systems.

3. In-situ TGO Development on NiCoCrAlY Studied by HTXRD

Approach – The development of a TGO in the transient stage of oxidation can be tracked using high temperature x-ray diffraction (HTXRD) *in situ* measurements. A 1500°C Rigaku furnace attachment was used in conjunction with a Rigaku SmartLab diffractometer. A polished, flat section of NiCoCrAlY bond coat was placed in the furnace and ramped to 600°C at 5°C/min, the same ramp rate used in all other transient oxidation experiments. The temperature was held for one hour while a 1° glancing angle scan was performed using the necessary parallel beam optics. Subsequent scans were taken at 100° increments through 1100°C, with one final scan at 1125°C.

Results and Discussion – Figure 20 is a plot of all seven scans, showing the development of oxide phases as a function of temperature. Spinel was the first phase to be detected, with three peaks emerging at 700°C. Interestingly, these peaks correspond with spinel phases that are high in Ni, Co and Cr, and lacking Al; they are denoted as $(Ni,Co)(Co,Cr)_2O_4$ in the legend (divalent Ni and Co occupy A sites of the AB_2O_4 structure and trivalent Co and Cr occupy B sites). The common picture of transient oxidation is that spinels develop via solid-state reaction of phases such as NiO and Cr_2O_3 to form $NiCr_2O_4$. Peaks for NiO, CoO and Cr_2O_3 are not detected before the spinels, and while that does not mean the solid state reaction is skipped entirely, it at least suggests the reaction has been completed well before getting to elevated temperature. Al-containing spinels do not emerge until 1100°C, just after α-alumina is first detected at 1000°C. This result adheres to the solid-state reaction premise; one would not expect Al in the spinels until the Al_2O_3 precursor has first been formed.

Discussion – These *in situ* results are a function of ambient air. At this time, the high temperature furnace has not been approved for use with a humidified environment due to concerns that water vapor will encourage the volatilization of sensitive furnace parts. If safe integration of humidity can be achieved on this HTXRD system, a comparison between wet and dry *in situ* results could be promising. The ability to track the development of different spinel phases, as done here, serves as a proxy for tracking the participation of different cations in the oxidation process. If water vapor has an effect on the diffusion and solubility of cations in oxides, as suspected, HTXRD with environmental control could provide a means to probe it.

4. Impurity Deposition and the Corrosion, Infiltration and Phase Destabilization of TBC Top Coats

Alternative fuels derived from coal gasification and conversion of biomass may also contain elevated levels of impurities. These non-combustible impurities lead to the formation of ash in the combustion gas stream and low-melting point surface deposits of non-combustible constituents. In general, it is likely that (despite the extensive efforts to clean the fuel) particulate matter and volatile species lead to sufficient levels of impurities to form hot section surface deposits and molten “CMAS” phases. CMAS refers to calcia-magnesia-alumina-silica phases that have been found to form in the hot-sections of aero-turbine engines as a result of ingestion of sand, dust, volcanic ash, etc. However, it remains an issue to determine

the proper deposit compositions to study, and to determine in what form the deposits should be put in contact with the hot section materials (TBC systems). For example, melt infiltration dynamics and thermo-chemical reactions will be different if a fully homogenized amorphous phase is put in contact with the TBC materials, as opposed to heterogeneous deposits of fully oxidized stoichiometric oxides of the deposit constituents, that then must undergo solid state reactions to form the molten phases.

As components of this program, we have explored the following in support of understanding any acceleration of hot-section materials degradation in syngas and high hydrogen content fueled turbine systems: (1) what is a representative chemistry of surface deposits, in relation to the fuel composition and impurity levels? (2) are these unique to syngas fueled IGCC turbine systems? (3) what is the susceptibility of alternative TBC materials to thermo-chemical degradation in the presence of these deposits? (4) What is the role of elevated water vapor content on these degradation phenomena? (5) what is the role of TBC layer microstructure on the CMAS-based deposit attack? and (6) are there rapid screening processes that can assist in evaluating the viability of new TBC materials under simulated IGCC engine conditions? *Another emerging theme is that volatilization, and transport of the oxyhydroxides of the CMAS cations, may be important to the ingress of CMAS elements into the TBC and the subsequent reactions with the TBC coating materials and the underlying TGO layer*. Studies are now being developed to evaluate the relative importance of these gas-phase transport mechanisms.

Approach: Fly Ash Evaluations and Determination of Relevant Deposit Compositions – Early in the project we procured a sampling of bottom ash from a coal gasification process (kindly provided by Jeff Bons, OSU) and subjected these materials to a comprehensive chemical analysis. Powder samples of the materials received were compacted and analyzed the by way of EDS analysis. The general results are shown in Tables 2 and 3. In general, the material was found to be, in general, a "CMAS" type material, but was found to have elevated concentrations of silica and iron oxide, relative to the CMAS compositions that have been reported in the literature relevant to aero-turbine propulsion systems. This opened up discussions on what constitutes a representative deposit material for syngas and HHC-fueled turbine systems. As a response, we initiated a set of discussions with industry stakeholders (OEMs) and power plant personnel, as well as leading researchers overseas, in an attempt to come to some consensus on appropriate materials to study in future efforts. The effort consisted of gathering information on the gasification process, and exploring the possible sources of fuel-based impurities in light of the gas cleanup procedures that are used. In general, it was determined that, despite the extensive efforts to clean the fuel, particulate matter and volatile species lead to sufficient levels of impurities to form hot section surface deposits and molten "CMAS" phases. However, it remains an issue to determine the proper deposit compositions to study, and to determine in what form the deposits should be put in contact with the hot section materials (TBC systems). For example, melt infiltration dynamics and thermo-chemical reactions will be different if a fully homogenized amorphous phase is put in contact with the TBC materials, as opposed to heterogeneous deposits of fully oxidized stoichiometric oxides of the deposit constituents, that then must undergo solid state reactions to form the molten phases. Despite these questions, several deposit compositions have emerged as important to perform baseline studies of how syngas-based CMAS (or "CMAF", as it is rich in Fe) interacts with existing and alternative TBC materials in high water vapor content environments.

Results & Discussion: Relevant Fly Ash Deposit Synthesis – As a result of this initial exploration, representative compositions of CMAS-based compositions were developed for use in the following components of the research program. The resulting glass frits will then be used in subsequent studies of thermo-chemical interactions with TBC materials. As a result of the sabbatical visit to the

Forschungszentrum Jülich, the PI has had the opportunity to "compare notes" with European researchers, and use these discussions to refine thoughts on what constitutes relevant deposit chemistries and thermo-chemical reaction studies. One primary theme that is emerging is that IGCC systems and turbines operating with syngas or HHC fuels are likely to see deposits that have significant concentrations of Fe, an smaller quantities of Si, than what is typical for aero-turbine propulsion system studies. The composition shown in Table 4 has emerged as perhaps a 'representative' CMAS composition (or "CMAF", as it is rich in Fe) to perform baseline studies of alternative TBC materials with. This composition was then synthesized through both solid-state approaches and wet-chemical synthesis routes, for use in subsequent studies of thermo-chemical interactions with TBC materials.

Approach: Thermo-Chemical Reaction Screening Tests – As another component of our efforts to better understand the formation of deposits and their thermochemical and thermo-mechanical impacts, we developed a rapid materials screening process and utilized this method to quantitatively examine the thermo-chemical reactions taking place at the TBC/deposit interfaces. The general idea is to form a porous compact of a candidate material, which is then machined to have a central hole into which CMAS is deposited. The pellet is then exposed to high temperatures to allow for melt infiltration and thermo-chemical reactions. The pellet is then sectioned and examined using imaging, chemical mapping, microanalysis and spectroscopy techniques to assess the mechanisms and extent of reaction with the infiltrating material.

Results & Discussion: Thermo-Chemical Reaction Screening Tests – We screened a number of oxides, some of which have clear potential as alternative TBC materials, and others which have shown interesting high temperature properties and may elucidate new thermo-chemical reaction behavior. The oxides span across the flourites, pyrochlores, and perovskites, and include such things as mullite, monazite (APO_4), and co-doped zirconates. The study materials were made by solid-state synthesis routes, and were evaluated for structure and composition by XRD analysis. For example, the diffraction patterns obtained for synthesis of $Gd_2Zr_2O_7$ and $(GdYb)Zr_2O_7$ are shown in Figure 21, confirming that the desired phases were successfully synthesized with the solid-state reaction having run to completion without secondary phase formation. To study thermo-chemical reactions between these oxide ceramics and a baseline CMAS composition, porous compacts of each material were prepared by procedures outlined above, but described in more detail here. Pressed pellets of each material were bisque-fired (2 hours at 1050°C) to achieve consolidated bodies with approximately 60% relative density. These pellets were then prepared with the center hole, which was then filled with 8 grams of the CMAS powder. The pellets were then exposed to isothermal heat treatment at 1300°C for 4 hours, to allow for thermo-chemical reaction between the pellet materials and the molten CMAS. Upon cooling, the pellets were cross-sectioned and metallographically prepared for microstructural and micro-chemical analysis. Typical cross-sections of the rough-sectioned materials, showing various reaction zones are illustrated in Figures 22.

Building upon the efforts initiated in the previous reporting period, we have continued to examine the interactions of a model CMAS composition with select TBC materials, both YSZ and alternative candidate materials. For instance, cross-sections of the interaction zone of CMAS exposure of mullite materials (also heavily considered as a EBC component) are illustrated in Figure 23. The corresponding Energy Dispersive Spectroscopy (EDS) maps of cross-sectional chemistry is shown in Figure 24. Interfacial reaction is extensive, but involves extensive crystallization of the molten phase – with formation of anorthite crystals. Such crystallization may be beneficial to hot-section coating stability, as it prevents further penetration and infiltration into the coating. Anorthite ($CaAl_2Si_2O_8$) crystals formed in the reaction zone, and delamination cracks are observed. These observations are the basis for developing

a mechanistic understanding of interfacial reactions and the materials basis for mitigating extensive infiltration of molten phases and the ensuing thermo-chemical and thermo-mechanical damage processes. Equivalent observations of interfacial reaction zones between CMAS and (a) $Gd_2Zr_2O_7$ and (b) $GdYbZr_2O_7$ are shown in Figure 25 and Figure 26, respectively. Quantitative analysis of the interfacial reaction zones, and general material responses, are described below.

Approach: Thermochemical Interactions Between TBC-Relevant Oxides and CMAS – As another component of our studies focusing on the formation of deposits and their thermochemical impacts, we have utilized the rapid screening technique described above to quantitatively examine the thermo-chemical reactions taking place at the TBC/deposit interfaces for a number of candidate alternative TBC and/or model oxide systems. For each candidate material, single-cation oxides were mixed and ball-milled in ethanol for 24 hours. For instance, in synthesizing $GdYbZr_2O_7$, Gd_2O_3, ZrO_2, and Yb_2O_3 were mixed and ball milled to form the starting powder mixture for solid-state synthesis. Oxide pellets were then pressed in a cold isostatic press to 45,000 psi to achieve a relative density of 60%. The pressed pellets were bisque-fired for 2 hours at 1050°C so that they could be drilled. The pellets were drilled with a 3-mm, titanium-carbide drill bit to allow placement of the CMAS within the pellet. The drilled pellets were then sintered with CMAS at 1300°C. The sintered pellets were cross-sectioned using a slow-speed diamond saw, embedded in epoxy, and ground down to 1 micron using diamond-lapping films. The polished mount was then sputter coated with *Ir* and quantitative EDS was performed at 15 kV and 2.4 nA.

Results: Thermochemical Interactions Between TBC-Relevant Oxides and CMAS – Examining one of the subject oxide materials ($GdYbZr_2O_7$), we can explore the details of CMAS interactions as follows. Figure 27 shows a BSE image of the attack of $GdYbZr_2O_7$ (GYZO) by CMAS and the corresponding qualitative EDS maps. The major CMAS constituents *Ca* and *Si* appear to come to a clear stopping point within the GYZO. *Mg* and *Al* appear to go past the penetration stopping point of *Ca* and *Si* in the GYZO. However, this is unlikely as the minor constituents should not be present in the GYZO past the point of the *Ca* and *Si* penetration. Upon closer examination of the energy spectrum, the energy lines of *Mg* and *Al* actually overlap with *Gd* and Yb, respectfully. The qualitative maps are still useful though in terms of showing how the CMAS solidified and dissolved the GYZO. Reaction products rich in *Yb* and *Gd* appear embedded in the CMAS above the dissolution front without much incorporation of *Zr* or CMAS elements. These reaction products also appear faceted suggesting a crystalline nature. The CMAS elements do not appear in heavy concentration within these reaction products and also do not all appear to have solidified uniformly above the dissolution front. While *Si* and *Mg* appear to be uniform everywhere around the regions of high *Yb* and *Gd* concentration, *Ca* and *Al* appear to be concentrated in opposite places of one another—i.e. where one element is heavily concentrated the other is not.

Figure 28 shows higher magnification BSE images of the regions at and above the dissolution front as well as the corresponding quantitative EDS. At least four regions of distinct chemical composition have been identified within these regions. The *Spherical Particles* are rich in *Zr* and also contain the other elements of the GYZO substrate. The *Crystals* have a very faceted morphology and consist of nearly equivalent amounts of *Gd* and *Yb*, some *Ca* and *Si* incorporation, and only minor amounts of *Zr*. The *Spherical Particles* and *Crystals* are embedded within a matrix consisting of two distinct CMAS-rich regions. The *Light CMAS Background* region has *Si* as its largest constituent but also has minor amounts of the ceramic-oxide substrate present. However, the *Dark CMAS Background* region has no detectable substrate elements and *Ca* is the largest constituent not *Si*. The larger amount of *Ca* by wt% is probably the reason for the difference in the z-contrast between the two CMAS-rich regions.

Discussion: **CMAS-$GdYbZr_2O_7$ Interactions –** To determine why there are two distinct CMAS-rich matrix regions, a relevant ternary phase diagram is used to determine what phases are present based on the quantitative EDS results. Figure 29 shows the two CMAS-rich regions superimposed on a re-drawn isothermal cross-section of the SiO_2-CaO-Al_2O_3 ternary system at 1300°C. These compositions on the diagram ignore the presence of the minor constituent MgO and are thus normalized in terms of SiO_2, CaO, and Al_2O_3 wt.%. This ternary is a metastable representation of the associated phases and it is assumed that no pseudowollasite phase can kinetically crystallize within the time frame of the experiment. Thus, the liquid region is extended all the way to the CaO-SiO_2 binary, as was assumed previously [68], even though this would not be expected at equilibrium.

The composition of the *Dark CMAS Background* falls within the liquid phase of the metastable ternary, while the *Light CMAS Background* falls within the Liquid + CA_2S_2 (Anorthite) phase. It is logical that both CMAS compositions had a liquid at equilibrium at this temperature given that the CMAS had to become molten to dissolve the GYZO. Previous work also identified the starting CMAS composition to be in the liquid phase at 1300°C [68] and emphasized the role of Al_2O_3 in driving the dissolution-reprecipitation reaction. The dissolution of Al_2O_3 into the glass melt pushes the composition to the anorthite + liquid field where anorthite nucleates and is at equilibrium with the CMAS melt. As the dissolution-reprecipitation reaction continues, the composition of the melt is pushed toward the Al_2O_3 corner of the ternary system.

Approach: **CMAS - 5 mole% Yb-$SrZrO_3$ Interactions –** $SrZrO_3$ and Yb_2O_3 oxides were ball milled in ethanol for 24hrs. The 5 mole% Yb-SrZrO3 (YSZO) pellet was then pressed in a cold isostatic press to 45,000 psi to achieve a relative density of 60%. The pressed pellets were bisque-fired for 2 hours at 1050°C so that they could be drilled. The pellets were drilled with a 3-mm, titanium-carbide drill bit to allow placement of the CMAS within the pellet. The drilled pellets were then sintered with CMAS at 1300°C. The sintered pellets were cross-sectioned using a slow-speed diamond saw, embedded in epoxy, and ground down to 1 micron using diamond-lapping films. The polished mount was then sputter coated with *Ir* and quantitative EDS was performed at 29 kV and 2.4 nA (29 kV was used in order to use the Kα1 line of Sr—located at 14.2 keV for quantification).

Results: **CMAS - 5 mole% Yb-$SrZrO_3$ Interactions –** Figure 30 shows a BSE image of the attack of YSZO by CMAS and the corresponding qualitative EDS maps. The CMAS elements appear to have solidified into two different layers above the dissolution front. The BSE image supports this with two distinct regions of contrast above the dissolution front. The top layer appears to be much more concentrated with the CMAS elements, while the bottom layer is more diffuse. All CMAS elements appear uniform in the top layer with the exception of Mg. This segregation of Mg is supported in the BSE image that shows a darker contrast for the regions where Mg is located and lighter where Mg is not. Below the bottom CMAS layer Ca and Mg are not present, but Si and Al appear to continue to penetrate the YSZO. However, examination of the EDS energy spectrum reveals that there is overlap of the Si and Sr energy lines as well as the Al and Yb energy lines. The substrate elements do not appear significantly in the top CMAS layer. In the bottom CMAS layer, Zr appears to be dispersed around the CMAS elements.

Figure 31 shows a higher magnification BSE image of the region at and above the dissolution front as well as the corresponding quantitative EDS. At least four regions of distinct chemical composition have been identified within this dissolution region. There are two regions that consist primarily of the substrate elements—the *Light Dissolved Product* and the *Dark Dissolved Product*. Both of these regions have

minor amounts of Sr, Ca, and Si but they differ in their wt.% of Zr and Yb—the *Light Dissolved Product* has more than twice the Yb of the *Dark Dissolved Product* and less Zr. The other two regions—*Light Crystal* and *Dark CMAS Background*— consisted mostly of CMAS elements and Sr. The elemental wt.% breakdown is very similar between these two CMAS-rich regions and the only real differences between the regions are the presence of Mg in the *Dark CMAS Background* and the presence of Zr and Yb in the *Light Crystal*. The *Light Crystal* also appears very faceted in BSE image.

Discussion: **CMAS - 5 mole% Yb-$SrZrO_3$ Interactions –** A ternary system consisting of the components CaO, SiO_2, and SrO is difficult to obtain. However, a binary diagram consisting of two perovskite structures—$CaSiO_3$ and $SrSiO_3$—is available above 1200°C and is redrawn in Figure 32. It is necessary to make same assumptions in order to determine where the CMAS compositions fall within the phase diagram. First, the minor constituents are ignored in the system—Mg and Al for the *Dark CMAS Background* and Zr and Yb for the *Light Crystal*. The second assumption is in regards to not knowing how much O to assign to the cations in either perovskite structure. Therefore, it was assumed that Ca and Sr contributed one mol of O and Si two mol of O to each of their respective perovskite structures. With these assumptions, both compositions are ~46 mol% $SrSiO_3$ and fall within the two-phase region of the binary phase diagram—$CaSiO_3$ + $SrSiO_3$—at 1300°C. This seems logical due to the similar elemental wt.% of each of the cations and the equivalent stoichiometry for both crystal structures. There are extensive solid solution regions over a 250°C plus temperature range for both perovskite structures outside of the narrow 2-phase region. With the addition of more Sr into the system, the composition would fall within the $SrSiO_3$ solid solution and Ca would merely substitute for Sr as opposed to form a distinct perovskite phase.

The maps indicate that the CMAS stops penetrating into the YSZO. However, the maps and the BSE images do not indicate many faceted YSZO reaction products as was reported for the CMAS interaction with another rare-earth zirconate GZO [69]. Previously, the CMAS reacted significantly with the GZO so that the resulting crystalline reaction products obstructed continual penetration of CMAS into the pores of the GZO [69]. That mechanism is not supported in CMAS reaction with YSZO. While perhaps perovskite reaction products are formed, these structures do not appear to obstruct the CMAS penetration into the YSZO. However, the CMAS is dissolving the YSZO as shown in the higher magnification BSE images and is supported by qualitative and quantitative EDS detecting CMAS around the dissolved YSZO. The reason for the limited CMAS dissolution of YSZO is therefore unclear but may have been limited by the kinetics of the dissolution reaction. Regardless, YSZO remains an interesting rare earth zirconate to study for CMAS mitigation as it had less CMAS penetration than either $GdYbZr_2O_7$ or GZO as shown in Table 1. Further study would help us understand why the YSZO-CMAS reaction limits penetration and could help identify other possible candidates for CMAS mitigation.

5. TBC Phase Destabilization Under Elevated Water Vapor Exposures

Efforts have been expended to utilize Raman Spectroscopy and X-ray diffraction to monitor phase evolution and destabilization of APS YSZ TBC top coat materials, focusing on the effects of exposure to high water vapor content. Sections of as-sprayed TBC plates have been profiled via Raman spectroscopy, to examine shifts in the absorbance spectrum features characteristic of the t' phase of the TBC coatings – and phases that may appear with phase evolution – that may give insights into mechanisms of coating degradation and destabilization. Similarly, the materials have been examined via X-ray diffraction analysis to explore these same degradation mechanisms via analysis of changes in lattice parameters of

the ceramic top coat, indicating evolution of the material to less desirable cubic and monoclinic phases. Peak shifts and peak broadening are expected as the t' phase breaks down and yttrium diffusion occurs to form Y-rich and Y-poor domains. Of particular interest is whether the kinetics of these processes are affected by the water vapor content in the exposure environment, and if so by what mechanism.

Approach: Raman Spectroscopic Studies – We have utilized the FZJ resources to process free-standing plates of TBC coatings for studies of materials stability in syngas and HHC environments. A large plate of 8YSZ material was manufactured to a thickness of approximately 3mm, processed by spraying onto stainless steel substrates and etching away the substrate. This plate was removed from the metal substrate used in air plasma spraying (APS) through an acid etching procedure. The resultant plate of material is shown in Figure 33. These materials were then sectioned for use in experiments evaluating the role of high water vapor content exposures on destabilization of the TBC coating materials (via Raman spectroscopy and XRD studies). This material was sprayed under conditions that provided commercially relevant porosities (17%) and a compliant APS microstructure, to ensure the relevancy of results generated to applications in turbine engine technologies. To understand the effect of combustion environment on coating stability the coatings were annealed at different times in dry and humid (20Kpa water vapor) environments in 100kpa total pressure at 1300°C. A tube furnace system has been modified to carry out high temperature exposures under controlled water vapor content in the environment, and then perform time dependent studies of changes in the Raman and x-ray spectroscopic data.

Raman spectra were obtained from the coatings using a Renishaw *inVia* confocal Raman microscope (Renishaw, Hoffman Estates, IL) using a 562nm laser operated at room temperature. Fitting was conducted to find peak positions and widths using OrginPro commercial peak fitting software (OrginLab, Northampton, MA). The rate at which peak shifting and narrowing occurs provides information on the kinetics of phase destabilization. Raman spectra were acquired with a 532 nm edge laser with a 2400 l/m grating groove. Prior to each run the system was calibrated with a Si standard. All Raman spectra were taken on the same day to avoid any peak shifting due to fluctuations in room temperature. The largest, characteristic Raman peak of tetragonal zirconia at 640 cm^{-1} was fitted with a Pseudo-Voight peak function. The 260 cm^{-1} peak for tetragonal zirconia was fitted with an Asymmetric Double Sigmoidal peak function. The peak positions were determined from the fits of five averaged Raman spectra. The standard deviation for the averaged peak positions of each of the aging times was less than 0.1 %.

Results: Raman Spectroscopic Analysis – A representative spectrum of the APS YSZ TBC heated to 1300°C before aging is shown in Figure 34, verifying accurate measurement of the spectrum (in good agreement with results reported in the literature. This now serves as a baseline from which materials evolution may be monitored and correlated with micro-chemical and microstructural changes. Figure 35 shows where the six characteristic tetragonal peaks fall on the spectra shown in Figure 34 [70]. The spectra peaks are shifted off-center of the tetragonal characteristic lines. The apparent discrepancy from the characteristic lines is likely due to strains built into the coating during the thermal spray process. Figure 36 shows the Raman peak position as a function of the Larson-Miller parameter (LMP) for the dry oxygen and water vapor environments. The aging times for dry oxygen were 6, 15, and 75 hrs while for the water vapor environment it was 6, 15, and 24 hrs. The Raman peak position for the 640 cm^{-1} peak increases linearly (R^2 = 0.973 and P = 0.147) with increasing LMP. Although this peak was not fit in earlier work **[70]**, the Raman peak shift for 8YSZ was shown to follow a linear trend for three different tetragonal peaks when plotted as a function of LMP.

In the water vapor environment, the Raman peak position also increased linearly with increasing LMP (R^2 = 0.988 and P = 0.1002). The shift of the 640 cm^{-1} peak position occurs more rapidly than in the case of the dry oxygen with the slope of the fit for the water vapor data being three times larger. Previous work **[70]** had attributed the shift of Raman lines in 8YSZ to misfit strains from ageing. The strains were thought to result from the formation of local tetragonal and cubic phases in a two-phase composite. No direct evidence was observed for the cubic phase formation and the phase transformation may actually be to a modulated structure consisting of local Y-rich and Y-lean lamellar domains [71]. Nevertheless, this phase transformation was followed by a change in morphology that was said to be influenced by a coherency strain. The acceleration in the shift of the Raman peak position in the water vapor environment is the acceleration of a phase transformation. Increased volatilization of yttria in the water vapor environment from 8YSZ may explain the quicker transformation rate from the t' phase to the coexistence of alternating Y-rich and Y-lean phases. This is supported by the observation that the increase in the degree of tetragonality (*c/a*) was found to increase with ageing time [72] as the yttria content in the tetragonal phase decreases [71].

Figure 37 shows a comparison of the 260 cm^{-1} peak positions for the dry and humid oxygen environments. The increase in the Raman peak position increases linearly with the LMP for the humid environment (R^2 = 0.999 and P = 0.00933) as it did for the dry environment. However, the slope for the humid environment is less than half of the slope for the dry environment. It is not clear if this trend will hold for other characteristic peaks of the 8YSZ tetragonal phase. Whether or not the humid environment will affect the different modes of vibration for 8YSZ in the same way requires further study. More spectra need to be taken at different ageing times to verify this trend. This spectra needs to have higher signal-to-noise ratios to ensure better fits of the spectra peaks and therefore more accurate determination of the peak positions. Also, the same spectra peaks fitted in previous work will be fitted in the future for a direct comparison.

Approach: X-ray Spectroscopic Studies – On a parallel front, efforts to measure TBC instabilities and monitor materials degradation by X-ray diffraction have been undertaken. X-ray peak shifts and peak broadening are expected as the t' phase breaks down and yttrium diffusion occurs to form Y-rich and Y-poor domains. Of particular interest is whether the kinetics of these processes are affected by the water vapor content in the exposure environment. Materials from the same material billet as used for the Raman spectroscopy study were utilized in aging studies based on XRD analysis. Long-term materials exposures have been carried out, and measurements from the samples have been assessed.

XRD was performed using the 1-D, D/tex detector with Bragg-Brentano optics. The scan speed was 2 deg/min with a step size of 0.02 deg. Due to the fact that phase destabilization of zirconia is a thermally activated process, requiring diffusion of yttrium in the zirconia lattice, we can plot our data using a Larson Miller parameter. Larson Miller parameters collapse time and temperature on to one independent axis allowing direct comparison of sample heat treated at different times and temperatures. Side-by-side comparison of samples exposed in dry and wet environments with LMP allow for direct assessment of the effect of water vapor on the kinetics of structural changes. If the activation energy for the phase destabilization is any different in humid environments than in dry environments it will result in coatings with the same LMP having different peak shifts. This data then provides the foundational materials behavior information to the community – in the use of Raman and XRD spectroscopy to examine subtle structural changes, as well as understanding the effect of water on coatings at high temperature.

Results: X-ray Spectroscopic Analysis – The XRD scans for the five conditions are shown in Figure 38.

The as received state is markedly different from all of the aged samples as expected due to processing by the APS method. Unmelted or partially melted particles become embedded in the coating during the APS process and leave a noticeable fraction of the monoclinic phase in the as-received coating [73]. Evidence of this is seen in Figure 39, where the (111) and $(11\bar{1})$ peaks of the monoclinic phase are observed. There are differences that can be observed among the aged samples without zooming in at a particular peak. Peak broadening can be observed for the aged samples at 84° with increased ageing time as well as at 59°. More subtle differences can be observed by zooming in at particular peaks.

Figures 40-42 show specific peaks for the five conditions as well as the markers for the *t'* 8YSZ phase. In Figure 40 at 30.2 °, the peaks shift to a lower 2θ value and become more symmetrical with increased ageing time. Moreover, the peaks are shifting away from the *t'* phase. In Figure 41 at 35.1°, the *t'* peak broadens with increased ageing time and there is a slight increase in intensity of an emerging peak at a lower 2θ value. A similar trend is observed in Figure 42 between 59-60°.

The general qualitative trends observed here match the quantitative trends found by Levi, *et al* [74]. The phase markers used in the figures for the *t'* phase correspond to lattice parameters that match those found in Levi, *et al* for APS 8 YSZ. Also, the *tetragonal* phase fraction reaches a maximum value and then decreases with increased exposure severity. The monoclinic phase is not observed in the figures for the aged samples because the severity of exposure used was below a Hollomon–Jaffe parameter (HJP) of 51,000—the threshold level found by Levi et al. to indicate the onset of monoclinic formation [74]. The more significant shift that takes place at 30.2º for the 75 hrs ageing time is likely a result of the large increase in the phase fraction of *cubic+t''* that occurs from a HJP of $48.1 \cdot 10^3$ (24 hrs aging) to a value of $49.3 \cdot 10^3$ (75 hrs aging). Comparisons between observations made with materials exposed to dry and humid environments are illustrated in Figures 43-45. Comparing numerous exposure conditions (quantified via the Larson Miller Parameter) shows minimal evidence of any water-vapor dependence on the aging process for the YSZ TBC materials.

To evaluate whether there is any evidence of near surface effects such as yttria volatilization, which are being hidden by "bulk" analysis with standard XRD analysis, we have performed Grazing Incidence XRD analysis. With this technique, the thickness of material under study (depth from the surface)is controlled by varying the grazing incidence angle of the x-ray probe. Grazing Incidence XRD (GIXRD) was performed on the polished, 87.7 hrs humid-aged sample. The largest tetragonal peak and the largest monoclinic peak are shown below at incident angles ranging from 0.2-1.6 deg. A rough approximation of the x-ray penetration can be found using a simulator from the Center for X-Ray Optics at Lawrence Berkeley National Laboratory. Going from an incident angle of 0.2 to 1.6 deg, the approximate x-ray penetration depth into Zirconia at 30keV is 300 nm to 2.6 μm, respectively. From an angle of 35 to 75 deg, the approximate depth is 55 μm to 92 μm, respectively. Since the monoclinic peaks do not decrease at larger incident angles and deeper x-ray penetration (Figures 46 and 47), there is little evidence for more of the monoclinic phase at the surface. This is indicative that there is not preferential volatilization of yttrium at the surface for the humid-aged sample.

Discussion and Conclusions – We have found that under these experimental conditions there are substantial changes in the coating microstructures, and that the kinetics of the relevant phase change can be quantitatively studied by Raman spectroscopy. On the other hand, XRD analysis provided supplemental information on the types of phases that are present in the coating microstructure, as a function of aging and environmental exposures.

6. CMAF Infiltration into TBC Systems as a Function of TBC Microstructure

The CMAS/CMAF composition specified above as best representing that expected for IGCC turbine operations has been used in TBC exposure and infiltration experiments that assess whether there is a significant impact of TBC layer microstructure on the infiltration of CMAS and associated TBC degradation. The thermo-chemical interactions of CMAF with free-standing YSZ is herein presented, with particular attention paid to the role of coating microstructure.

Approach – Following the approach described above, we have also prepared a number of materials with the basic 8YSZ composition, with the thermal spray parameters varied to control the microstructural parameters. In particular, we have targeted the development of materials with (1) an "industry standard" APS porous microstructure, and (2) three different vertically cracked (or "segmented" coating microstructures) to explore what constitutes an optimal microstructure for CMAS resistance. Intuitively, the segmented microstructures appear to be inferior from the standpoint of molten phase infiltration (and thermo-mechanical damage development). However, laboratory tests have suggested otherwise, such that a focused study of these effects is deemed a priority. As such, free-standing plates of the TBC materials are being processed, as shown in Figure 48. These plates were again removed from the metal substrate used in air plasma spraying (APS) through an acid etching procedure.

While pursuing these efforts in regards to segmented coatings, the lack of a quantitative (and predictive) understanding of tailoring the development of segmented coating microstructures has come to light. In an effort to better understand the materials and processing relate parameters that control the development of segmented crack microstructures, we have also processed materials to allow for a detailed study of the segmentation crack development mechanism. Under various spray conditions, we have sprayed TBC layers as single-pass coatings and sequentially developed thickness, varying robot speeds and spraying conditions as they relate to the microstructural development. These materials are now being sectioned and examined. However, a representative example of the microstructural development is shown in Figure 49, where sprayed coatings of various thicknesses (increasing spray passes) are shown in relation to the vertical crack development.

Sections from these plates have been prepared with CMAF surface deposits (applied as a paste to a select region of the surface, at a specified loading). The TBC materials with CMAF deposits were then subjected to heat treatments of 1400°C in air for two hours in air. The materials were subsequently sectioned and examined in order to determine the overall degradation effects, and specifically the role of TBC microstructure on CMAF infiltration and thermo-chemical reaction. Three YSZ configurations were infiltrated with CMAS: one standard air plasma sprayed (APS) and two segmented (aka dense vertically cracked). The spray temperature of the segmented specimens was not high enough to yield a purely segmented microstructure, so a hybrid of dense APS and segmented was achieved instead; eight spray passes were completed for each type, yielding 500mm thick specimens with a high porosity horizontal partition approximately every 60mm. The CMAF deposit was a laboratory-created CMAF (Ca, Mg, Al, Fe) that also contained some amount of Si.

Results and Discussion – We have also carried out studies of the infiltration of "CMAF" into YSZ plates with various microstructures. The worst examples of such CMAF attack on each YSZ configuration are captured in Figure 50. The standard APS specimen experienced CMAF penetration through the entire thickness, which caused considerable volume expansion; the segmented specimens were not fully infiltrated, but were damaged significantly in the top few segments. Higher magnification SEM images

of the same three specimens are shown in Figure 51. Reordering of the microstructure by CMAF attack took place on very different length scales in APS vs. segmented. The new APS microstructure is indicative of a complete dissolution of YSZ, followed by the reprecipitation of large (~20μm) YSZ spheres, with glassy phases and equally large pores scattered in between; the original microstructure – and therefore the intended compliance – is completely lost. The portions of the segmented specimens that remained largely intact (i.e. the bottom half) experienced glass infiltration of the purposefully induced vertical cracks (Figures 51 and 52, Segmented 1) and YSZ re-ordering similar to APS, but a full order of magnitude smaller (Figures 51 and 52, Segmented 2). The clogging of vertical cracks with glass likely means that compliance was significantly lost even in the portions of the microstructure that did not fail catastrophically. Backscattered electron imaging demonstrates that there are two distinct glassy phases which precipitate upon cooling, and which are referred to here as light and dark glass. A saw-tooth pattern was observed at the interface between re-precipitated YSZ and glass in both APS and segmented samples, indicating that interfacial surface area needed to be increased in order to accommodate the large amount of surface energy that was locked in upon cooling.

This set of images demonstrate that, at least in the isothermal tests that have been carried out to date, that the coating *microstructure* has a profound influence on the CMAS-related damage development. Whereas the APS coating has been fully infiltrated through-thickness and undergone extensive dissolution and thermo-chemical degradation, the segmented coatings show much less pronounced degradation, and only partial infiltration (partial penetration through-thickness of the coating material).

7. Volatility of TBC Stabilizers (Y_2O_3) in Elevated Water Vapor Environments

During the conduct of this project, efforts have been expended to better understand the susceptibility of thermal barrier coating constituents (in this case Y_2O_3) to volatility in the relevant syngas of HHC combustion environments.

Approach – An experimental apparatus consisting of an environmentally-controlled TGA system is utilized to study the volatility of Y_2O_3 in high temperature (1000°C < T < 1500°C) water vapor environments. The experiments are carried out using a tube furnace with a quartz tube with a zirconia tube insert. Weight loss measurements (by way of TGA analsysis), SEM observations, and x-ray diffraction analysis is used to examine yttria volatility and possible experimental artifacts due to volatile species impurity deposition.

Results and Discussion – Initial efforts were hampered by the finding that impurities (silicon and/or aluminum) are subsequently deposited on the samples surface, prevent proper analysis of volatile loss of yttria by weight loss measurements. Three possible sources of these impurities have been identified, and protocols to distinguish each (and mitigate these effects) are now underway. The impurities may originate from the samples themselves, from the quartz tube, or from the alumina or zirconia liner tubes. To examine if back diffusion was the source of silicon contamination of our samples both flow rate and the position of the yttrium samples in our liner tube (zirconia) was varied. Experiments have demonstrated a decrease in the amount of yttrium silicate formation (Figure 53). Varying the flow rate seems to point us in a similar direction as shown in Figure 54. It should be noted that varying the flow rate also caused a variation in sample temperature and the partial pressure of water in the environment. Further work is needed to sort out the relative role of each of these variables. An EDS scan of an as received sample, along with a sample that has been exposed to the high temperature water vapor rich environment, shows the presence of aluminum (Figure 55) for the exposed specimen. This implies that

the alumina insert is acting as a source of impurities as well. Eventually, the test system was modified with a thin platinum liner in the TGA furnace tube. With this liner in place, weight loss measurements indicated negligible yttrium volatility in high water vapor content environments, at least for the test temperatures being utilized here.

Discussion and Conclusions – There is no significant evidence of water-vapor-enhanced degradation of YSZ TBCs due to the preferential volatilization of the stabilizer yttria.

8. Alternative TBC Materials – Synthesis and Evaluation

Another objective of this research program was to evaluate the potential of alternative materials to enhance durability in the IGCC turbine environment, particularly in regards to CMAS attack. To facilitate these studies, we synthesized select materials as alternative TBC materials. The aero-propulsion community has already identified several classes of materials that have promise as substitutes for YSZ, based on having lower thermal conductivity. Recent studies have also demonstrated that some of these materials have additional promise in regards to their response to CMAS attack. For instance, Gd-zirconate has been evaluated, and shown to have higher resistance to CMAS infiltration – although the specific mechanisms leading to the enhanced performance have not yet been fully elucidated. In this program, we evaluated other zirconates that have even lower thermal conductivity, and that can be tailored into bi-layer combinations of these zirconates with YSZ (for reasons of compatibility with the underlying alumina-based TGO).

Approach – We continued interactions with leading experts in thermal spray processing of turbine hot-section materials at the Forschungszentrum Jülich (Jülich, Germany). In particular, we carried out studies of optimal spray conditions for APS processing of Sm-zirconate coating materials. Using in-flight particle diagnostics, we are able to look at the temperature distribution of particles in flight, and determine whether the materials are reaching an optimal temperature relative to the melting point of the target material, without starting to break down in multiple (and less-desirable phases). Figure 56 presents a summary of histograms of in-flight temperature distributions, which demonstrate that at the more aggressive spraying parameters, there is a dual peak developed that suggests phase breakdown. The optimal spraying conditions are determined to be those that produced the data in Figure 56b. From this study, processing conditions were determined for processing free-standing plates and thermal cycling rig buttons from Sm-zirconate top coat materials.

We produced plates of samarium zirconate materials, as thermally sprayed components, followed by isothermal exposures of the $Sm_2Zr_2O_7$ materials to CMAS deposits. We obtained the raw oxides for synthesis of $Sm_2Zr_2O_7$ powders through solid-state synthesis routes, and then processed proper thermal spray feedstock by way of spray drying. An example of the resulting spherical granules is shown in Figure 57. A 5kg of feedstock powder was synthesized. Moving forward, the same powders may be thermally sprayed into practical TBC microstructures, following the same procedures outlined above for YSZ materials. The materials were then subjected to identical CMAS exposure and infiltration experiments as outlined above for the YSZ materials.

Results and Discussion – A set of images similar to those collected for YSZ were collected for CMAF-infiltrated $Sm_2Zr_2O_7$ (Figures 58, 59 and 60). The original microstructure was intended to have 15-17% porosity uniform across the thickness of the specimen, with no cracks. The “as received” specimen achieved the porosity goal, measuring 17%, 17% and 15% in the top, middle and bottom thirds of the

cross-section, respectively (porosity was measured as a percent area of a thresholded SEM image). A series of cracks connected the porosity, however, as is evident in Figure 58; a high magnification look at a crack is shown in Figure 59.

CMAF infiltration was limited to less than 100μm in each of the $Sm_2Zr_2O_7$ microstructures tested (Figures 59 and 60). A dense, glassy phase is visible for the first ~50μm, followed by another ~50μm of depth throughout which the pores have coalesced and the cracks have seemingly disappeared. High magnification images (Figure 60) reveal that two distinct glass phases are present in both specimens, as was the case in the infiltrated YSZ.

EDS results (Table 6) display the average composition for each phase (coating and glass) in the infiltrated YSZ and $Sm_2Zr_2O_7$. In both materials, the largest constituent of the light and dark glass phases is Fe. The light phase is primarily classified by having a heightened amount of Fe compared to the dark phase. The composition of the as received (AR) $Sm_2Zr_2O_7$ is nearly identical to that of the coating phase in the infiltrated sample, indicating that very little – if any – CMAF was incorporated into the $Sm_2Zr_2O_7$ microstructure below the glass cap (the data for the infiltrated phase was collected between 20 and 50μm below the bottom of the glass cap). These results appear to confirm that $Sm_2Zr_2O_7$ has high resistance to CMAF attack, especially compared to YSZ.

9. Characterization of Alternative TBC Materials – $Sm_2Zr_2O_7$ TEC Determination by HTXRD

In addition to exploring the susceptibility of these new TBC materials to CMAS attack, we also measured basic constituent properties for this potential alternative TBC coating material, namely the thermal expansion coefficient (TEC) – a key parameter in any layered system undergoing thermal variations.

Approach – The Rigaku SmartLab high temperature x-ray diffraction (HTXRD) system was used to calculate the thermal expansion coefficient (TEC) for $Sm_2Zr_2O_7$ powders. The goal was to test the viability of the method by comparing it to literature values that were obtained using a high temperature dilatometer [75]. Bragg-Brentano (BB) optics were chosen over parallel beam (PB) optics due to the higher peak resolution they afforded. BB also made it possible to use a 1D detector, which sped up the measurements, allowing for more temperature increments and more 2q range to be explored in a practical amount of time (14 hours). PB optics are often preferred for measurements such as these – despite the poorer resolution – because PB is less sensitive to specimen displacement errors that result from the sample expanding at temperature. By programming the Rigaku SmartLab to perform automated sample height alignments at each new temperature, however, displacement errors were eliminated and the advantages of BB optics were realized without any trepidation.

A plot of the x-ray spectra as a function of temperature is shown in Figure 61. The determined TEC vs. temperature for the HTXRD method is shown in Figure 62a. Data was collected from 50 to 1400°C with a ramp rate of 5°C/min and a hold time of 5 minutes before making each measurement. Data points represent the average TEC values from four high angle peaks, associated with the following *hkl* planes: *(8 8 0)*, *(10 6 2)*, *(12 0 0)* and *(12 4 0)*. The HTXRD plot can be compared to the HT dilatometer plot in Figure 62b. The lone discrepancy between the data – a hump at 200°C – may have to do with the amount of time allowed for the sample to equilibrate at each new temperature step, as well as the differences in the nature of the furnaces used. Indications were that dilatometer rods were measured "continuously" at 5°C/min. It is suspected that HTXRD TEC values might not dip after 200°C if given longer than 5 minutes to equilibrate. This behavior is being further studied, and will be reported in the future. More

data points may be taken between 0 and 300°C to better resolve the low temp regime.

Figure 63 plots the linear expansion of $Sm_2Zr_2O_7$ vs. temperature. The TEC for the range of 300-1400°C is measured at 1.0E-5°C^{-1}, compared to the literature value, 1.0E-5°C^{-1} [76]. The values in this HTXRD study are derived from $Sm_2Zr_2O_7$ powders that were pressed into pellets. Identifying the TEC values for those specimens may help determine if $Sm_2Zr_2O_7$ can adequately replace standard YSZ in a TBC-coated hot-section system.

10. Thermal Gradient Testing and Thermo-Mechanical Behavior Modeling

Development provided a foundation of analytical treatments to model the thermo-mechanical aspects of segmentation cracking and molten phase intrusion into these microstructures. Basic elements of the analytical model, which capture microstructural details and thermal gradient effects, have been developed; future efforts are aimed at accounting for local stress fields as a function of thermal history.

Also facilitated by the visiting appointment at the Forschungszentrum Jülich, we were able to jump start on performing thermal-gradient based testing of alternative materials, and also exploring thermo-mechanical implications of molten-phase intrusion into alternative TBC coatings. Burner rig testing has been done on button cell specimens coated with samarium zirconate coatings. In parallel to preparation of the burner rig buttons, additional flat plate coupons of each material are being APS thermal spray processed to allow for isothermal studies of CMAS interactions. We have come to recognize that there are opportunities to induce molten phase infiltration resistance to a TBC top coat through tailoring of the coating microstructure (porosity and crack networks). . In addition, the PI has continued analytical work to model the thermo-mechanical aspects of molten phase intrusion, crack growth during thermal cycling, coating delamination, and the impacts of microstructural tailoring. Basic aspects of the modeling efforts to capture microstructural details and thermal gradient effects are in place.

.

LIST OF TABLES

Table 1: Compositions, in weight percent, of alloys prior to oxidation (M = Ni and Co, X = Y or Re). An asterisk indicates that data were collected by the authors using EDS at 15 kV. All other numbers are supplied by manufacturers. EDS error is +/- 1%.

Table 2: Compositions of bottom ash (obtained from Jeff Bons, OSU), in terms of elemental constituents.

Table 3: Compositions of bottom ash (obtained from Jeff Bons, OSU), in terms of oxide constituents.

Table 4: Compositions of CMAS that believed to be relevant for aero-propulsion turbines and IGCC turbine systems, in terms of the mol% of the constituent cations.

Table 5: Average CMAS penetration and residual glass for YSZ and the rare-earth zirconates.

Table 6: EDS results displaying the composition of phases following CMAF infiltration into YSZ and $Sm_2Zr_2O_7$ microstructures. The relevant phases are the coating and as many as two glass phases, classified as dark and light.

LIST OF FIGURES

Figure 1: Cross-section images of TBC-bond coat interfaces resulting from field tests of industrial turbine blade material systems, courtesy A. Kulkarni, Seimens Power Generation [3]. TGO develops dissimilarly on equivalent TBC systems when combusting **(a)** syngas versus **(b)** natural gas. A second set of images (not shown) indicate similar differences for a second, "Type 2" bond coat composition as well.

Figure 2: Schematics depicting a) "original" and b) "modified" wedge geometries, as they appear after taper-polishing, but before the final re-oxidation step.

Figure 3: Cross-sectional BSE micrographs (5 kV) of sprayed NiCoCrAlRe (with superalloy substrate attached) exposed for 300 h at 1125 °C in a) 0%, b) 15%, c) 30%, and d) 45% H_2O. Electroplated copper was added to aid in polishing.

Figure 4: Plan view BSE micrographs (7 kV) of sprayed NiCoCrAlRe with the superalloy substrate removed (top row) and cast NiCoCrAlY (bottom). The exposures are: not oxidized (a. and d.), and oxidized for 100 h at 1125 °C in 0% H_2O (b. and e.) and 30% H_2O (c. and f.).

Figure 5: Cast NiCoCrAlY TGO spinel coverage vs. exposure time for three different water vapor environments.

Figure 6: Plan view BSE time-lapse micrographs (5 kV) of cast NiCoCrAlY TGO from 5 (a. and e.) to 30 (b. and f.), to 55 (c. and g.), to 80 h (d. and h.) in 0% and 15% H_2O, respectively.

Figure 7: Evaporation rate of Ni from pre-fabricated $NiAl_2O_4$ pellets as a function of H_2O vol% at 1125 ^{0}C and 200 sccm gas flow rate.

Figure 8: Plan view BSE images (5 kV) of taper-polished, cast NiCoCrAlY before and after 4 h re-oxidation in 15%H_2O using the a) original and b) modified wedge geometry. In each case, the same sample was imaged before (left) and after (right) re-oxidation. High mag images appear as insets (c. and d.). The initial oxidation was 100 h in 0% H_2O.

Figure 9: a) Thin foil specimen from a cast CoNiCrAlY sample (100 h oxidation in 0% H_2O, 4 h re-oxidation in 15% H_2O) is viewed in cross-section using dark field STEM mode (30 kV). The inset (part b.) reports average EDS values for spinel grains analyzed on thin foil specimens (15 kV). EDS error is +/- 1%.

Figure 10: Plan view BSE micrographs (5 kV) of cast CoNiCrAlY modified wedges having a) no coating and b) 4YSZ coating, show no new oxide growth following 200 h, 30% H_2O re-oxidation.

Figure 11: A demonstration of the thresholding technique used to quantify the surface area coverage of spinel and alumina on low magnification BSE images. A 400 μm HFW image **(a)**, when thresholded **(b)**, canvases enough area to be representative of the macrostructure, while still accurately capturing microstructure. A 30 x 20 μm^2 area cropped from the larger image **(c and d)** produces coverage values within 1% of those derived from a higher resolution 30 μm HFW image of the same location **(e and f)**.

Figure 12: A comparison of sprayed CoNiCrAlY TGO grown in **(a)** 0% and **(b)** 15% H_2O, versus cast CoNiCrAlY grown in **(c)** 0% and **(d)** 15% H_2O for "zero hours" at 1125 °C. BSE images, 5 kV, 400 μm HFW.

Figure 13: Before-after 150 μm HFW BSE plan view images (5 kV) of cast NiCoCrAlY TGO grown in 0% (before **a** vs. after **d**), 5% (**b** vs **e**) and 15% H_2O (**c** vs **f**) for "zero hours" at 1125 °C. The rectangles overlaid on the micrographs represent the site-specific areas evaluated in Fig.5a-f.

Figure 14: Locations indicated by outlined rectangles in Fig.4 are represented as higher magnification images of NiCoCrAlY before (**a** and **b**) and after (**c** and **d**) oxidation for "zero hours" at 1125 °C in 0% and 15% H_2O, respectively. Thin foil cross-sections that spanned what was originally a β/γ' interface **(e** and **f)**, were prepared from the indicated locations. General cross-sections **(g** and **h)**, prepared via grinding and polishing from equivalent specimens, are included to show TGO morphology in higher resolution. All images 5 kV, BSE.

Figure 15: Spinel surface area coverage plotted as a function of water vapor content for cast CoNiCrAlY and NiCoCrAlY. Data are derived from 400 μm HFW BSE images (5 kV) that were thresholded. All exposures were held at 1125 °C for "zero hours."

Figure 16: Spinel surface area coverage plotted as a function of oxygen content for cast **(a)** CoNiCrAlY and **(b)** NiCoCrAlY. Data are derived from 400 μm HFW BSE images (5kV) that were thresholded. All exposures were held at 1125 °C for "zero hours."

Figure 17: Sprayed CoNiCrAlY TGO grown in 30% H_2O and 10% O_2 for 5 h at 1125 °C, seen in **(a)** plan view and **(b)** cross-section, representing the most extreme case of transient spinel growth in this study. BSE images, 5kV.

Figure 18: Spinel surface area coverage plotted as a function of the 5 h holding temperature for cast NiCoCrAlY (15% H_2O) and cast CoNiCrAlY (5% H_2O). The Greek symbols refer to the metastable alumina phase present at each temperature. Note that after holding 5 h, each specimen was ramped to 1125 °C and then back to room temp so that all experiments had equal duration.

Figure 19: Plan view, 400 μm HFW micrographs of NiCoCrAlY bond coats held for 5 h at **(a)** 825 °C and **(b)** 1125 °C (the 825 °C sample was ramped to 1125 °C and back to room temperature following its hold). The inset micrographs (**c** and **d**) are representative high magnification views of TGO that grew above the bond coat's β alloy phase.

Figure 20: *In situ* NiCoCrAlY TGO development, tracked with HTXRD from 600-1125°C.

Figure 21: XRD Patterns acquired from the (a) GZO, and (b) GYZO specimen. (hkl) indices are indicated.

Figure 22: Images taken from the cross-sectioned pellets showing the CMAS infiltration: (a) Monazite, (b) Mullite, (c) $ZrSiO_4$, (d) $CaZrO_3$, (e) $BaZrO_3$, (f) $SrZrO_3$, (g) GZO, (h) GYZO, (i) 4YSZ, (j) 5Yb-SZ.

Figure 23: (a) A BSE image from the cross-section at which CMAS reaction and infiltration of mullite took place; (b) A secondary electron (SE) image acquired from the same region, showing the anorthite crystallite morphology.

Figure 24: EDS maps of the Mullite/CMAS interface, showing the general distribution of chemistry in the resulting phase mixtures.

Figure 25: EDS mapping results from the cross-sectioned $Gd_2Zr_2O_7$ sample acquired from the infiltration region.

Figure 26: EDS mapping results from the cross-sectioned $GdYbZr_2O_7$ sample acquired from the infiltration region. A much more extensive thermo-chemical interaction is observed with the $GdYbZr_2O_7$ in relation to the $Gd_2Zr_2O_7$ materials.

Figure 27: BSE image and elemental maps of the dissolution front of CMAS into GYZO.

Figure 28: Close-up of CMAS-GYZO reaction products showing: (a) and (b) BSE images and (c) EDS results of various regions within the images.

Figure 29: Isothermal ternary phase diagram at 1300°C of SiO_2-CaO-Al_2O_3. Single-cation oxide formula units are used here so that A = $AlO_{3/2}$, C = CaO, and S = SiO_2.

Figure 30: BSE image and elemental maps of the dissolution front of CMAS into YSZO.

Figure 31: Close-up of CMAS-YSZO reaction products showing: (a) BSE image and (b) EDS results of various regions within the image.

Figure 32: Binary phase diagram of $CaSiO_3$-$SrSiO_3$. The estimated CMAS compositions—*Dark CMAS Background* and *Light Crystal*—are superimposed on the graph. The CMAS compositions are grouped together as one point because the minor constituents for both compositions are ignored.

Figure 33: A plate of free-standing 8YSZ TBC top coat material, formed by air plasma spraying (APS).

Figure 34: A Raman spectra obtained for APS-processed YSZ material, showing characteristic peaks for the initial t' (metastable tetragonal phase) of YSZ. This data set then acts as the baseline from which material evolution with extended exposures is monitored, relative to changes in the features of the spectra.

Figure 35: Typical Raman spectra on an 8 YSZ sample heated to 1300°C with no aging. The characteristic 8YSZ tetragonal Raman lines are shown in red.

Figure 36: Raman peak position as a function of the Larson-Miller parameter for the 640 cm^{-1} peak of 8YSZ. The points correspond to ageing times of 6, 15, and 75 hrs for the dry oxygen environment and 6, 15, and 24 hrs for the water vapor environment.

Figure 37: Raman peak position for the 260 cm^{-1} tetragonal peak as a function of the Larson-Miller parameter (LMP) for the dry and humid, oxygen environments.

Figure 38: XRD scans for APS 8YSZ for the as received state and various ageing times.

Figure 39: XRD scan for the APS 8YSZ as received state showing the (111) and $(11\bar{1})$ monoclinic peaks.

Figure 40: XRD scans for APS 8YSZ for the as received state and various ageing times at the 30.2º peak position.

Figure 41: XRD scans for APS 8YSZ for the as received state and various ageing times at the 35.1º peak position.

Figure 42: XRD scans for APS 8YSZ for the as received state and various ageing times between the 59-60° peak position.

Figure 43: XRD peaks of aged, APS 8YSZ with increasing Larson Miller Parameter for the (002) and (110) tetragonal planes and the (002) cubic plane. The theoretical angular positions and relative intensities are superimposed for the tetragonal, t', and cubic phases.

Figure 44: XRD peaks of aged, APS 8YSZ with increasing Larson Miller Parameter for the (013) and (121) tetragonal planes and the (113) cubic plane. The theoretical angular positions and relative intensities are superimposed for the tetragonal, t', and cubic phases.

Figure 45: XRD peaks of aged 8YSZ with increasing Larson Miller Parameter for the (004) and (220) tetragonal planes and the (004) cubic plane. The theoretical angular positions and relative intensities are superimposed for the tetragonal, t', and cubic phases.

Figure 46: XRD peaks of the 87.7 hrs humid-aged, APS 8YSZ for the (101) tetragonal plane with increasing incident angle.

Figure 47: XRD peaks of the 87.7 hrs humid-aged, APS 8YSZ for the $(\bar{1}11)$ monoclinic plane with increasing incident angle.

Figure 48: TBC coatings (as deposited) formed by thermal spray under conditions which give rise to various microstructures: (a) left-most image is that of "standard APS" porous coating; (b) and (c) have increasing levels of segmentation cracking.

Figure 49: Microstructure development during deposition of 8YSZ TBC coatings with intended segmented coating microstructure. Images show microstructure evolution as a function of spray passes.

Figure 50: SEM micrographs of the full cross-sectional thickness of a standard APS (left) and two segmented (middle, right) YSZ specimens following infiltration with CMAF. CMAF was applied to specimens from the top.

Figure 51: SEM micrographs showing cross-sections from the middle of a standard APS (left) and two segmented (middle, right) YSZ specimens following infiltration with CMAF.

Figure 52: SEM micrographs showing features of note from the middle of a standard APS (left) and two segmented (middle, right) YSZ specimens following infiltration with CMAF.

Figure 53: X-ray diffraction highlighting the formation of silicate peaks indicating impurity deposition from the tube furnace walls.

Figure 54: Comparison of Y_2O_3 samples exposed in a quartz tube furnace at 1200°C for 12 hours, with specimens placed at different positions within the zirconia tube. The middle position was 6" from the end.

Figure 55: Energy dispersive spectroscopy of an as received sample, and a sample exposed for 12 hours, at 1200°C and 50% water vapor.

Figure 56: Histograms of particle temperatures during optimization of thermal spray process protocols for Sm-zirconate coatings. The fitting illustrates process conditions at which phase breakdown occurs, and quantifies optimal spray conditions for deposition of phase-pure SZO.

Figure 57: A micrograph of a spherodized granule of $Sm_2Zr_2O_7$, ready for use in thermal spray processing.

Figure 58: SEM micrographs of the full cross-sectional thickness of an as received (left) and two infiltrated (middle, right) $Sm_2Zr_2O_7$ specimens. CMAF was applied to specimens from the top.

Figure 59: SEM micrographs showing cross-sections from the top portion of as received (left) and infiltrated (middle, right) $Sm_2Zr_2O_7$ specimens.

Figure 60: SEM micrographs showing features of note from as received (left) and infiltrated (middle, right) $Sm_2Zr_2O_7$ specimens.

Figure 61: Temperature dependent XRD spectra for $Sm_2Zr_2O_7$, showing peak shifts due to thermal expansion.

Figure 62: Comparison of TEC data obtained via (a) HTXRD and (b) HT dilatometry [75].

Figure 63: Linear expansion of $Sm_2Zr_2O_7$ via HTXRD.

REFERENCES

[1] Evans, A.G., Mumm, D.R., Hutchinson, J.W., Meier, G.H., Pettit, F.S.: *Mechanisms controlling the durability of thermal barrier coatings*. Progress in Materials Science **46**(5), 505-553 (2001).

[2] White, B.M., R.W.Ames, P. Burke: *Conditions in advanced turbines for IGCC power plants with carbon capture*. Proceedings of the ASME Turbo Expo 2013 **TE2013** (2013).

[3] Kulkarni, A., Seimens Power Generation, personal communication, 2008.

[4] Üstündag, E.et al.: *Influence of residual stresses on the evolution of micro-structure during the partial reduction of $NiAl_2O4$.* Materials Science and Engineering: A **238**(1), 50-65 (1997).

[5] Giggins, C.S., Pettit, F.S.: *Oxidation of Ni-Cr-Al Alloys Between 1000° and 1200°C.* J Electrochem Soc **118**(11), 1782 (1971).

[6] Wallwork, G.R., Hed, A.Z.: *Some limiting factors in the use of alloys at high temperatures*. Oxidation of Metals **3**(2), 171-184 (1971).

[7] Sloof, W.G., Nijdam, T.J.: *On the high-temperature oxidation of MCrAlY coatings*. International Journal of Materials Research **100**(10), 1318-1330 (2009).

[8] Nijdam, T.J., Kwakernaak, C., Sloof, W.G.: *The effects of alloy microstructure refinement on the short-term thermal oxidation of NiCoCrAlY alloys*. Metallurgical and Materials Transactions A **37A**(3), 683-693 (2006).

[9] Stiger, M.J., et al., *Thermal barrier coatings for the 21st century*. Zeitschrift Fur Metallkunde, 1999. **90**(12): p. 1069-1078.

[10] Choi, H.S., Yoon, B., Kim, H.J., Lee, C.H.: *Isothermal oxidation of air plasma spray NiCrAlY bond coatings*. Surface & Coatings Technology **150**(2-3), 297-308 (2002).

[11] Shillington, E.A.G., Clarke, D.R.: *Spalling failure of a thermal barrier coating associated with aluminum depletion in the bond-coat.* Acta Materialia **47**(4), 1297-1305 (1999).

[12] Maris-Sida, M.C., G.H. Meier, and F.S. Pettit, *Some water vapor effects during the oxidation of alloys that are alpha-Al2O3 formers.* Metallurgical and Materials Transactions a-Physical Metallurgy and Materials Science, 2003. **34A**(11): p. 2609-2619.

[13] Angle, J.P., Morgan, P.E.D., Mecartney, M.L., Cawley, J.: *Water vapor-enhanced diffusion in alumina*. Journal of the American Ceramic Society **96**(11), 3372-3374 (2013).

[14] Clarke, D.R., Tolpygo, V.K.: *Evidence of outward aluminum grain-boundary diffusion in Y- and Zr-doped alumina scales*. Presented at the Kofstad Symposium, Electrochemical Society (1999).

[15] Meier Jackson, E.M., Yanar, N.M., Maris-Jakubowski, M.C., Onal-Hance, K., Meier, G.H., Pettit, F.S.: *Effect of surface preparation on the durability of NiCoCrAlY coatings for oxidation protection and bond coats for thermal barrier coatings*. Materials and Corrosion **59**(6), 494-500 (2008).

[16] Haynes, J.A., Unocic, K.A., Pint, B.A.: *Effect of water vapor on the 1100°C oxidation behavior of plasma-sprayed TBCs with HVOF NiCoCrAlX bond coatings*. Surface and Coatings Technology **215**, 39-45 (2013).

[17] Zhou, C., Xu, H., Gong, S.: *Influence of water vapor on the cyclic-oxidation behavior of a low-pressure plasma-sprayed NiCrAlY coating*. Oxidation of Metals **62**(3-4), 195-206 (2004).

[18] Saunders, S.R.J., Monteiro, M., Rizzo, F.: *The oxidation behaviour of metals and alloys at high temperatures in atmospheres containing water vapour: A review*. Progress in Materials Science **53**(5), 775-837 (2008).

[19] Essuman, E., Meier, G.H., Żurek, J., Hänsel, M., Quadakkers, W.J.: *The effect of water vapor on selective oxidation of Fe–Cr alloys*. Oxidation of Metals **69**(3-4), 143-162 (2008).

[20] Zurek, J.et al.: *Growth and adherence of chromia based surface scales on Ni-base alloys in high- and low-pO_2 gases*. Materials Science and Engineering: A **477**(1-2), 259-270 (2008).

[21] Buscail, H., Heinze, S., Dufour, P., Larpin, J.P.: *Water-vapor-effect on the oxidation of Fe-21.5wt%Cr-5.6wt%Al at 1000°C*. Oxidation of Metals **47**(5-6), 445-464 (1997).

[22] Ehlers, J., et al., *Enhanced oxidation of the 9%Cr steel P91 in water vapour containing environments.* Corrosion Science, 2006. **48**(11): p. 3428-3454.

[23] Galerie, A., Wouters, Y., Caillet, M.: *The kinetic behaviour of metals in water vapour at high temperatures: Can general rules be proposed?* In: Streiff, R. Wright I. G. Krutenat R. C. Caillet M. Galerie A. (eds.) Material Science Forum, vol. 369-372. Materials Science Forum, pp. 231-238. (2001)

[24] Norby, T.: *Protonic defects in oxides and their possible role in high-temperature oxidation.* Journal De Physique IV **3**(C9), 99-106 (1993).

[25] Norby, T.: *Wagner-type theory for oxidation of metals with co-transport of hydrogen ions.* Electrochemical Society Proceedings **99**(38), 1-16 (1999).

[26] Schütze, M., Renusch, D., Schorr, M.: *Parameters determining the breakaway oxidation behaviour of ferritic martensitic 9%Cr steels in environments containing H_2O*. Corrosion Engineering, Science and Technology **39**(2), 157-166 (2004).

[27] Essuman, E., Meier, G.H., Żurek, J., Hänsel, M., Singheiser, L., Quadakkers, W.J.: *Enhanced internal oxidation as trigger for breakaway oxidation of Fe–Cr alloys in gases containing water vapor*. Scripta Materialia **57**(9), 845-848 (2007).

[28] Asteman, H., Svensson, J.E., Johansson, L.G.: Evidence for chromium evaporation influencing the oxidation of 304L: The effect of temperature and flow rate. Oxidation of Metals **57**(3/4), 193-216 (2002).

[29] Opila, E.J., et al., *Predicting oxide stability in high-temperature water vapor*. JOM, 2006. **58**(1): p. 22-28.

[30] Meschter, P.J., Opila, E.J., Jacobson, N.S.: *Water vapor-mediated volatilization of high-temperature materials*. In: Clarke, D.R. (ed.) Annual Review of Materials Research, Vol 43., pp. 559-588. (2013)

[31] Nychka, J.A., Clarke, D.R.: *Quantification of aluminum outward diffusion during oxidation of FeCrAl alloys*. Oxidation of Metals **63**(5-6), 325-352 (2005).

[32] Nychka, J.A., Clarke, D.R., Dryden, J.R.: *Quantifying cation grain boundary diffusion*. Journal of Applied Physics **102**(3), 034907 (2007).

[33] Jacobson, N., et al., *Interactions of water vapor with oxides at elevated temperatures.* Journal of Physics and Chemistry of Solids, 2005. **66**(2-4): p. 471-478.

[34] Stanislowski, M.et al.: *Reduction of chromium vaporization from SOFC interconnectors by highly effective coatings*. Journal of Power Sources **164**(2), 578-589 (2007).

[35] Froitzheim, J., Ravash, H., Larsson, E., Johansson, L.G., Svensson, J.E.: *Investigation of chromium volatilization from FeCr interconnects by a denuder technique*. Journal of The Electrochemical Society **157**(9), B1295 (2010).

[36] Areán, C.O., Viñuela, J.S.D.: *Structural study of copper-nickel aluminate ($Cu_xNi_{1-x}Al_2O_4$) spinels.* Journal of Solid State Chemistry **60**(1), 1-5 (1985).

[37] Zhou, C.G., Yu, J.S., Gong, S.K., Xu, H.B.: *Influence of water vapor on the isothermal oxidation behavior of low pressure plasma sprayed NiCrAlY coating at high temperature*. Surface & Coatings Technology **161**(1), 86-91 (2002).

[38] Kaplin, C., Brochu, M.: *Effects of water vapor on high temperature oxidation of cryomilled NiCoCrAlY coatings in air and low-SO_2 environments*. Surface and Coatings Technology **205**(17-18), 4221-4227 (2011).

[39] Nijdam, T.J., Sloof, W.G.: *Effect of reactive element oxide inclusions on the growth kinetics of protective oxide scales.* Acta Materialia **55**(17), 5980-5987 (2007).

[40] Nijdam, T.J., Sloof, W.G.: *Effect of Y distribution on the oxidation kinetics of NiCoCrAlY bond coat alloys.* Oxidation of Metals **69**(1-2), 1-12 (2007).

[41] Elrefaie, F.A., Smeltzer, W.W.: *Phase equilibria in the subsolidus region of the NiO–α-Al_2O_3 system between 1000 and 1920°C*. Oxidation of Metals **15**(5-6), 495-500 (1981).

[42] Belton, G.R., Jordan, A.S.: *Gaseous hydroxides of cobalt and nickel.* The Journal of Physical Chemistry **71**(12), 4114-4120 (1967).

[43] Swaddle, T.W., Lipton, J.H., Guastalla, G., Bayliss, P.: *The aqueous chemistry of chromium(III) above 100°C: Hydrothermal synthesis of chromium spinels.* Canadian Journal of Chemistry **49**(14), 2433-2441 (1971).

[44] Komlev, A.A., Gusarov, V.V.: *Mechanism of the nanocrystals formation of the spinel structure in the MgO-Al_2O_3-H_2O system under the hydrothermal conditions*. Russian Journal of General Chemistry **81**(11), 2222-2230 (2011).

[45] Zaplatynsky, I.: *Volatilization of oxides during oxidation of some superalloys at 1200°C*. Oxidation of Metals **11**(6), 289-305 (1977).

[46] Matsui, T., Kishida, R., Kim, J.-Y., Muroyama, H., Eguchi, K.: *Performance deterioration of Ni–YSZ anode induced by electrochemically generated steam in solid oxide fuel cells*. J. Electrochem. Soc. **157**(5), B776 (2010).

[47] Jiao, Z., Takagi, N., Shikazono, N., Kasagi, N.: *Study on local morphological changes of nickel in solid oxide fuel cell anode using porous Ni pellet electrod*e. Journal of Power Sources **196**(3), 1019-1029 (2011).

[48] Sehested, J.: *Sintering of nickel steam-reforming catalysts: Effects of temperature and steam and hydrogen pressures*. Journal of Catalysis **223**(2), 432-443 (2004).

[49] Opila, E.J. and D.L. Myers, *Alumina volatility in water vapor at elevated temperatures.* Journal of the American Ceramic Society, 2004. **87**(9): p. 1701-1705.

[50] Christensen, R.J., Tolpygo, V.K., Clarke, D.R.: *The influence of the reactive element yttrium on the stress in alumina scales formed by oxidation*. Acta Materialia **45**(4), 1761-1766 (1997)

[51] W.R. Chen, X. Wu, B.R. Marple, P.C. Patnaik, *The growth and influence of thermally grown oxide in a thermal barrier coating*, Surf. Coat. Technol., 201 (2006) 1074-1079.

[52] W.R. Chen, X. Wu, B.R. Marple, D.R. Nagy, P.C. Patnaik, *TGO growth behaviour in TBCs with APS and HVOF bond coats*, Surf. Coat. Technol., 202 (2008) 2677-2683.

[53] M.H. Sullivan, D.R. Mumm, *Vapor-phase-mediated phenomena associated with high temperature, high water content oxidation of MCrAlX bond coats*, Oxid. Met., (2014).

[54] B.A. Pint, A.J. Garratt-Reed, L.W. Hobbs, *Analytical electron-microscopy study of the breakdown of alpha-Al_2O_3 scales formed on oxide dispersion-strengthened alloys*, Oxid. Met., 56 (2001) 119-145.

[55] N.M. Yanar, F.S. Pettit, G.H. Meier, *Failure characteristics during cyclic oxidation of yttria stabilized zirconia thermal barrier coatings deposited via electron beam physical vapor deposition on platinum aluminide and on NiCoCrAlY bond coats with processing modifications for improved performances*, Metall. Trans. A, 37 (2006) 1563-1580.

[56] Nijdam, T.J. and W.G. Sloof, *Combined pre-annealing and pre-oxidation treatment for the processing of thermal barrier coatings on NiCoCrAlY bond coatings.* Surface & Coatings Technology, 2006. **201**(7): p. 3894-3900.

[57] T. Duong, A.M. Limarga, D.R. Clarke, *Diffusion of Water Species in Yttria-Stabilized Zirconia*, J. Am. Ceram. Soc., 92 (2009) 2731-2737.

[58] Munoz-Arroyo, R., et al., *Influence of composition and phase distribution on the oxidation behaviour of NiCoCrAlY alloys*, in *High Temperature Corrosion and Protection of Materials 5, Pts 1 and 2*, Materials Science Forum, 2001. **369-372**, p. 165-172.

[59] Bolt, P.H., et al., *A rutherford backscattering study of interfacial reactions of nickel and cobalt oxides with aluminum-oxide.* Applied Surface Science, 1993. **70-1**: p. 196-199.

[60] Nijdam, T.J., et al., *On the microstructure of the initial oxide grown by controlled annealing and oxidation on a NiCoCrAlY bond coating.* Oxidation of Metals, 2005. **64**(5-6): p. 355-377.

[61] V.E. Henrich, P.A. Cox, *Fundamentals of gas-surface interactions on metal oxides*, Appl. Surf. Sci., 72 (1993) 277-284.

[62] K.C. Hass, W.F. Schneider, A. Curioni, W. Andreoni, *First-principles molecular dynamics simulations of H_2O on α-Al2O3(0001)*, J. Phys. Chem. B, 104 (2000) 5527-5540.

[63] M. Michalik, M. Hansel, J. Zurek, L. Singheiser, W. Quadakkers, *Effect of water vapour on growth and adherence of chromia scales in high and low pO_2-environments at 1000 and 1050°C*, Mater. High Temp., 22 (2005) 39-47.

[64] Hansel, M., W.J. Quadakkers, and D.J. Young, *Role of water vapor in chromia-scale growth at low oxygen partial pressure.* Oxidation of Metals, 2003. **59**(3-4): p. 285-301.

[65] P.T. Moseley, K.R. Hyde, B.A. Bellamy, G. Tappin, *The microstructure of the scale formed during the high temperature oxidation of a fecralloy steel*, Corros. Sci., 24 (1984) 547-565.

[66] J. Doychak, M. Ruhle, *TEM studies of oxidized NiAl and Ni_3Al cross sections*, Oxid. Met., 31 (1989) 431-452.

[67] Sohlberg, K., S.J. Pennycook, and S.T. Pantelides, *Hydrogen and the structure of the transition aluminas.* Journal of the American Chemical Society, 1999. **121**(33): p. 7493-7499.

[68] Kramer, S.; Yang, J.; Levi, C. G.; Johnson, C. A., *Thermochemical interaction of thermal barrier coatings with molten CaO-MgO-Al_2O_3-SiO (CMAS) deposits*, Journal of the American Ceramic Society **89**, (2006), 3167-3175.

[69] S. Kraemer, J. Yang and C.G. Levi, *Infiltration-Inhibiting Reaction of Gadolinium Zirconate Thermal Barrier Coatings with CMAS Melt*s. Journal of the American Ceramic Society, **91**, (2008), 576-583.

[70] Limarga A.M., Iveland J., Gentleman M., Lipkin D.M., Clarke D.R.. *The use of Larson-Miller parameters to monitor the evolution of Raman lines of tetragonal zirconia with high temperature aging*, Acta Materialia **59**, (2011) 1162.

[71] Krogstad JA, Kramer S, Lipkin DM, Johnson CA, Mitchell DRG, Cairney JM, Levi CG. *Phase stability of t '-Zirconia-based thermal barrier coatings: mechanistic insights*. Journal of the American Ceramic Society, 2011. **94**: S168.

[72] Cairney, J. M.; Rebollo, N. R.; Ruhle, M.; Levi, C. G., *Phase stability of thermal barrier oxides: A comparative study of Y and Yb additions*. International Journal of Materials Research 2007, **98**, 1177-1187.

[73] Di Girolamo, G.; Blasi, C.; Pagnotta, L.; Schioppa, M., *Phase evolution and thermophysical properties of plasma sprayed thick zirconia coatings after annealing.* Ceramics International 2010, **36**, 2273-2280.

[74] Lipkin, D. M.; Krogstad, J. A.; Gao, Y.; Johnson, C. A.; Nelson, W. A.; Levi, C. G., *Phase Evolution upon Aging of Air-Plasma Sprayed t'-Zirconia Coatings: I – Synchrotron X-Ray Diffraction*. Journal of the American Ceramic Society 2013, 96, 290-298.

[75] Qu *et al*, Key Engineering Materials, **336-338** (2007) 2331-33.

[76] G. L. Catcher and T. M. Rearick, "*O-Anion Transport Measured in Several R2M2O7 Pyrochlores Using Perturbed-Angular Correction Spectroscopy*," Physical Review B, **B52**, (1995) 9890–99.

LIST OF ACRONYMS AND ABBREVIATIONS

TGO	Thermally grown oxide
TBC	Thermal barrier coating
HHC	High hydrogen content
CMAS	A glass deposit contain the primary constituents Ca, Mg, Al, and Si
CMAF	A glass deposit contain the primary constituents Ca, Mg, Al, and Fe
YSZ	Yttria stabilizd zirconia
MCrAlX	A metallic overall coating or bond coating contain the primary constituents M = Ni, Co, Cr, Al and a reactive elements X such as yttrium or hafnium
IGCC	Integrated gasification combined cycle
SEM	Scanning electron microscopy
EDS	Energy dispersive spectroscopy
BSE	Back-scattered electrons
XRD	X-ray Diffraction
STEM	Scanning transmission electron microscopy
GBRs	Grain boundary ridges
LMP	Larson Miller parameter
GIXRD	Grazing incedence X-ray diffraction
HTXRD	High temperature X-ray diffraction
TEC	Thermal expansion coefficient

TABLES

Table 1: Compositions, in weight percent, of alloys prior to oxidation (M = Ni and Co, X = Y or Re). An asterisk indicates that data were collected by the authors using EDS at 15 kV. All other numbers are supplied by manufacturers. EDS error is +/- 1%.

				Composition (wt%)								
Name	Supplier	Type	Phase	Al	Cr	Fe	Co	Ni	Mo	Y	Zr	Re
NiCoCrAlRe	*Siemens*	Sprayed Bond Coat	Total*	10.9	16.0		23.4	48.8				0.8
			β*	18.4	7.1		16.2	58.3				0.0
			γ' *	5.2	22.0		29.5	41.6				1.7
			M,Re-Rich*	0.4	68.2		5.8	5.6				20.1
CoNiCrAlY Amdry 365	*Sulzer Metco*	Sprayed Bond Coat	Total*	8.6	20.7		38.3	31.9		0.5		
NiCoCrAlY Amdry 386	*Sulzer Metco*	Sprayed Bond Coat	Total*	13.4	16.9		22.2	46.7		0.8		
CoNiCrAlY-127	*Praxair*	Cast Bond Coat	Total	8.0	21.0		38.5	32.0		0.5		
			β*	17.3	12.8		28.5	41.3		0.0		
			γ' *	6.1	24.8		39.0	30.1		0.0		
			M,Y-Rich*	7.2	9.1		24.9	40.8		18.0		
NiCoCrAlY-171	*Praxair*	Cast Bond Coat	Total	12.5	17.0		23.0	47.0		0.5		
			β*	17.3	12.2		18.3	52.1		0.0		
			γ' *	6.6	26.3		26.3	40.8		0.0		
			M,Y-Rich*	6.4	8.3		13.8	50.4		21.1		

Table 2: Compositions of bottom ash (obtained from Jeff Bons, OSU), in terms of elemental constituents.

Wt%	Spectrum 1	Spectrum 2	Spectrum 3	Average
Al	9.07	9.40	8.97	9.15
Ca	4.93	5.20	5.01	5.05
Fe	7.39	8.90	7.45	7.91
K	1.52	1.77	1.52	1.60
Mg	0.80	0.76	0.79	0.78
Na	2.56	2.24	2.15	2.30
O	49.03	45.68	47.35	47.35
Si	25.91	26.49	25.56	25.99
Ti	0.35	0.46	0.36	0.39

Table 3: Compositions of bottom ash (obtained from Jeff Bons, OSU), in terms of oxide constituents.

Compound	Wt%
Al2O3	17.28
CaO	7.23
Fe2O3	11.31
K2O	1.93
MgO	1.30
Na2O	3.10
SiO2	56.31
TiO2	0.65

Table 4: Compositions of CMAS that believed to be relevant for aero-propulsion turbines and IGCC turbine systems, in terms of the mol% of the constituent cations.

	Constituent Cations (mol%)						
	Si	**Ca**	**Mg**	**Al**	**Na**	**K**	**Fe**
Aero-Propulsion	50	38	5	4	1	1	1
IGCC	6	12	5	4			20

Table 5: Average CMAS penetration and residual glass for YSZ and the rare-earth zirconates.

Ceramic Oxide	Avg. CMAS Penetration Depth (μm)	Avg. Thickness of Residual CMAS Glass Above Oxide (μm)
8YSZ	500	0
$Gd_2Zr_2O_7$	90	75
$GdYbZr_2O_7$	75	80
$5Yb\text{-}SrZrO_3$	55	110

Table 6: EDS results displaying the composition of phases following CMAF infiltration into YSZ and $Sm_2Zr_2O_7$ microstructures. The relevant phases are the coating and as many as two glass phases, classified as dark and light.

	Composition (Wt %) by EDS											
	APS Standard YSZ			Segmented 1 YSZ		Segmented 2 YSZ			AR $Sm_2Zr_2O_7$	APS $Sm_2Zr_2O_7$ ($avg_{Infiltrated\ 1,2}$)		
	Coating	Light Glass	Dark Glass	Coating	Dark Glass	Coating	Light Glass	Dark Glass	Coating	Coating	Light Glass	Dark Glass
Y	3.2	0.3	1.5	4.7	2.2	4.3	3.6	1.7	-	-	-	-
Sm	-	-	-	-	-	-	-	-	46.7	43.8	28.3	26.5
Zr	64.9	3.7	9.0	66.4	6.0	63.9	8.8	4.4	32.0	33.6	16.4	19.4
O	27.6	34.4	41.6	28.7	44.3	27.9	36.4	43.1	21.3	21.6	27.7	29.1
Ca	1.1	0.6	13.1	0.2	13.0	1.1	2.2	12.8	0.0	0.5	6.6	6.4
Mg	0.2	0.6	2.2	0.0	3.1	0.2	2.3	2.0	0.0	0.1	0.7	1.3
Al	0.0	1.7	5.3	0.0	7.5	0.1	2.9	5.9	0.0	0.0	1.6	1.7
Fe	3.0	57.9	13.9	0.0	10.2	2.6	40.3	17.3	0.0	0.4	17.4	13.6
Si	0.0	0.9	13.5	0.0	13.9	0.0	3.5	12.9	0.0	0.0	1.3	2.1

FIGURES

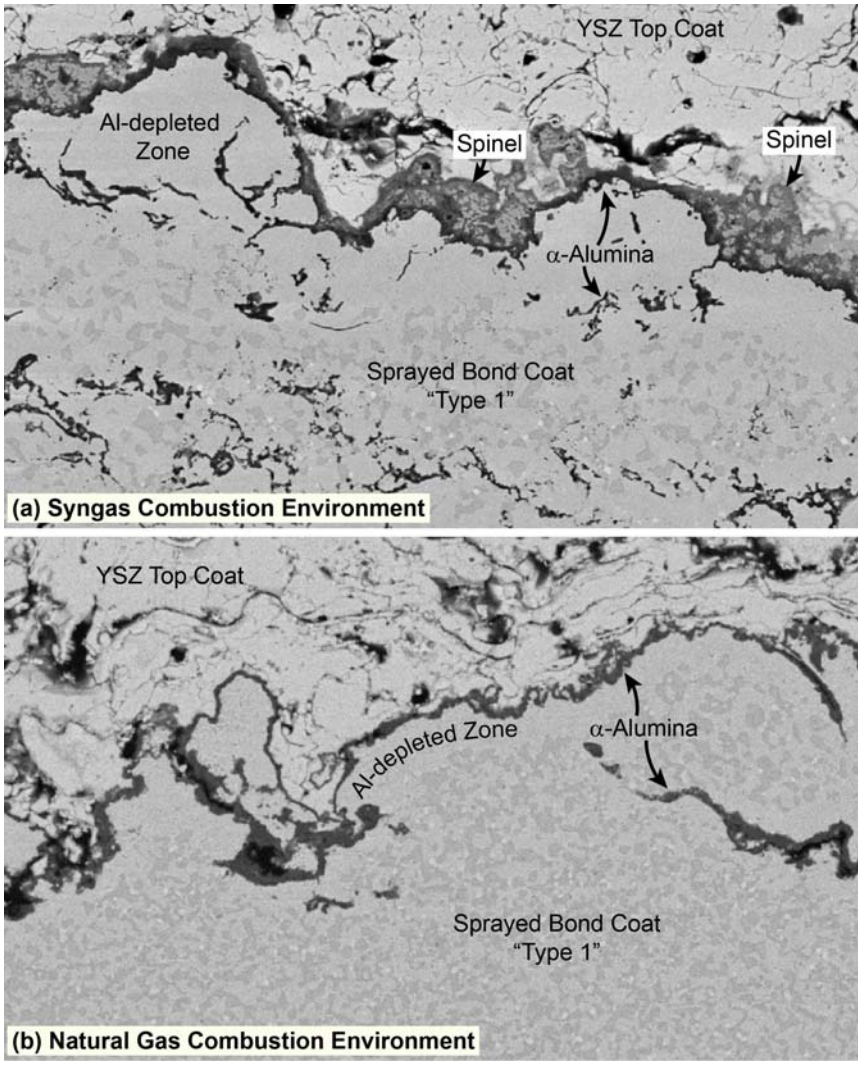

Figure 1: Cross-section images of TBC-bond coat interfaces resulting from field tests of industrial turbine blade material systems, courtesy A. Kulkarni, Seimens Power Generation [3]. TGO develops dissimilarly on equivalent TBC systems when combusting **(a)** syngas versus **(b)** natural gas. A second set of images (not shown) indicate similar differences for a second, "Type 2" bond coat composition as well.

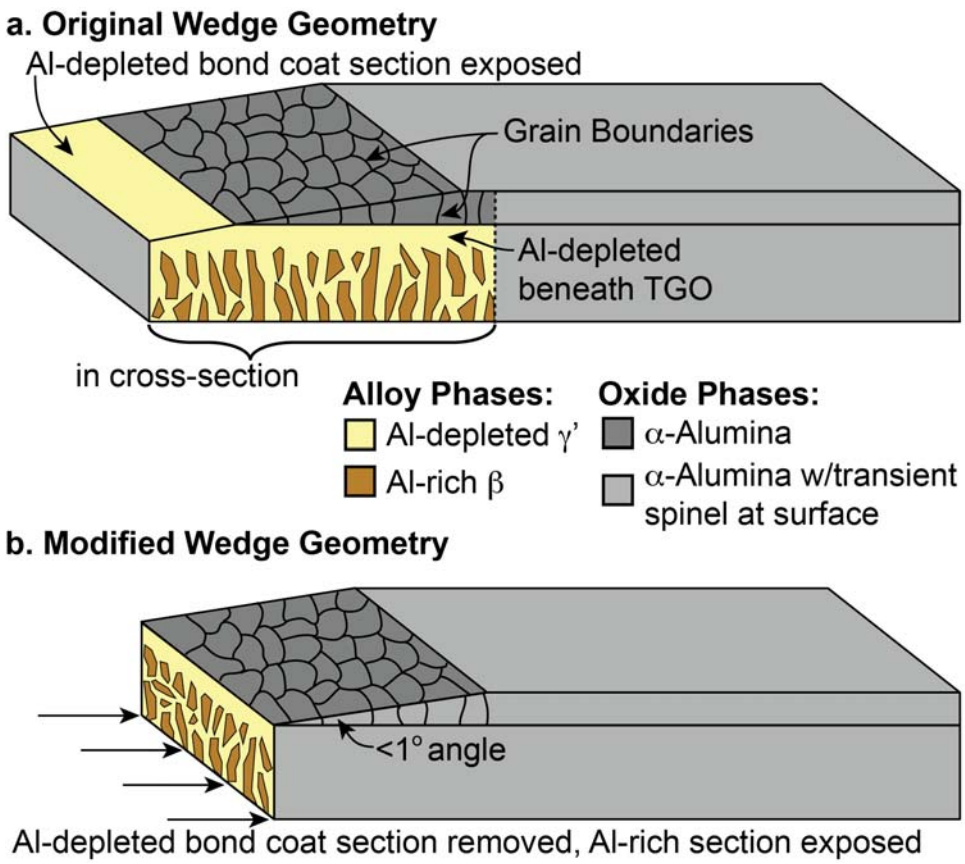

Figure 2: Schematics depicting a) "original" and b) "modified" wedge geometries, as they appear after taper-polishing, but before the final re-oxidation step.

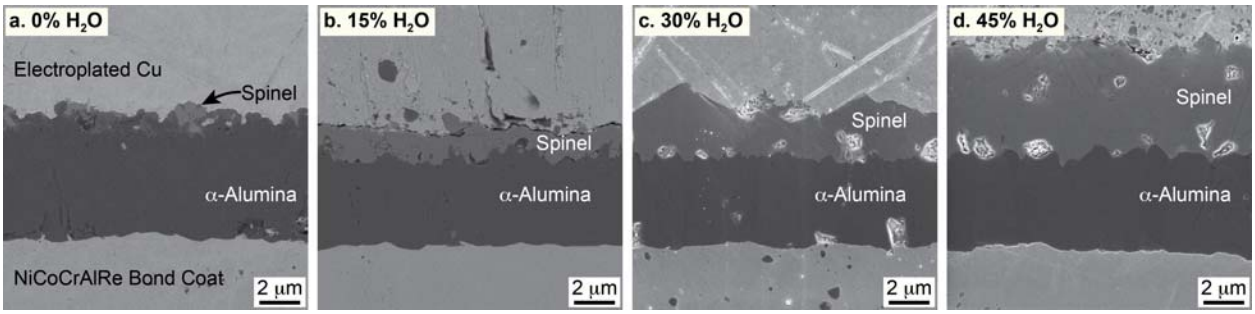

Figure 3: Cross-sectional BSE micrographs (5 kV) of sprayed NiCoCrAlRe (with superalloy substrate attached) exposed for 300 h at 1125 °C in a) 0%, b) 15%, c) 30%, and d) 45% H_2O. Electroplated copper was added to aid in polishing.

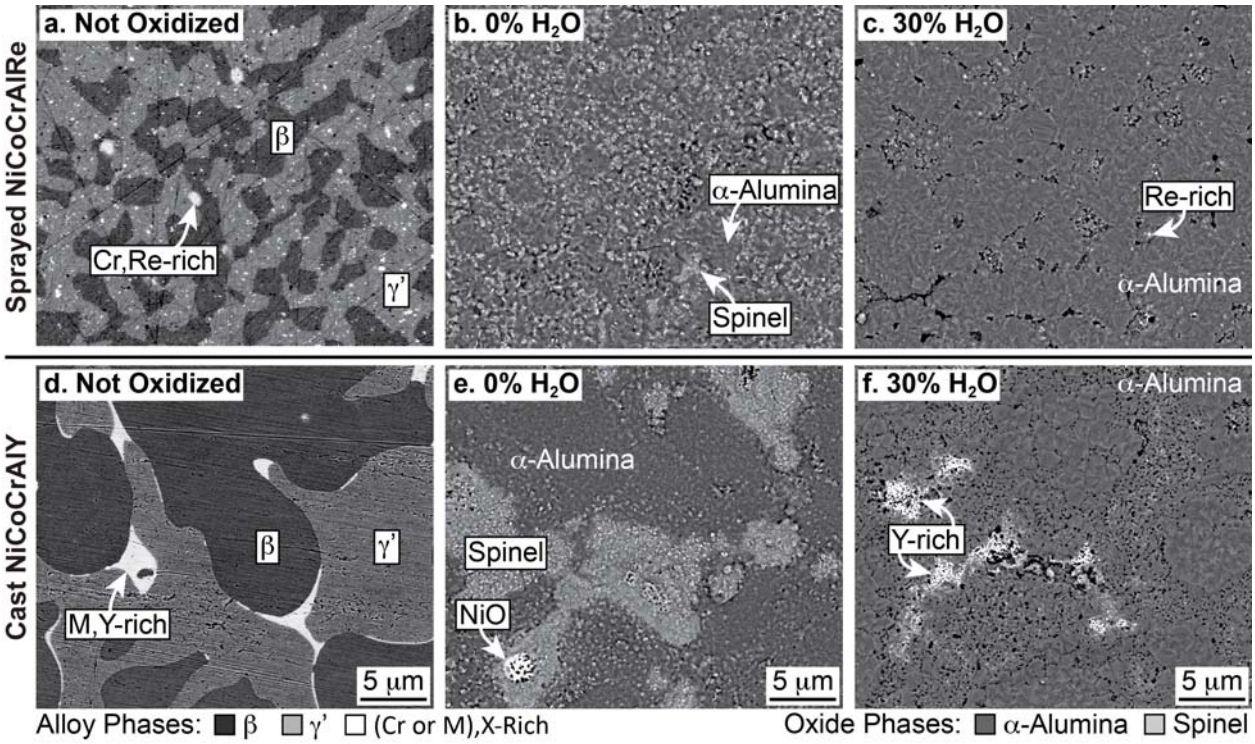

Figure 4: Plan view BSE micrographs (7 kV) of sprayed NiCoCrAlRe with the superalloy substrate removed (top row) and cast NiCoCrAlY (bottom). The exposures are: not oxidized (a. and d.), and oxidized for 100 h at 1125 °C in 0% H_2O (b. and e.) and 30% H_2O (c. and f.).

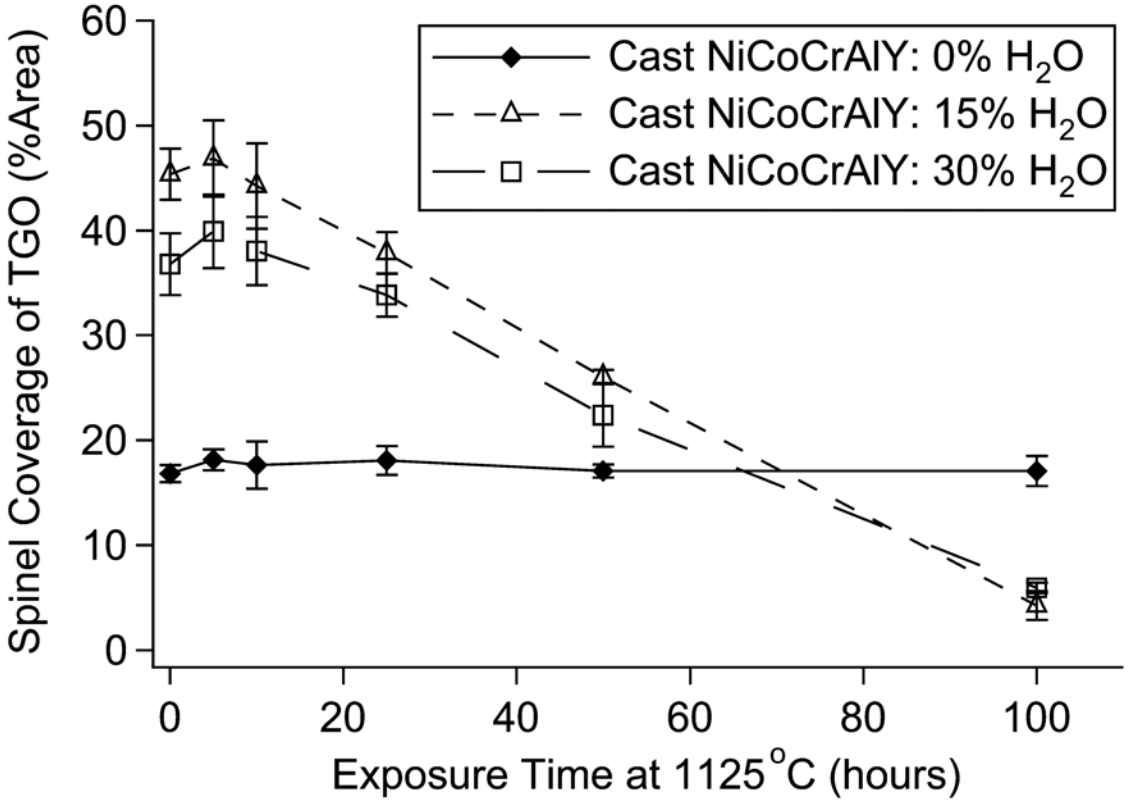

Figure 5: Cast NiCoCrAlY TGO spinel coverage vs. exposure time for three different water vapor environments.

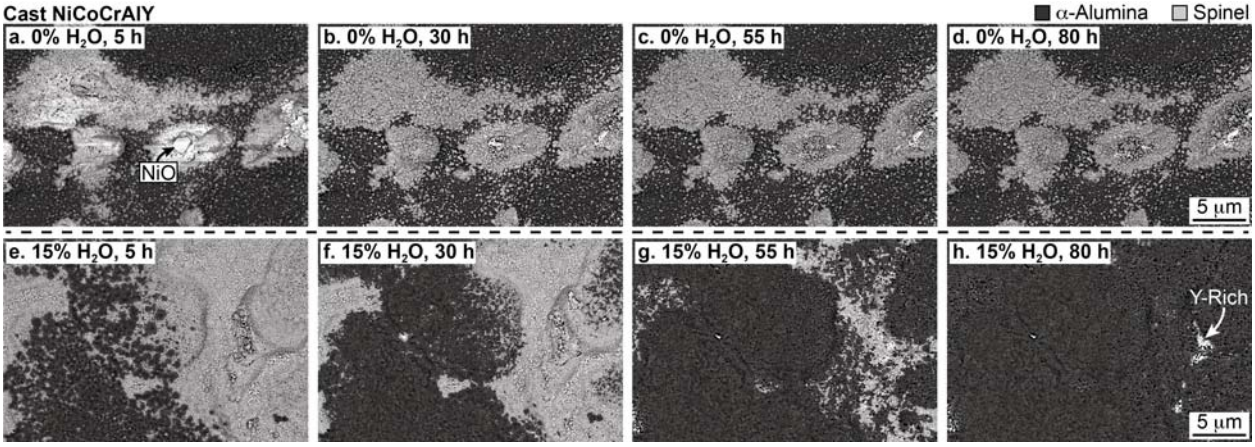

Figure 6: Plan view BSE time-lapse micrographs (5 kV) of cast NiCoCrAlY TGO from 5 (a. and e.) to 30 (b. and f.), to 55 (c. and g.), to 80 h (d. and h.) in 0% and 15% H_2O, respectively.

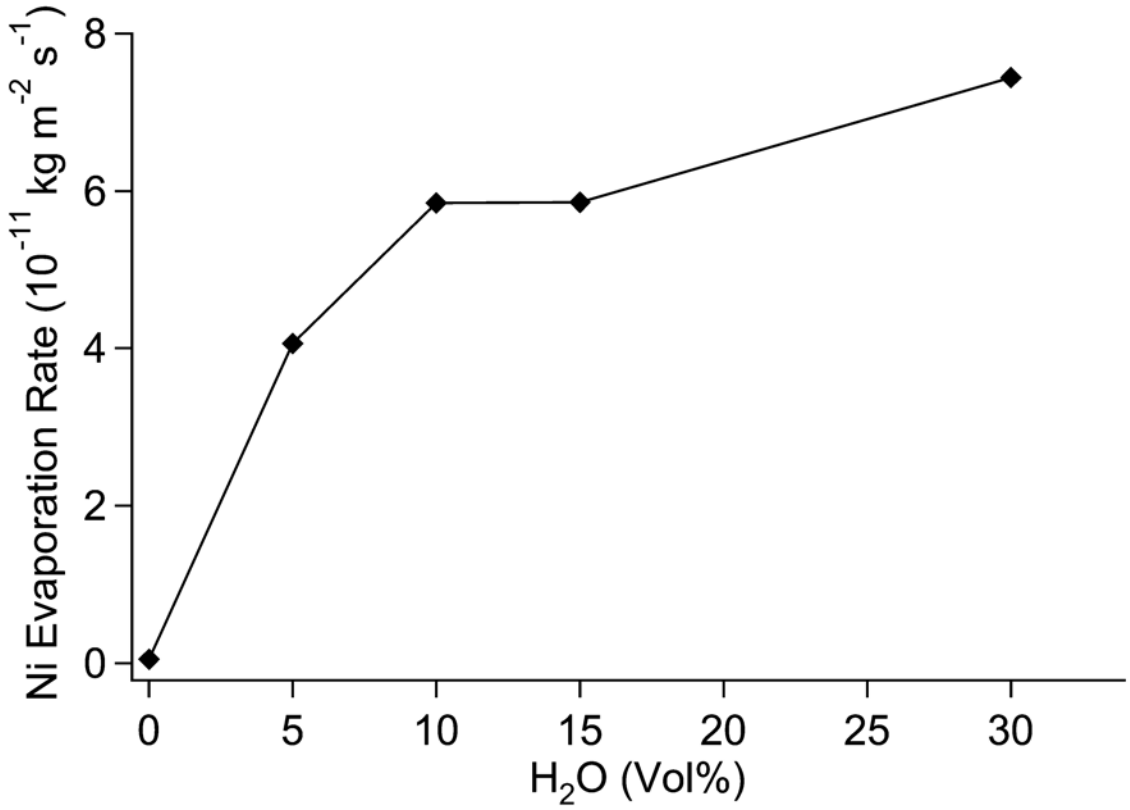

Figure 7: Evaporation rate of Ni from pre-fabricated $NiAl_2O_4$ pellets as a function of H_2O vol% at 1125 ^{0}C and 200 sccm gas flow rate.

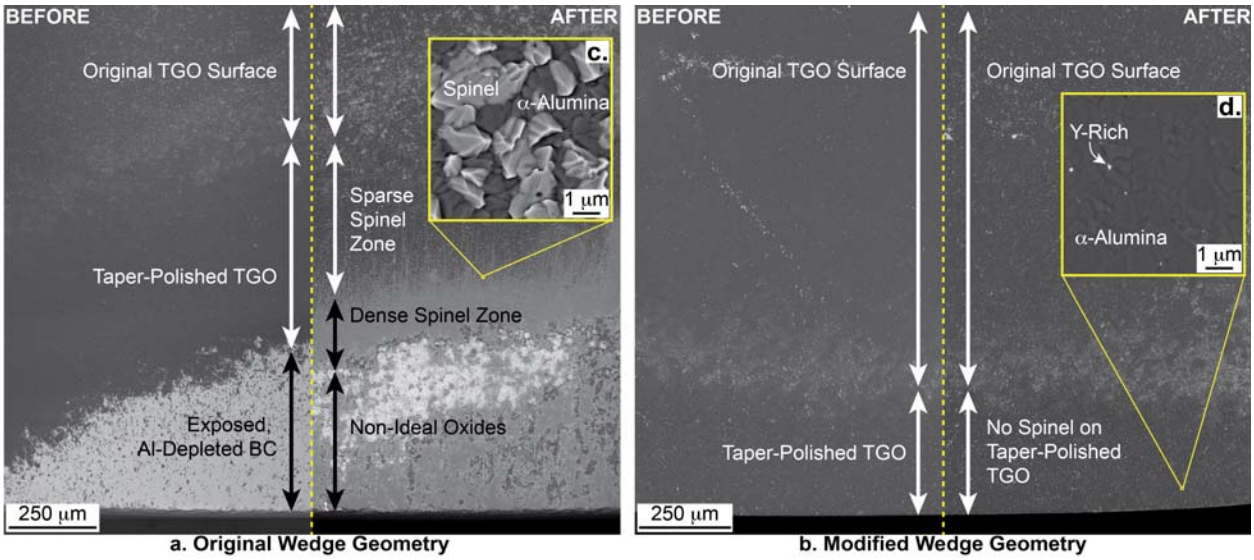

Figure 8: Plan view BSE images (5 kV) of taper-polished, cast NiCoCrAlY before and after 4 h re-oxidation in 15%H_2O using the a) original and b) modified wedge geometry. In each case, the same sample was imaged before (left) and after (right) re-oxidation. High mag images appear as insets (c. and d.). The initial oxidation was 100 h in 0% H_2O.

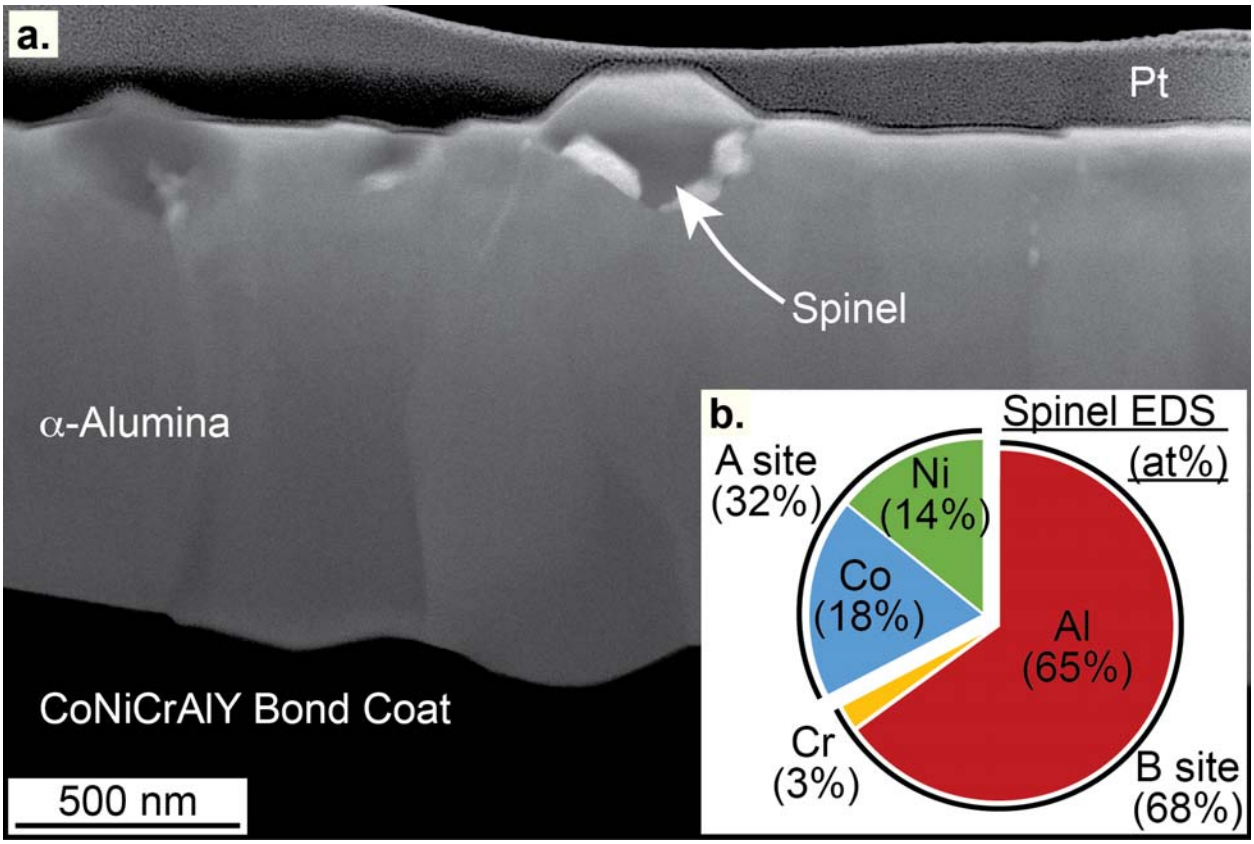

Figure 9: a) Thin foil specimen from a cast CoNiCrAlY sample (100 h oxidation in 0% H_2O, 4 h re-oxidation in 15% H_2O) is viewed in cross-section using dark field STEM mode (30 kV). The inset (part b.) reports average EDS values for spinel grains analyzed on thin foil specimens (15 kV). EDS error is +/- 1%.

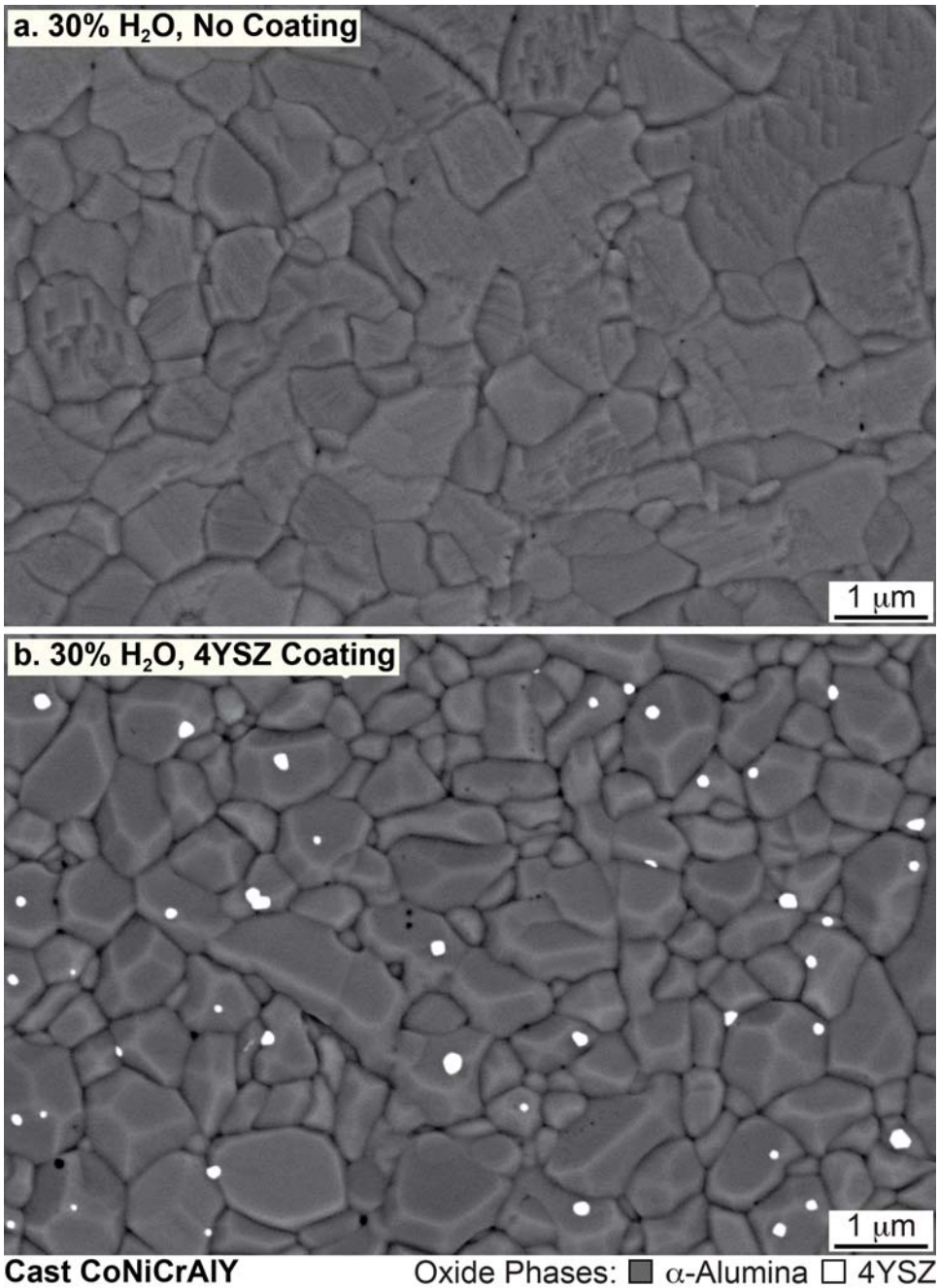

Figure 10: Plan view BSE micrographs (5 kV) of cast CoNiCrAlY modified wedges having a) no coating and b) 4YSZ coating, show no new oxide growth following 200 h, 30% H_2O re-oxidation.

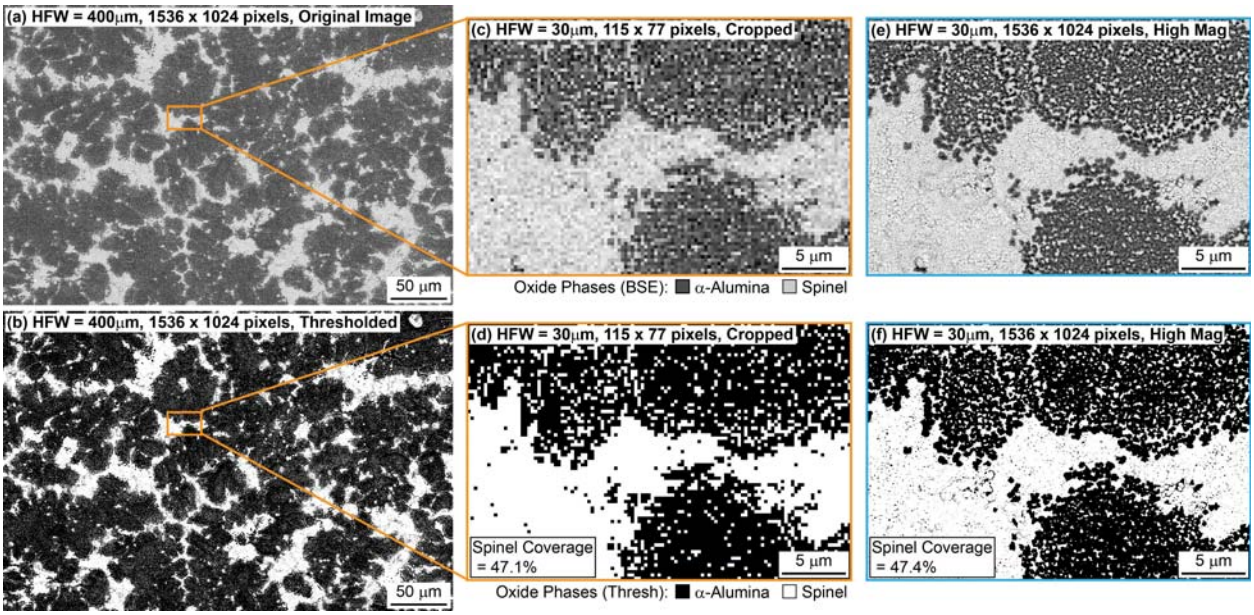

Figure 11: A demonstration of the thresholding technique used to quantify the surface area coverage of spinel and alumina on low magnification BSE images. A 400 μm HFW image **(a)**, when thresholded **(b)**, canvases enough area to be representative of the macrostructure, while still accurately capturing microstructure. A 30 x 20 μm^2 area cropped from the larger image **(c and d)** produces coverage values within 1% of those derived from a higher resolution 30 μm HFW image of the same location **(e and f)**.

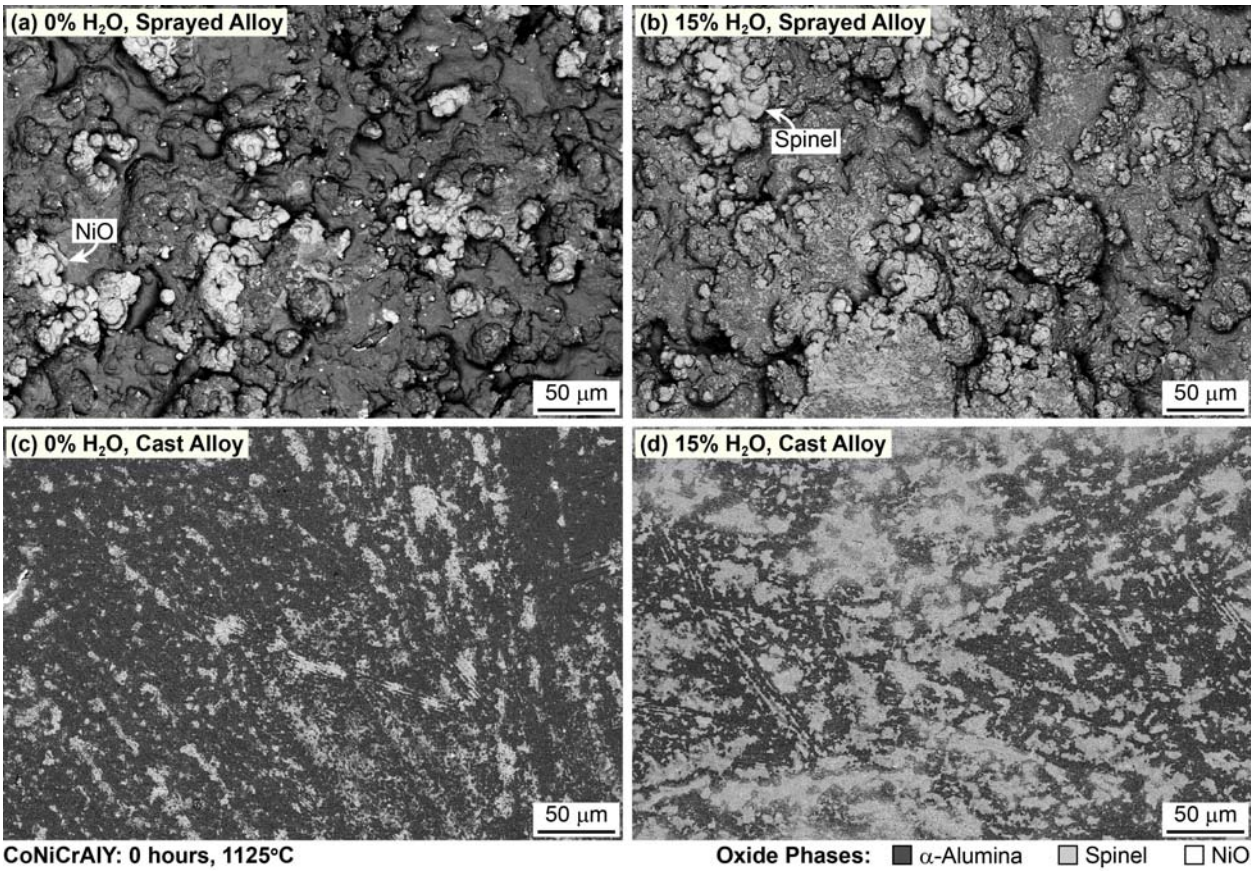

Figure 12: A comparison of sprayed CoNiCrAlY TGO grown in **(a)** 0% and **(b)** 15% H_2O, versus cast CoNiCrAlY grown in **(c)** 0% and **(d)** 15% H_2O for "zero hours" at 1125 ^{o}C. BSE images, 5 kV, 400 μm HFW.

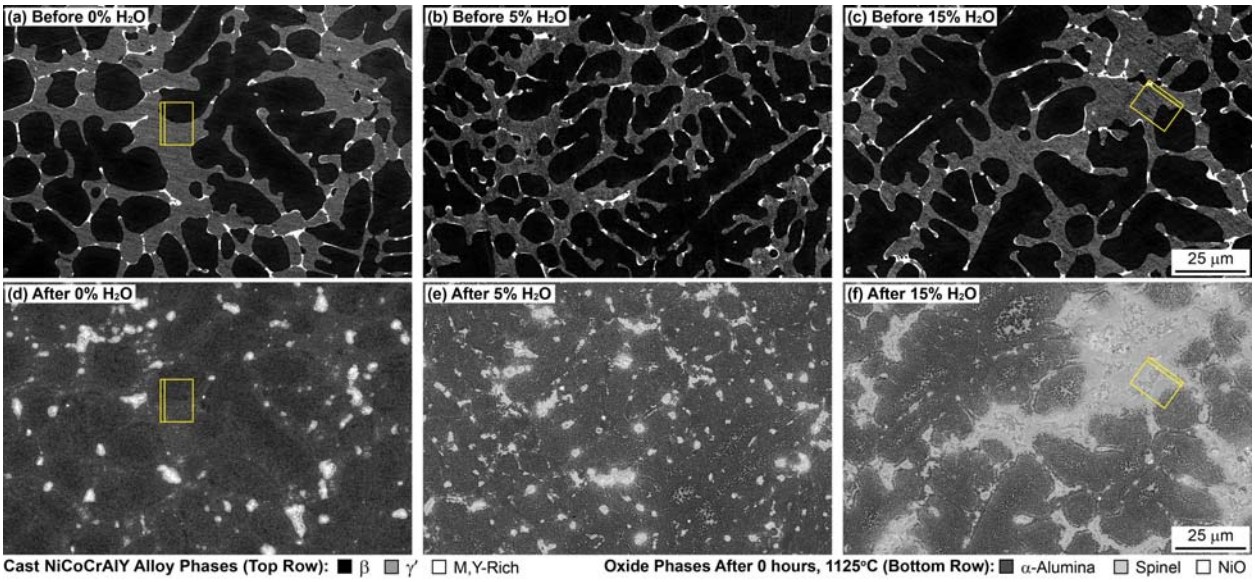

Figure 13: Before-after 150 μm HFW BSE plan view images (5 kV) of cast NiCoCrAlY TGO grown in 0% (before **a** vs. after **d**), 5% (**b** vs **e**) and 15% H_2O (**c** vs **f**) for "zero hours" at 1125 °C. The rectangles overlaid on the micrographs represent the site-specific areas evaluated in Fig.5a-f.

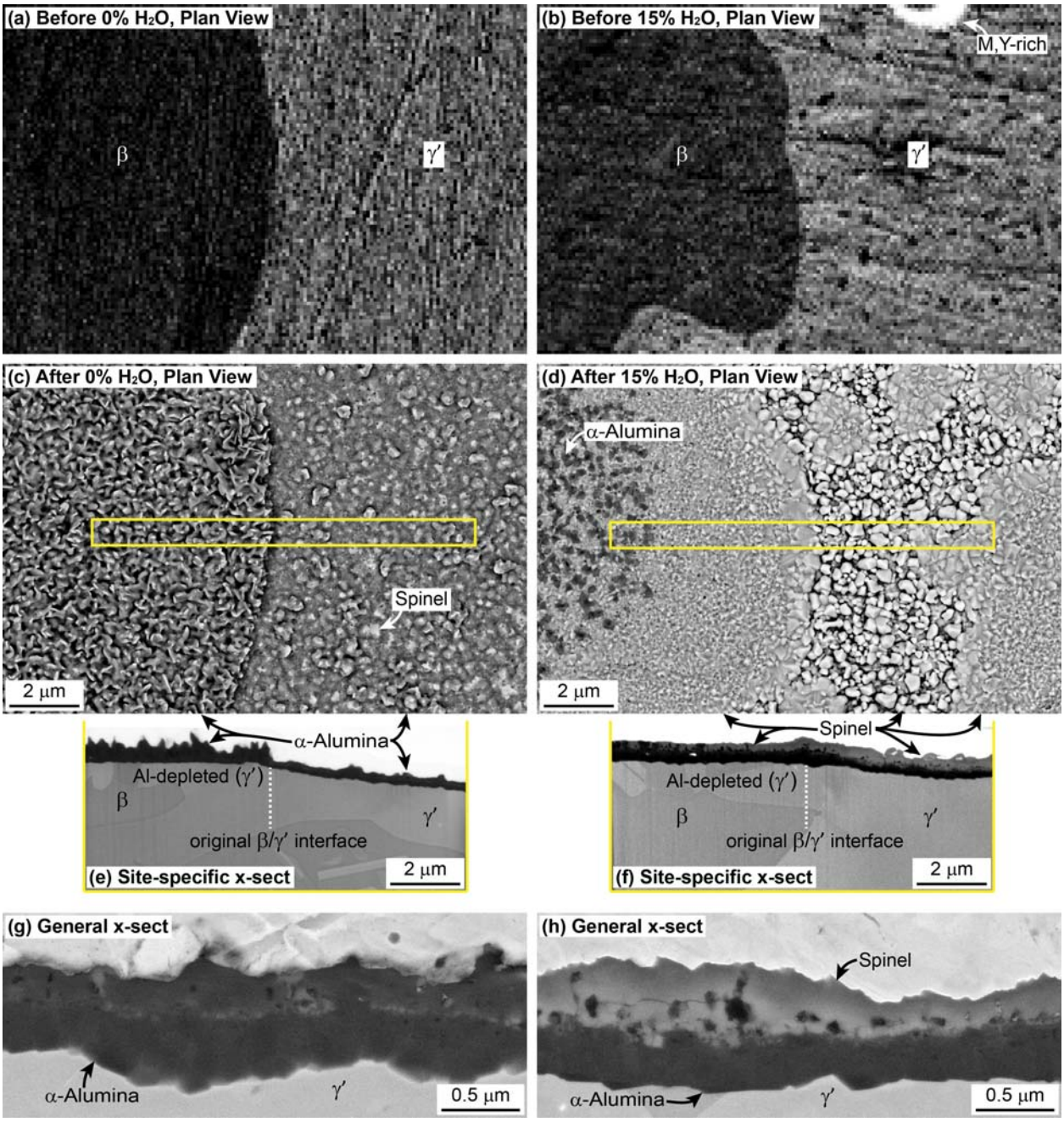

Figure 14: Locations indicated by outlined rectangles in Fig.4 are represented as higher magnification images of NiCoCrAlY before (**a** and **b**) and after (**c** and **d**) oxidation for "zero hours" at 1125 °C in 0% and 15% H_2O, respectively. Thin foil cross-sections that spanned what was originally a β/γ' interface **(e** and **f)**, were prepared from the indicated locations. General cross-sections **(g** and **h)**, prepared via grinding and polishing from equivalent specimens, are included to show TGO morphology in higher resolution. All images 5 kV, BSE.

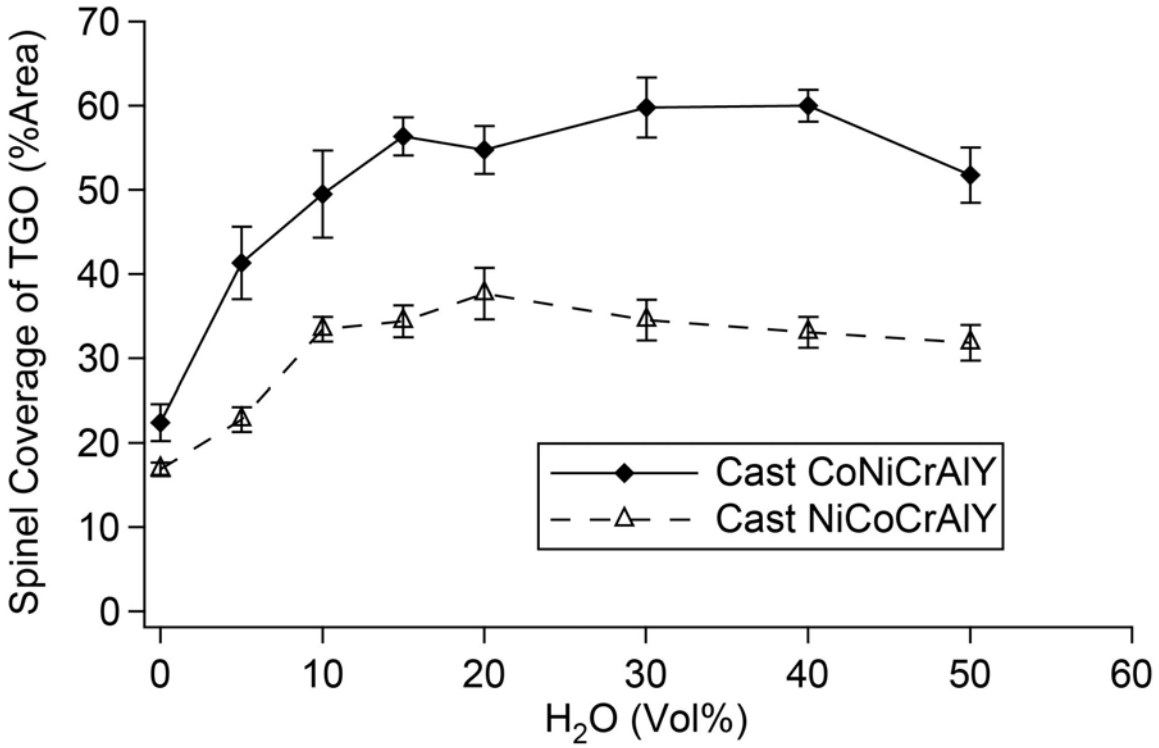

Figure 15: Spinel surface area coverage plotted as a function of water vapor content for cast CoNiCrAlY and NiCoCrAlY. Data are derived from 400 μm HFW BSE images (5 kV) that were thresholded. All exposures were held at 1125 °C for "zero hours."

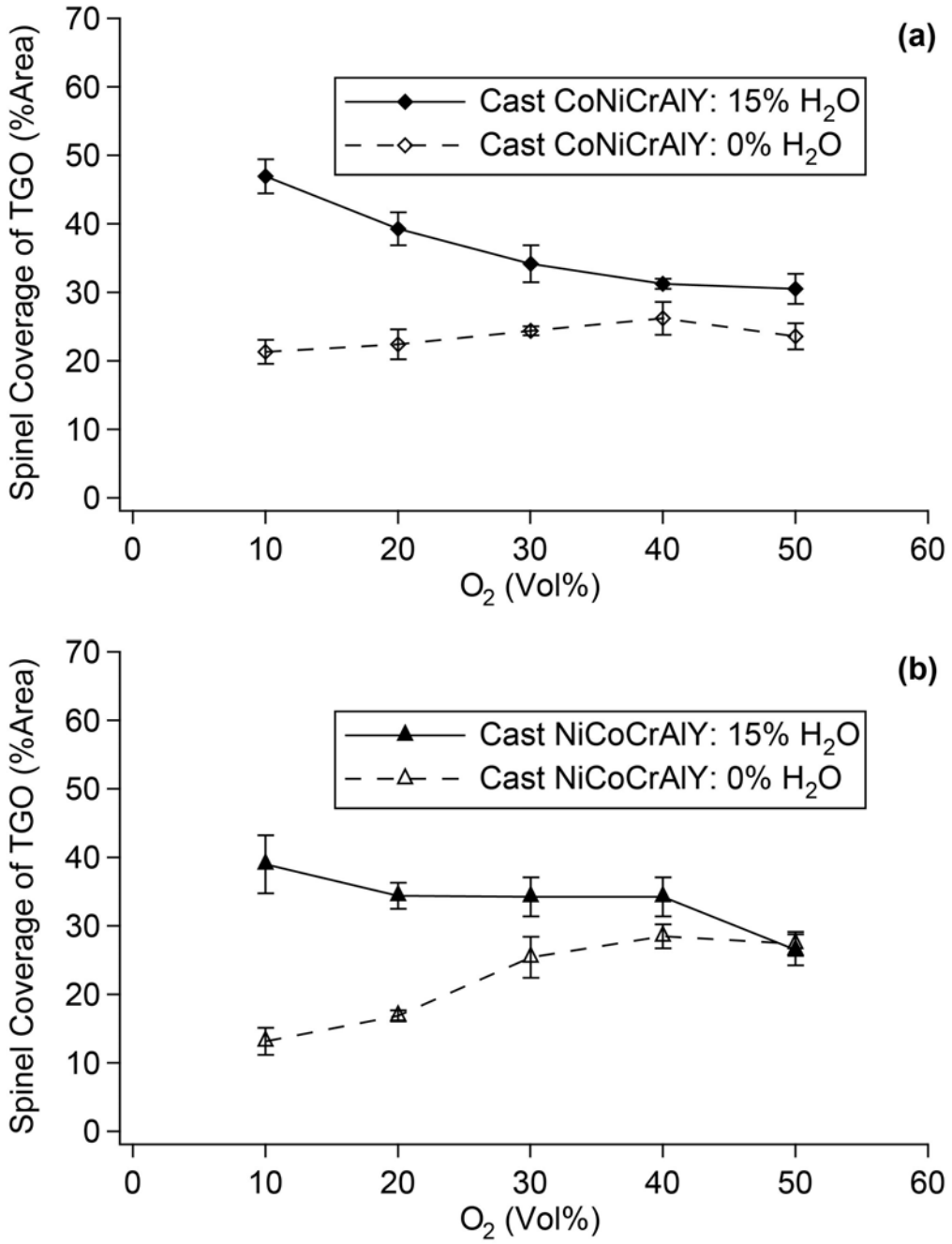

Figure 16: Spinel surface area coverage plotted as a function of oxygen content for cast **(a)** CoNiCrAlY and **(b)** NiCoCrAlY. Data are derived from 400 μm HFW BSE images (5kV) that were thresholded. All exposures were held at 1125 °C for "zero hours."

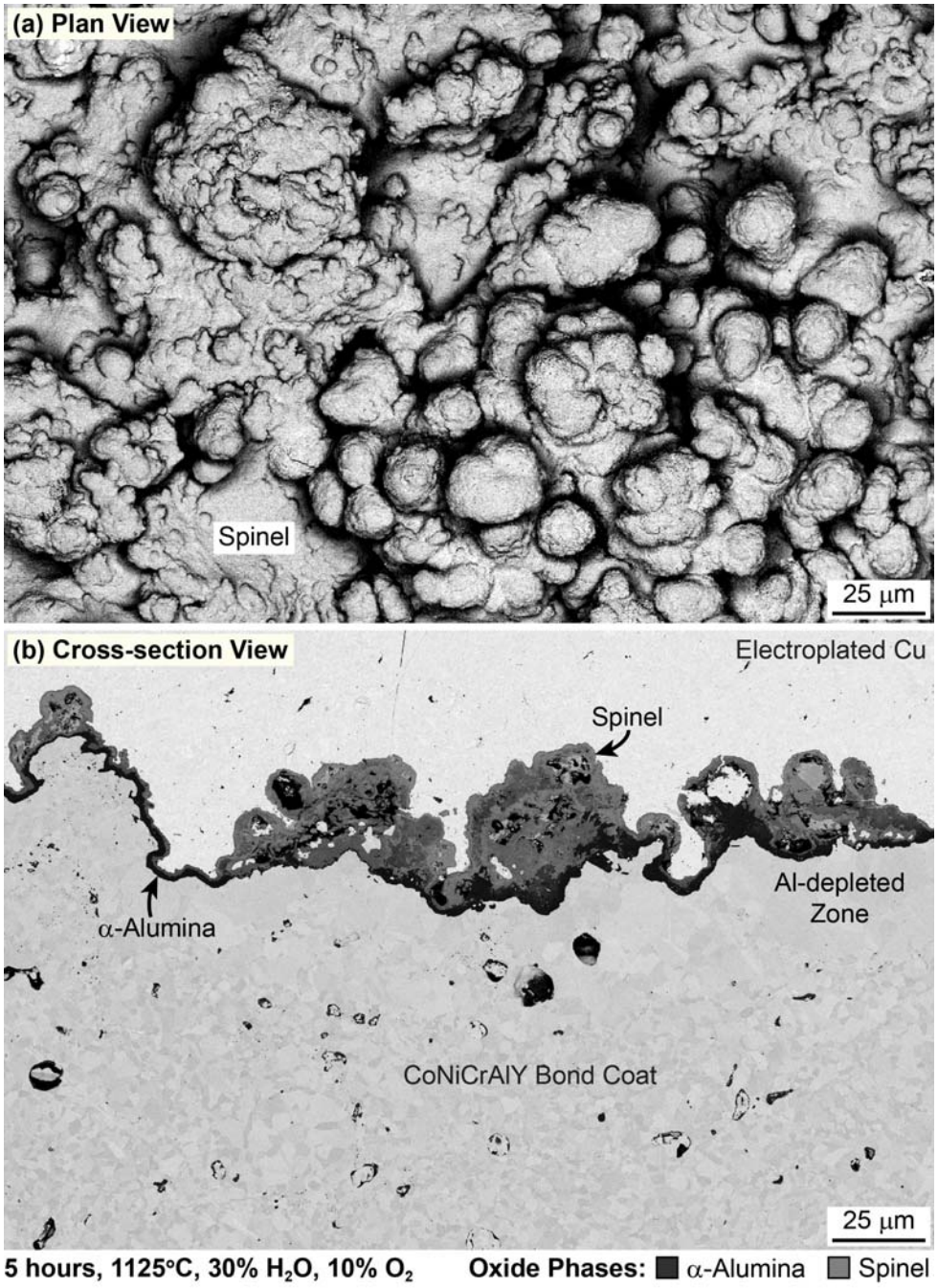

Figure 17: Sprayed CoNiCrAlY TGO grown in 30% H_2O and 10% O_2 for 5 h at 1125 °C, seen in **(a)** plan view and **(b)** cross-section, representing the most extreme case of transient spinel growth in this study. BSE images, 5kV.

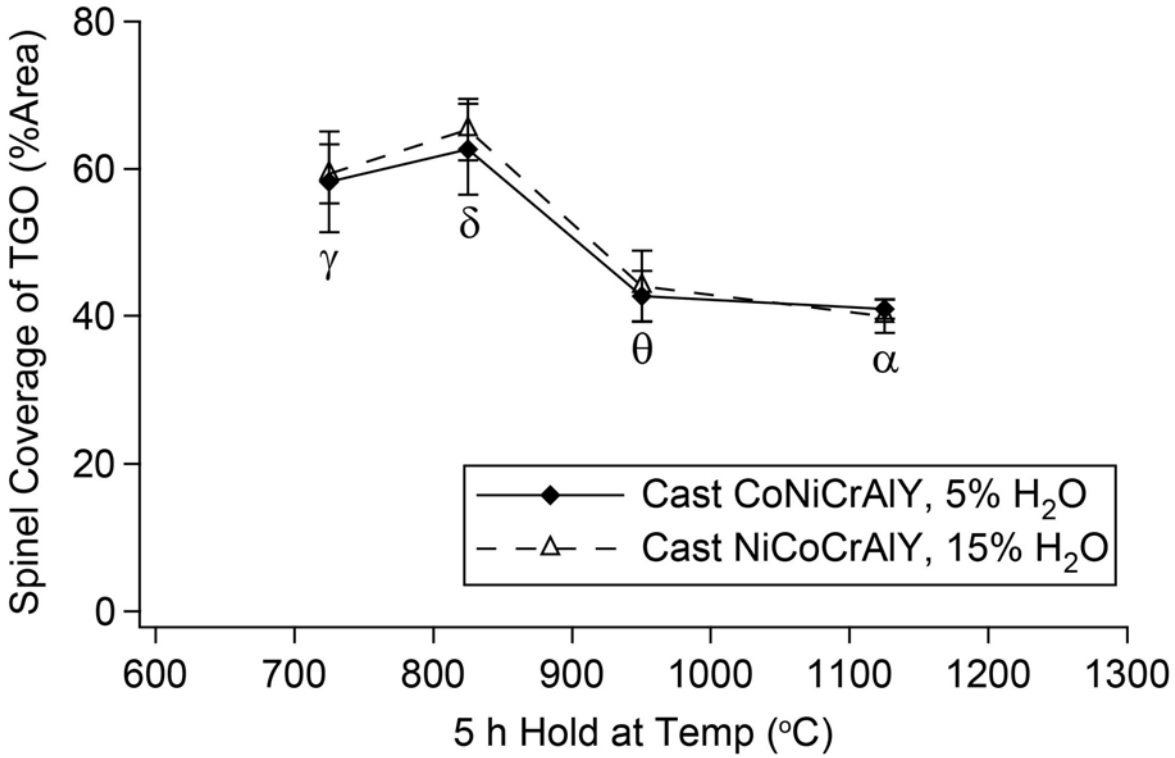

Figure 18: Spinel surface area coverage plotted as a function of the 5 h holding temperature for cast NiCoCrAlY (15% H_2O) and cast CoNiCrAlY (5% H_2O). The Greek symbols refer to the metastable alumina phase present at each temperature. Note that after holding 5 h, each specimen was ramped to 1125 ºC and then back to room temp so that all experiments had equal duration.

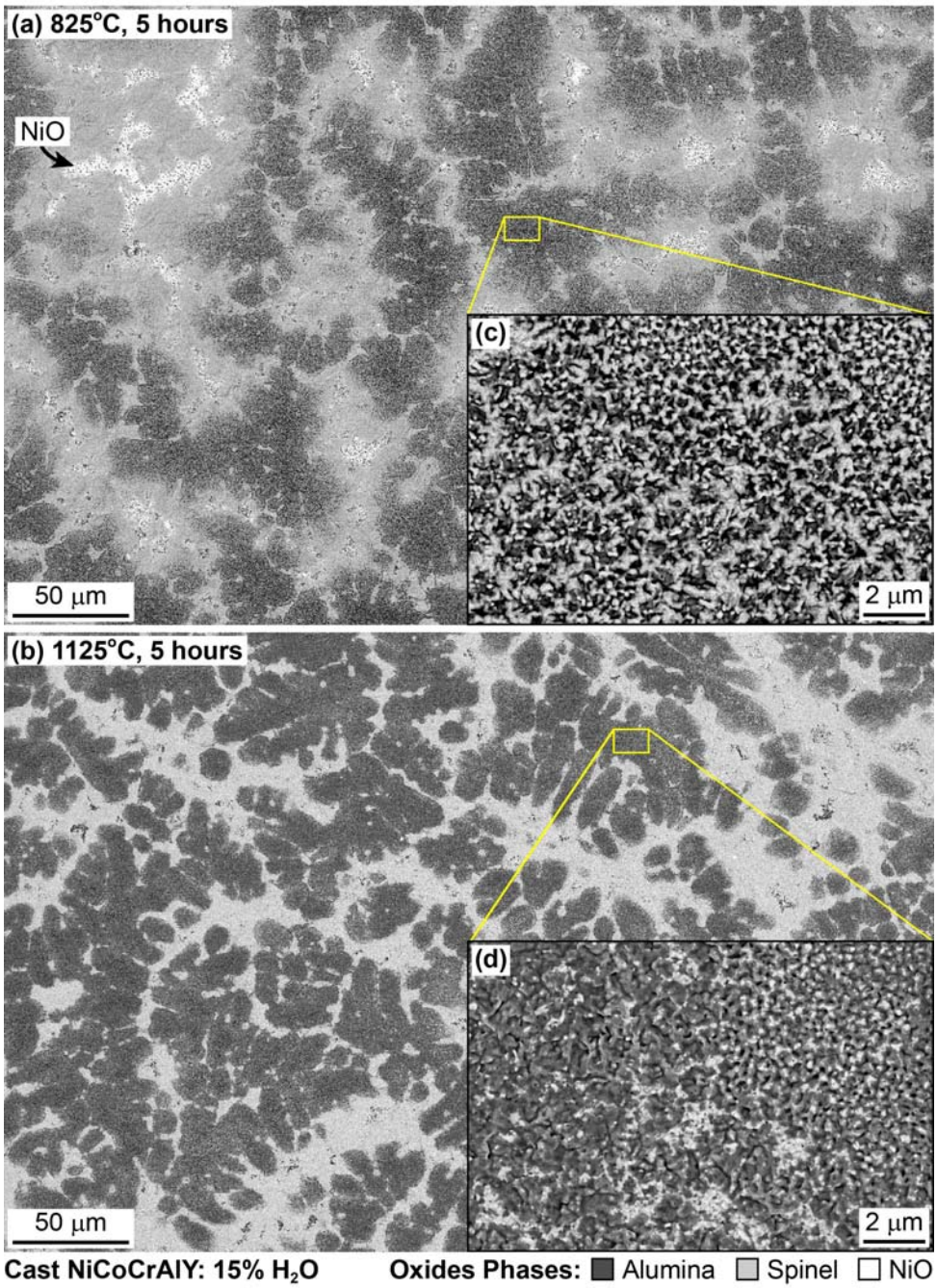

Figure 19: Plan view, 400 μm HFW micrographs of NiCoCrAlY bond coats held for 5 h at **(a)** 825 °C and **(b)** 1125 °C (the 825 °C sample was ramped to 1125 °C and back to room temperature following its hold). The inset micrographs (**c** and **d**) are representative high magnification views of TGO that grew above the bond coat's β alloy phase.

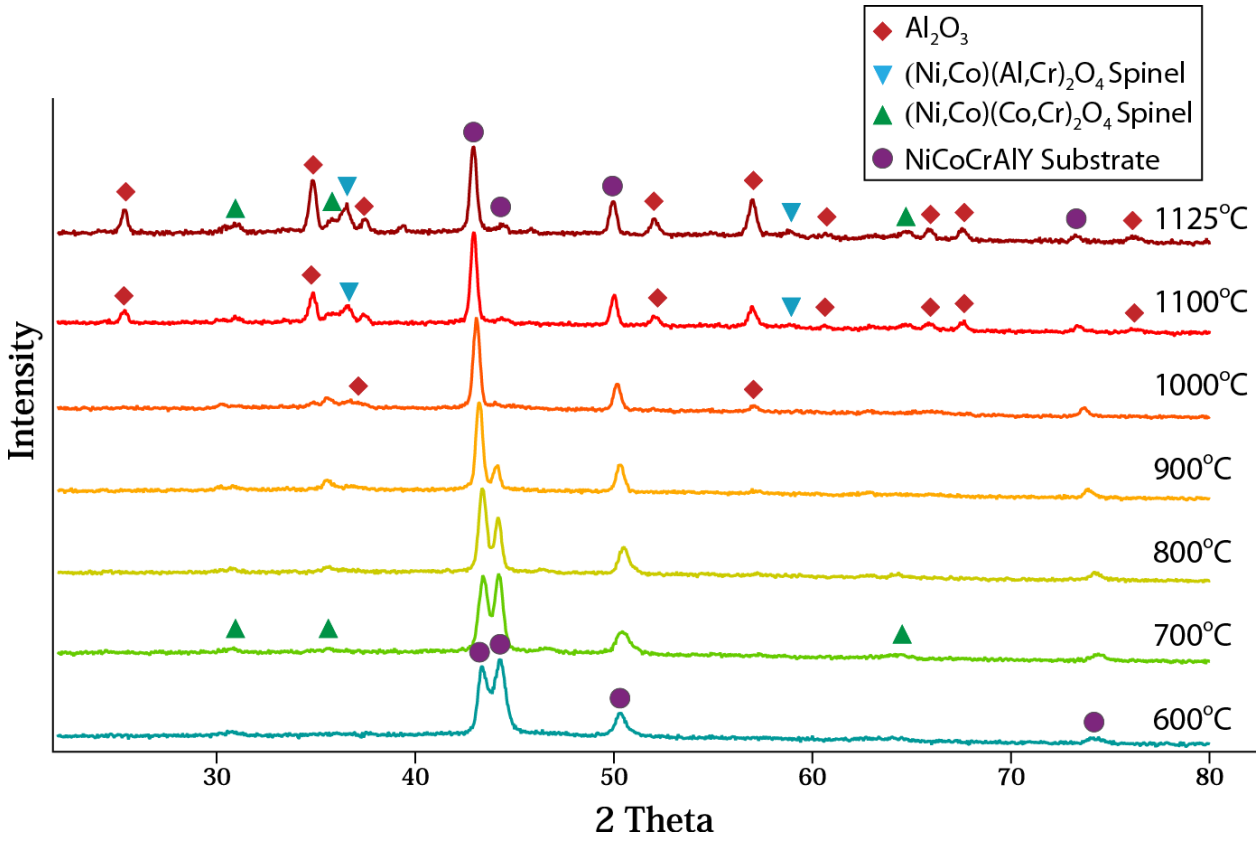

Figure 20: *In situ* NiCoCrAlY TGO development, tracked with HTXRD from 600-1125°C.

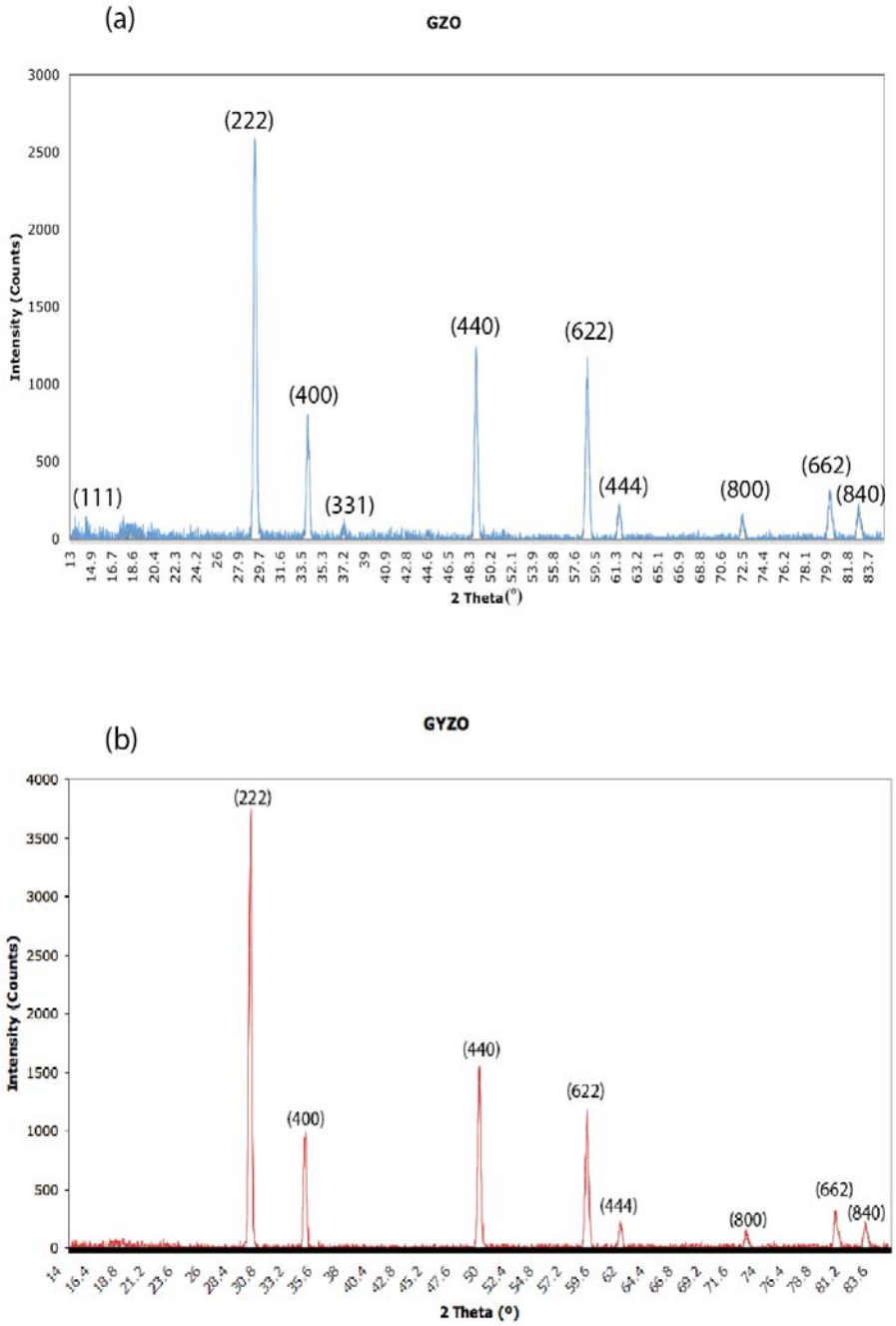

Figure 21: XRD Patterns acquired from the (a) GZO, and (b) GYZO specimen. (hkl) indices are indicated.

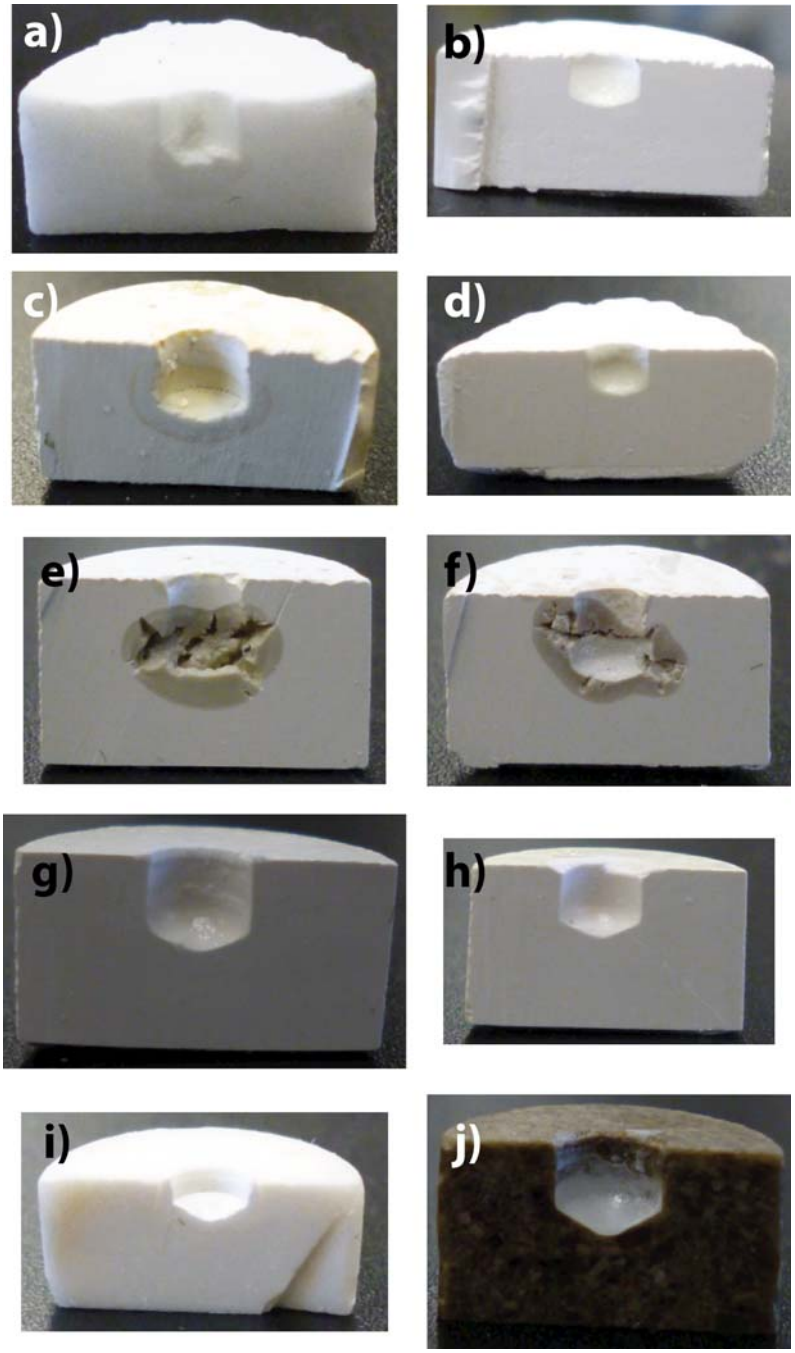

Figure 22: Images taken from the cross-sectioned pellets showing the CMAS infiltration: (a) Monazite, (b) Mullite, (c) $ZrSiO_4$, (d) $CaZrO_3$, (e) $BaZrO_3$, (f) $SrZrO_3$, (g) GZO, (h) GYZO, (i) 4YSZ, (j) 5Yb-SZ.

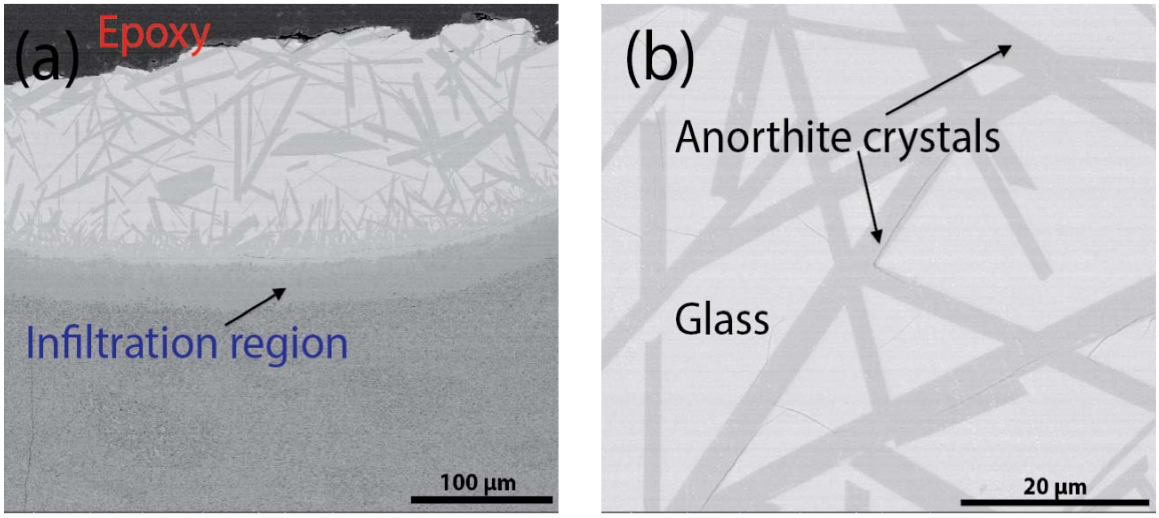

Figure 23: (a) A BSE image from the cross-section at which CMAS reaction and infiltration of mullite took place; (b) A secondary electron (SE) image acquired from the same region, showing the anorthite crystallite morphology.

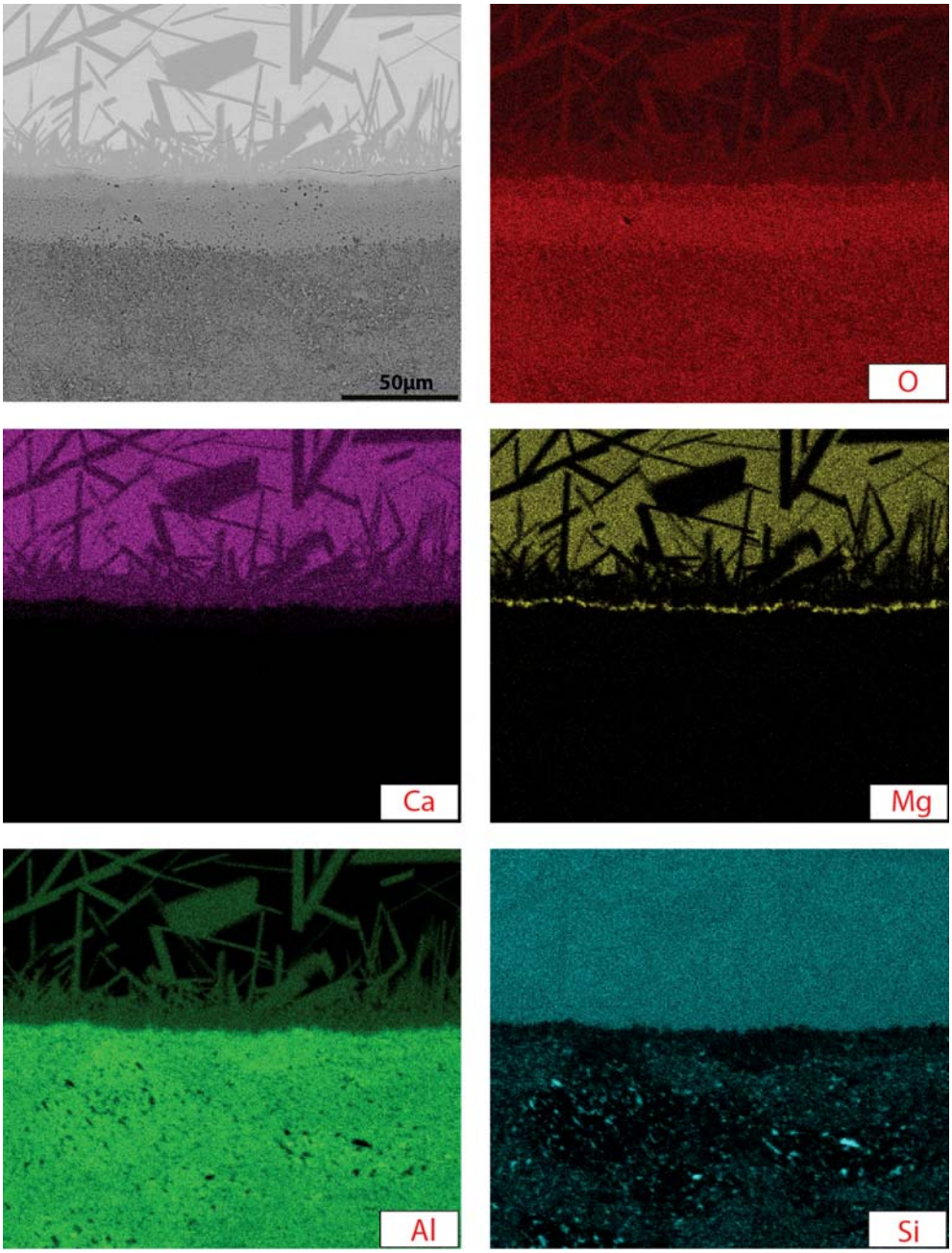

Figure 24: EDS maps of the Mullite/CMAS interface, showing the general distribution of chemistry in the resulting phase mixtures.

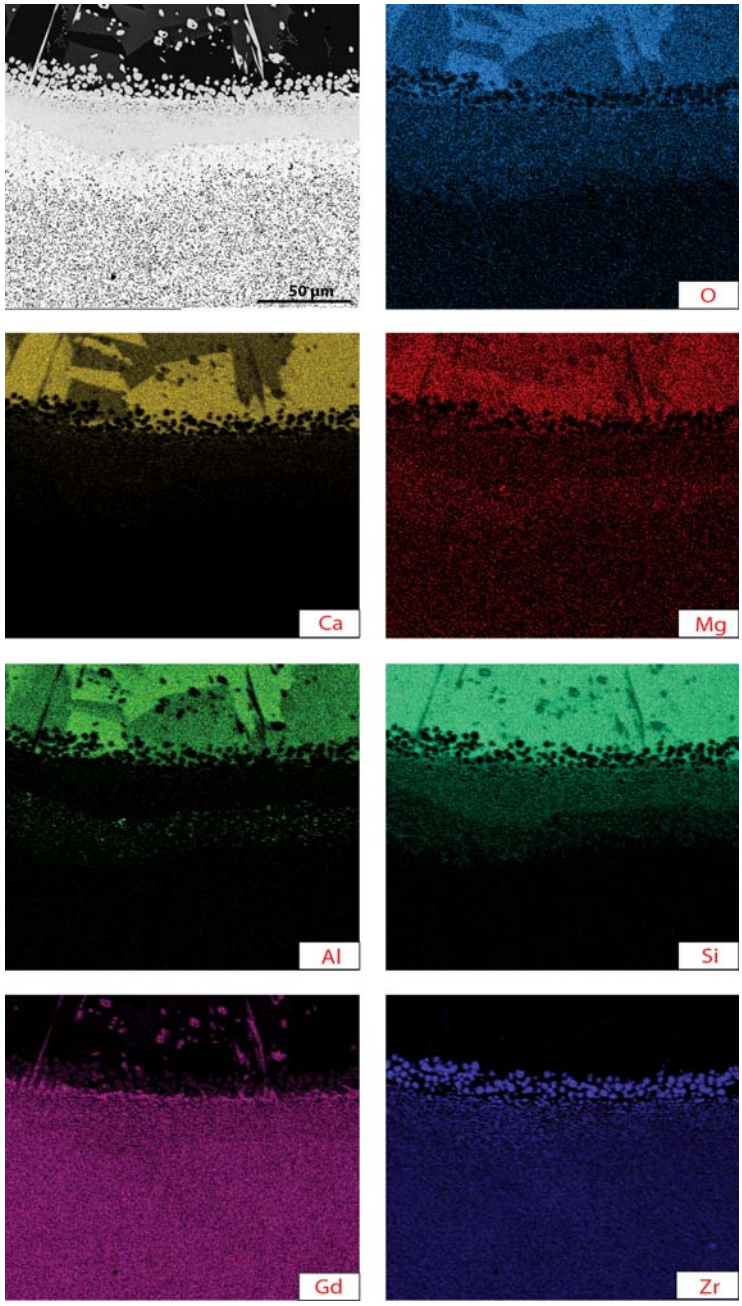

Figure 25: EDS mapping results from the cross-sectioned $Gd_2Zr_2O_7$ sample acquired from the infiltration region.

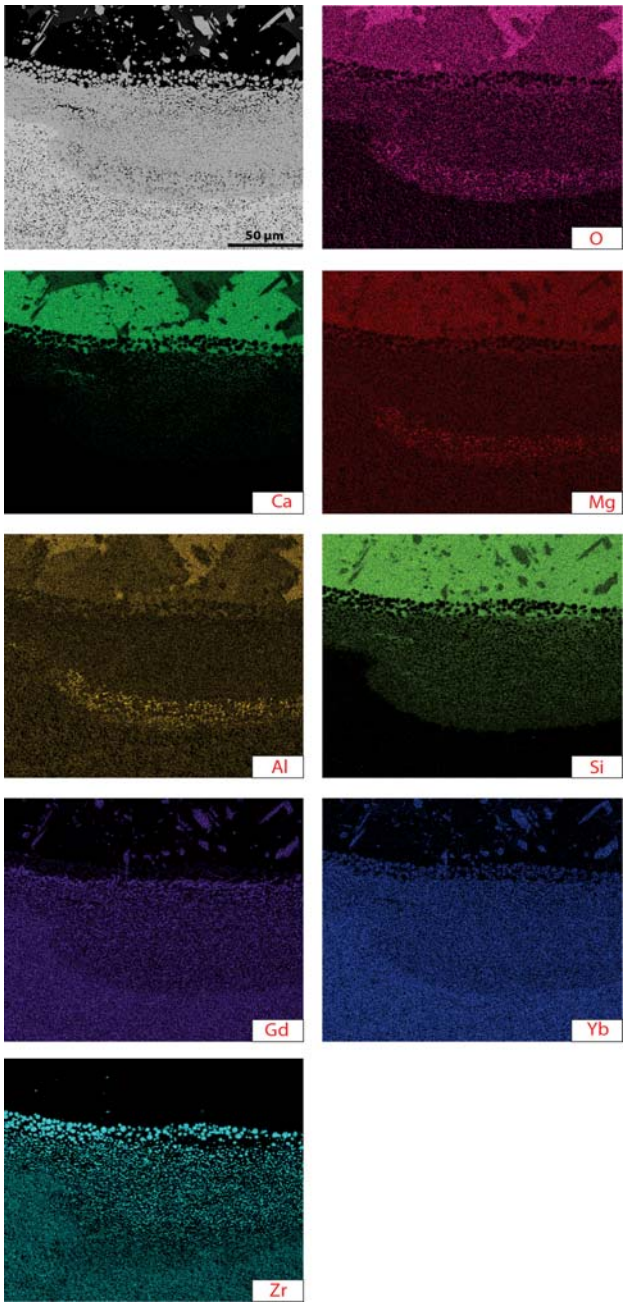

Figure 26: EDS mapping results from the cross-sectioned $GdYbZr_2O_7$ sample acquired from the infiltration region. A much more extensive thermo-chemical interaction is observed with the $GdYbZr_2O_7$ in relation to the $Gd_2Zr_2O_7$ materials.

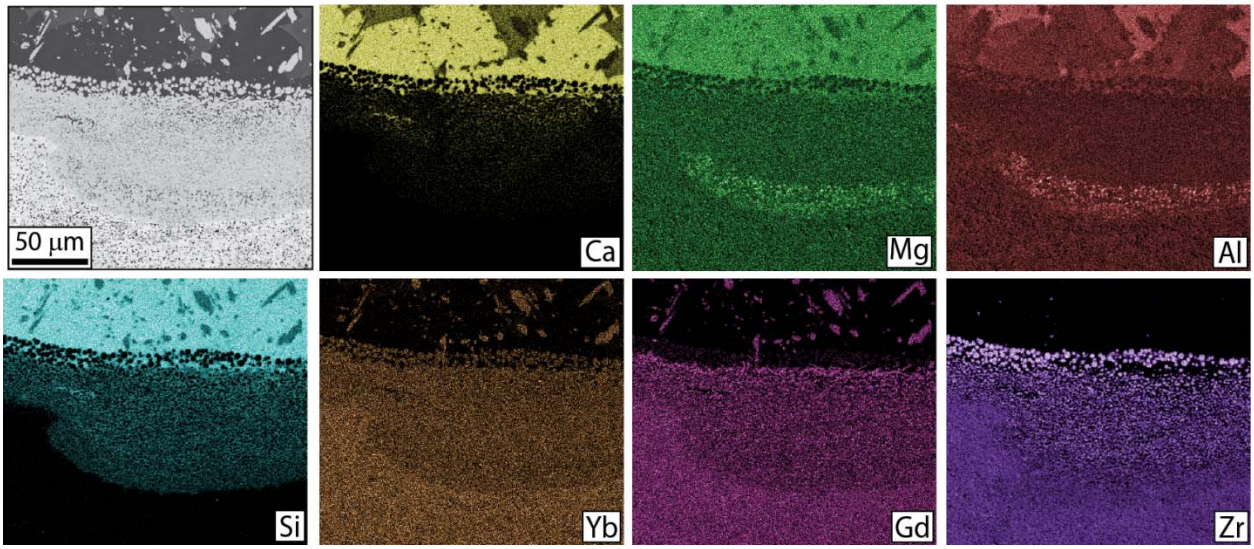

Figure 27: BSE image and elemental maps of the dissolution front of CMAS into GYZO.

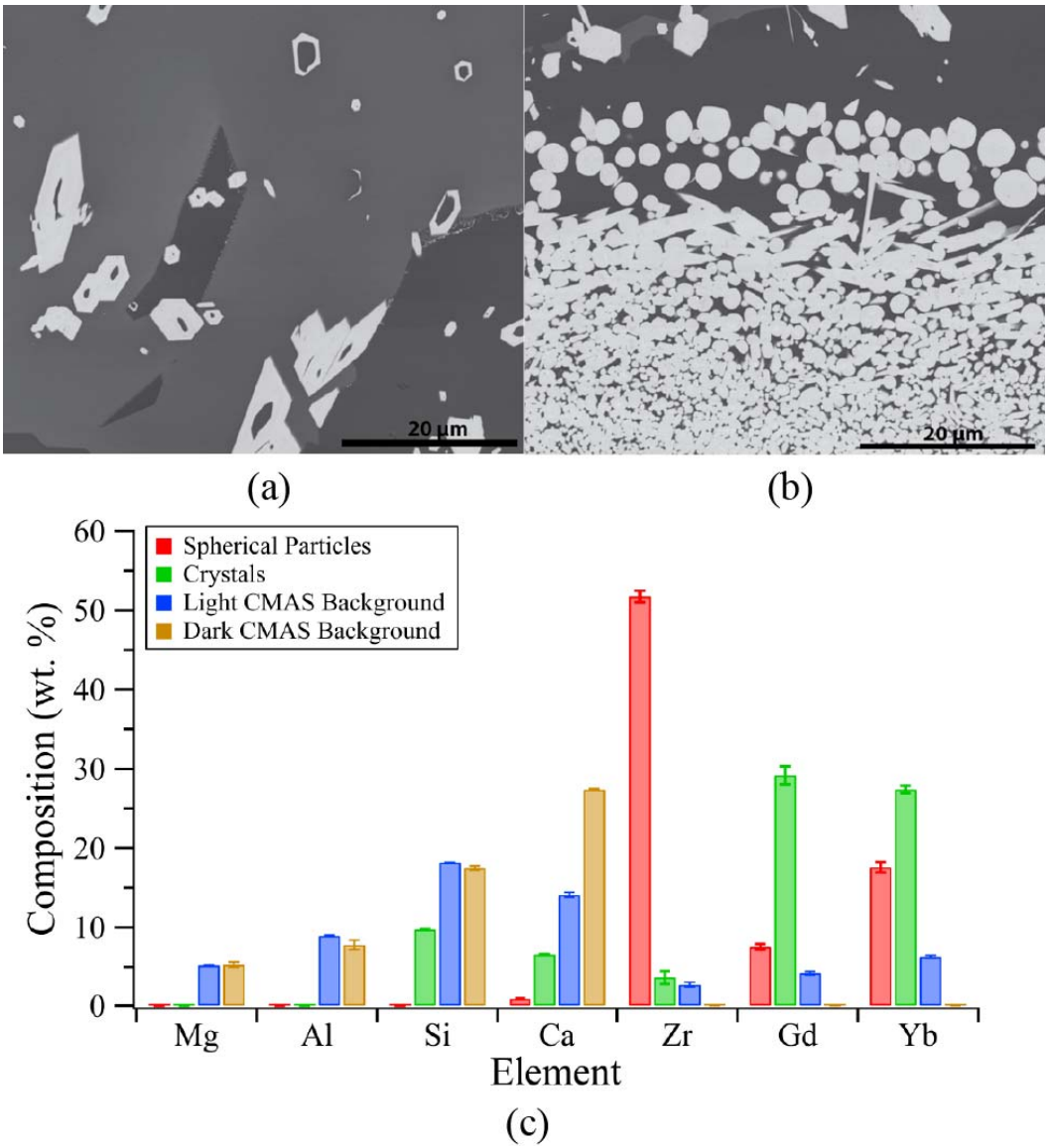

Figure 28: Close-up of CMAS-GYZO reaction products showing: (a) and (b) BSE images and (c) EDS results of various regions within the images.

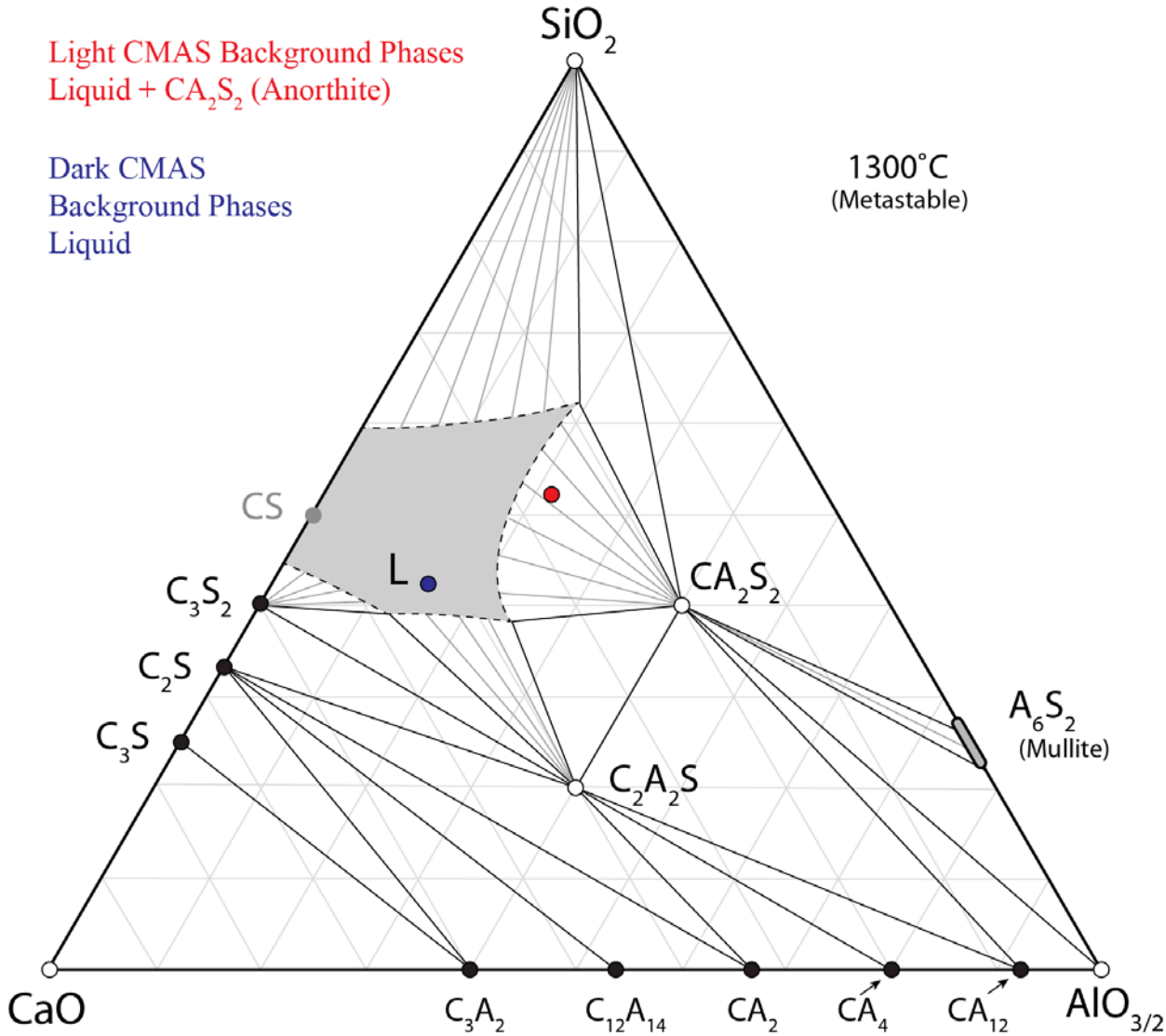

Figure 29: Isothermal ternary phase diagram at 1300°C of SiO_2-CaO-Al_2O_3. Single-cation oxide formula units are used here so that A = $AlO_{3/2}$, C = CaO, and S = SiO_2.

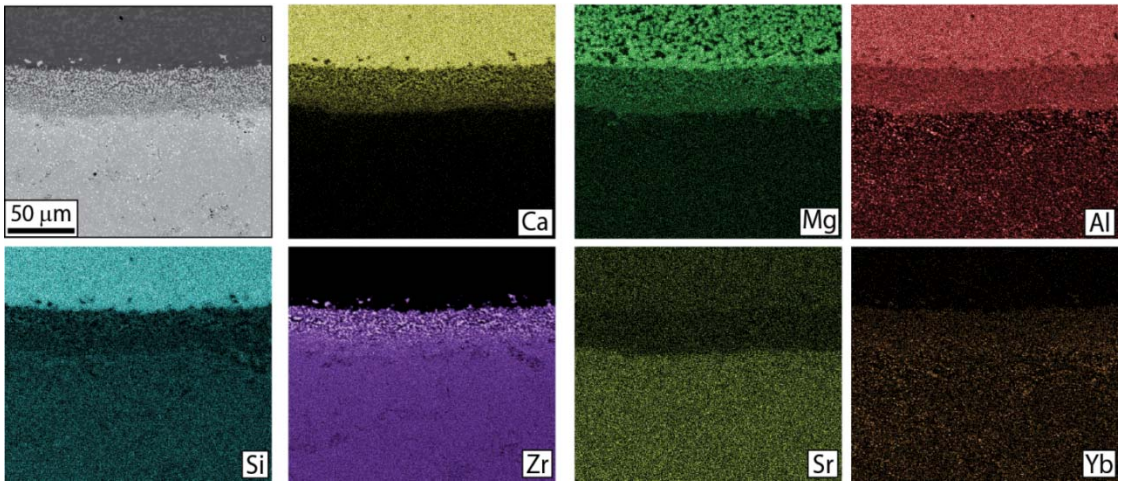

Figure 30: BSE image and elemental maps of the dissolution front of CMAS into YSZO.

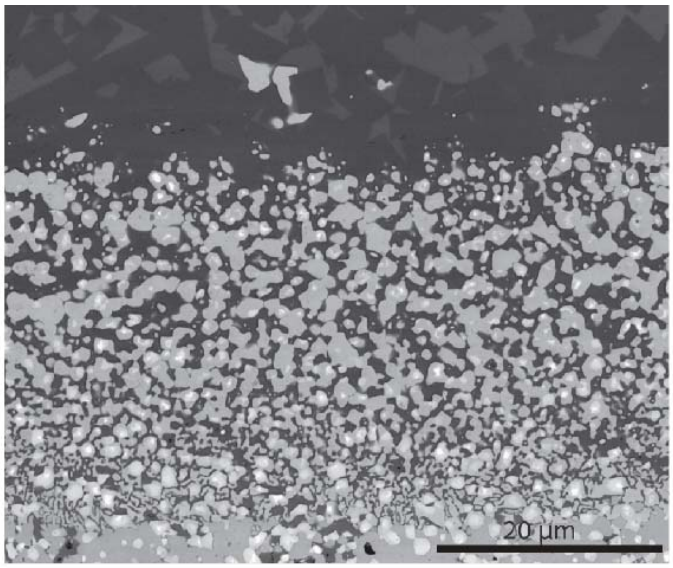

(a)

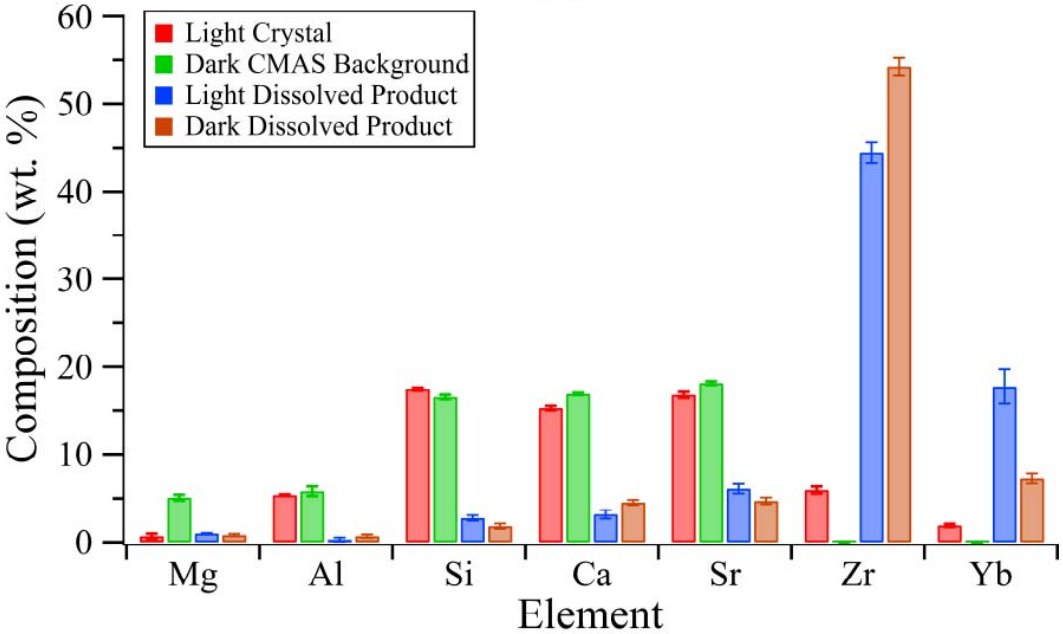

(b)

Figure 31: Close-up of CMAS-YSZO reaction products showing: (a) BSE image and (b) EDS results of various regions within the image.

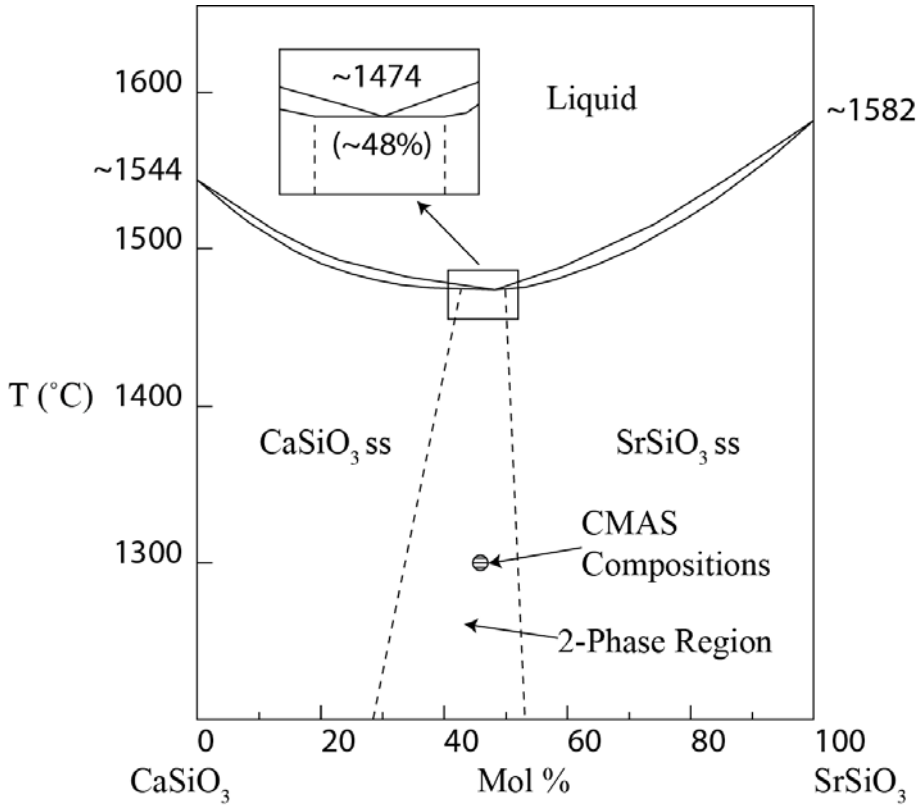

Figure 32: Binary phase diagram of $CaSiO_3$-$SrSiO_3$. The estimated CMAS compositions—*Dark CMAS Background* and *Light Crystal*—are superimposed on the graph. The CMAS compositions are grouped together as one point because the minor constituents for both compositions are ignored.

Figure 33: A plate of free-standing 8YSZ TBC top coat material, formed by air plasma spraying (APS).

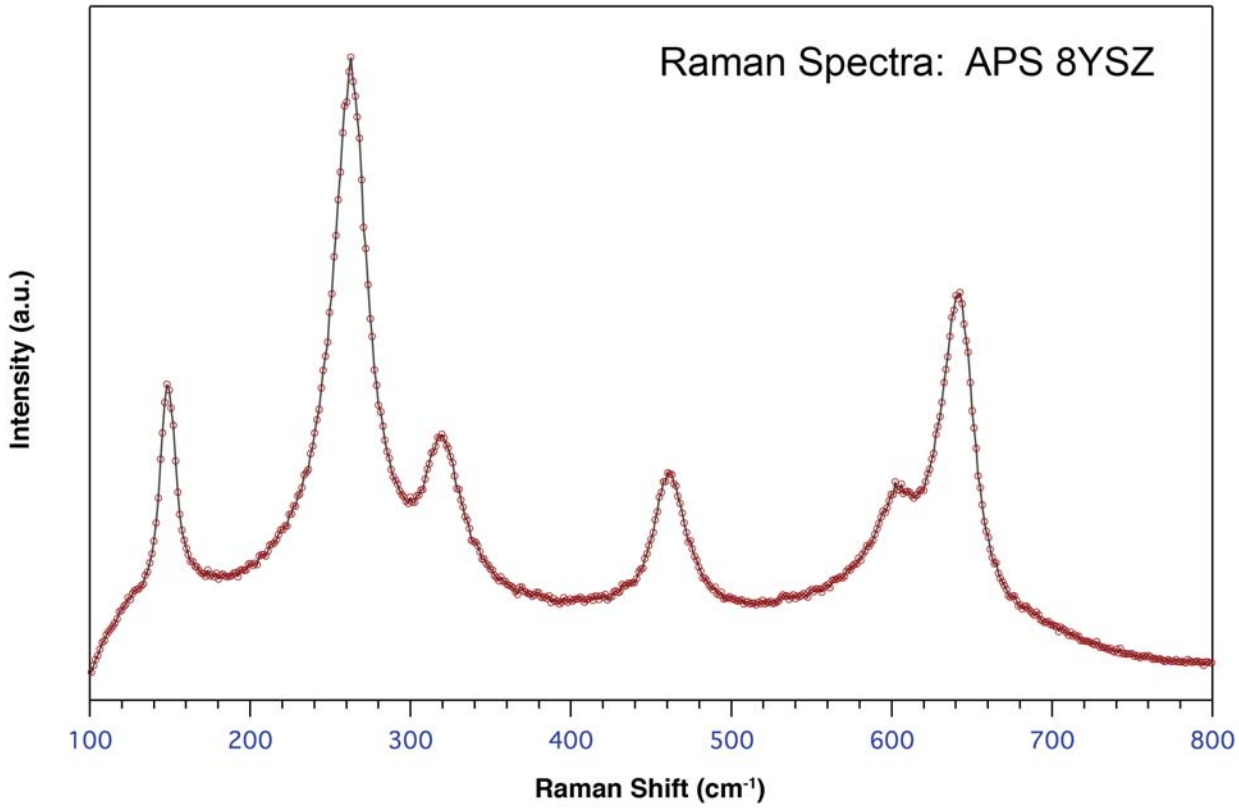

Figure 34: A Raman spectra obtained for APS-processed YSZ material, showing characteristic peaks for the initial t' (metastable tetragonal phase) of YSZ. This data set then acts as the baseline from which material evolution with extended exposures is monitored, relative to changes in the features of the spectra.

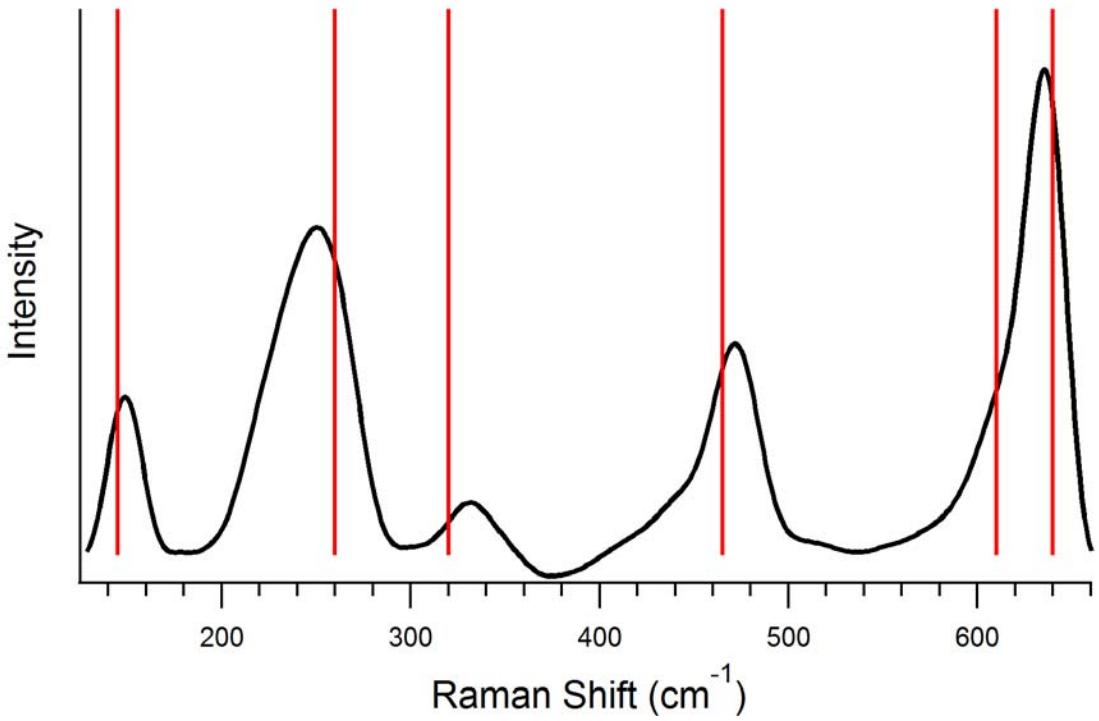

Figure 35: Typical Raman spectra on an 8 YSZ sample heated to 1300°C with no aging. The characteristic 8YSZ tetragonal Raman lines are shown in red.

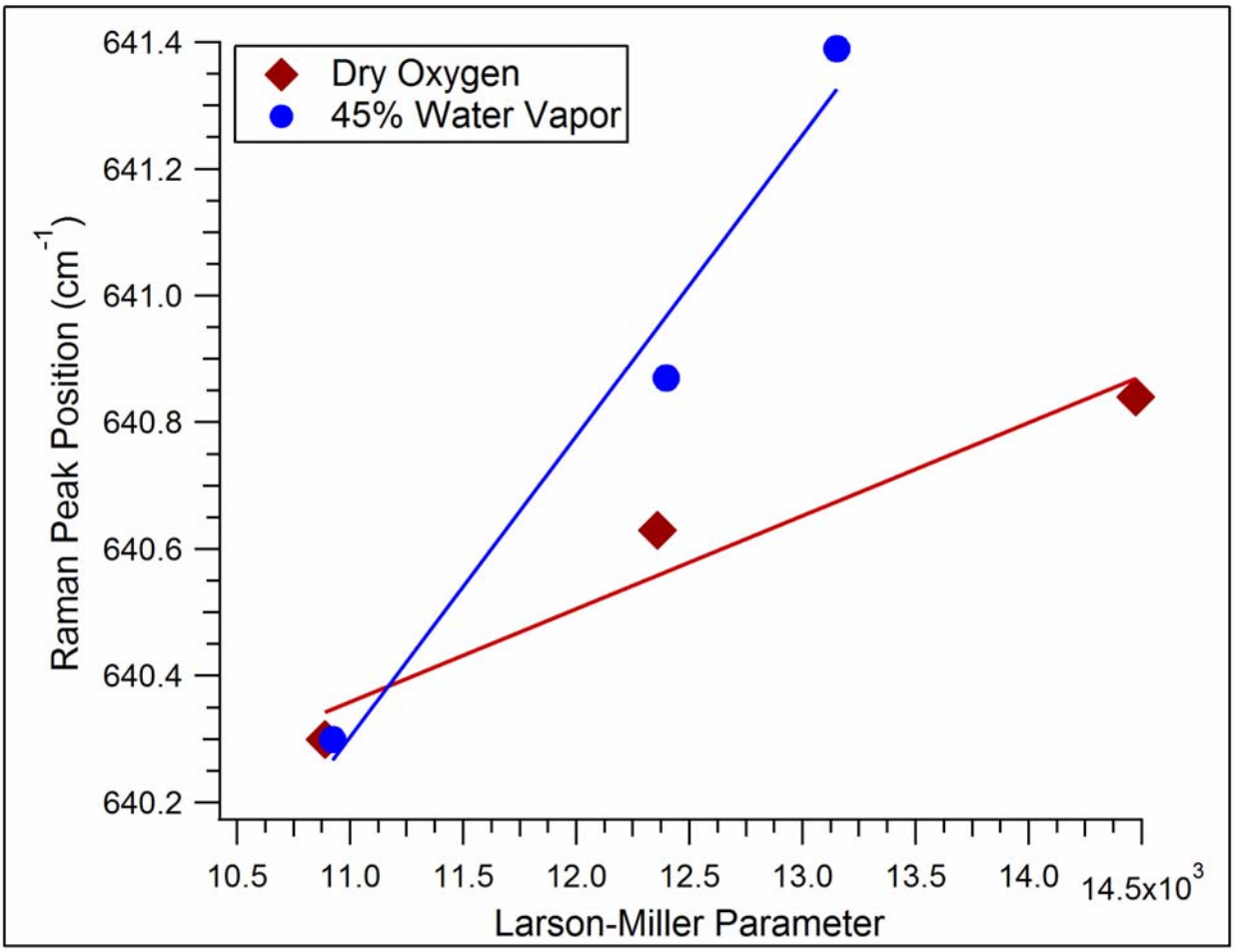

Figure 36: Raman peak position as a function of the Larson-Miller parameter for the 640 cm^{-1} peak of 8YSZ. The points correspond to ageing times of 6, 15, and 75 hrs for the dry oxygen environment and 6, 15, and 24 hrs for the water vapor environment.

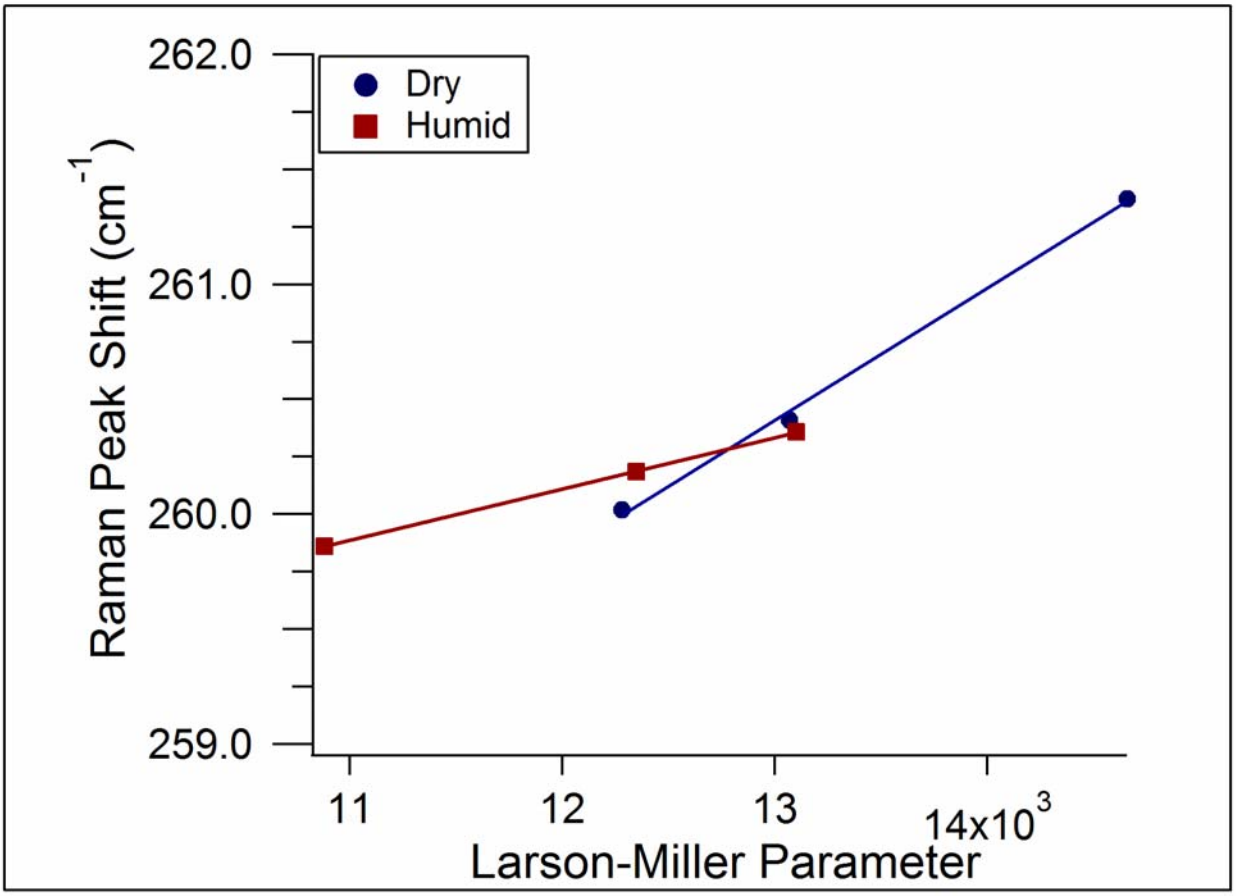

Figure 37: Raman peak position for the 260 cm^{-1} tetragonal peak as a function of the Larson-Miller parameter (LMP) for the dry and humid, oxygen environments.

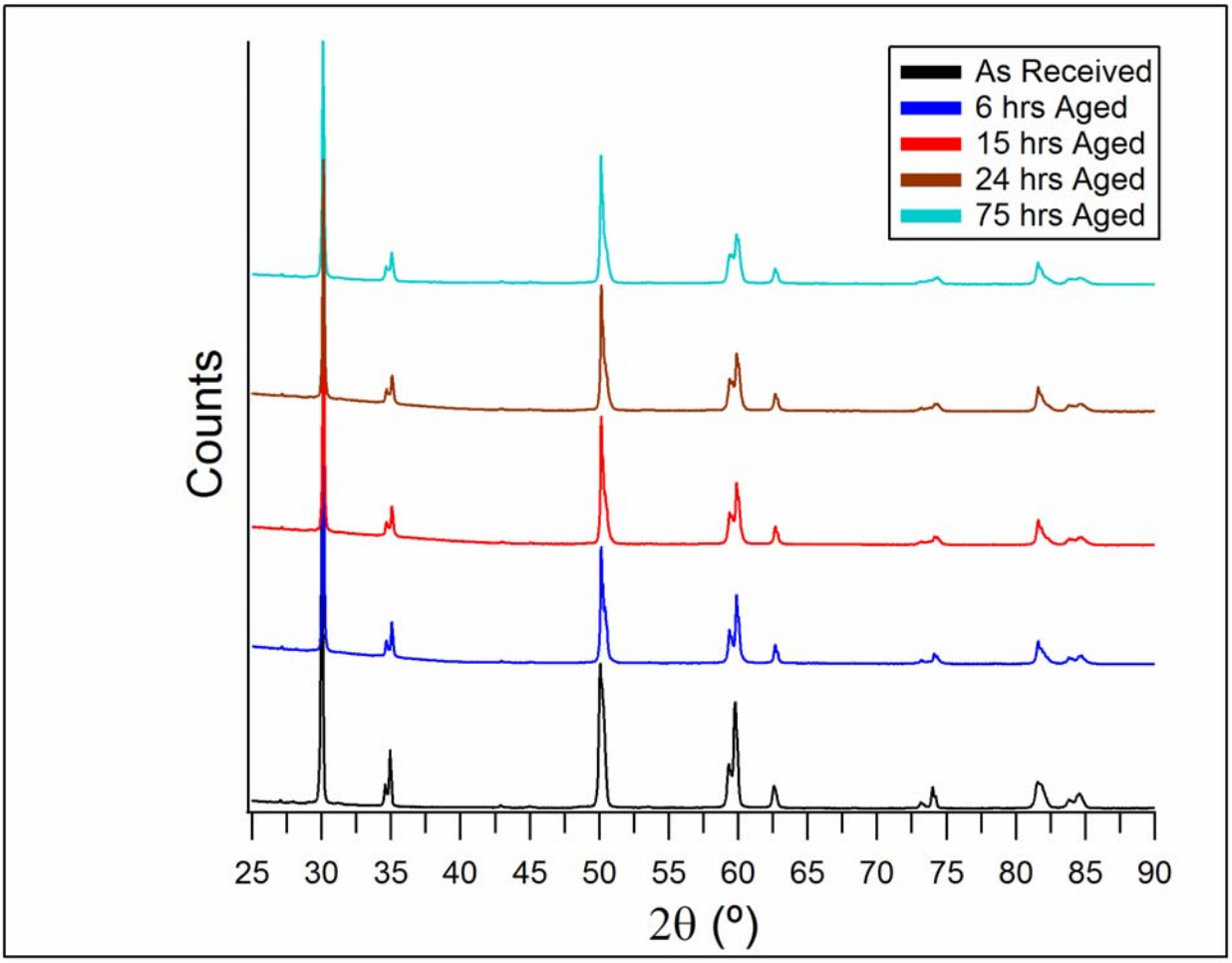

Figure 38: XRD scans for APS 8YSZ for the as received state and various ageing times.

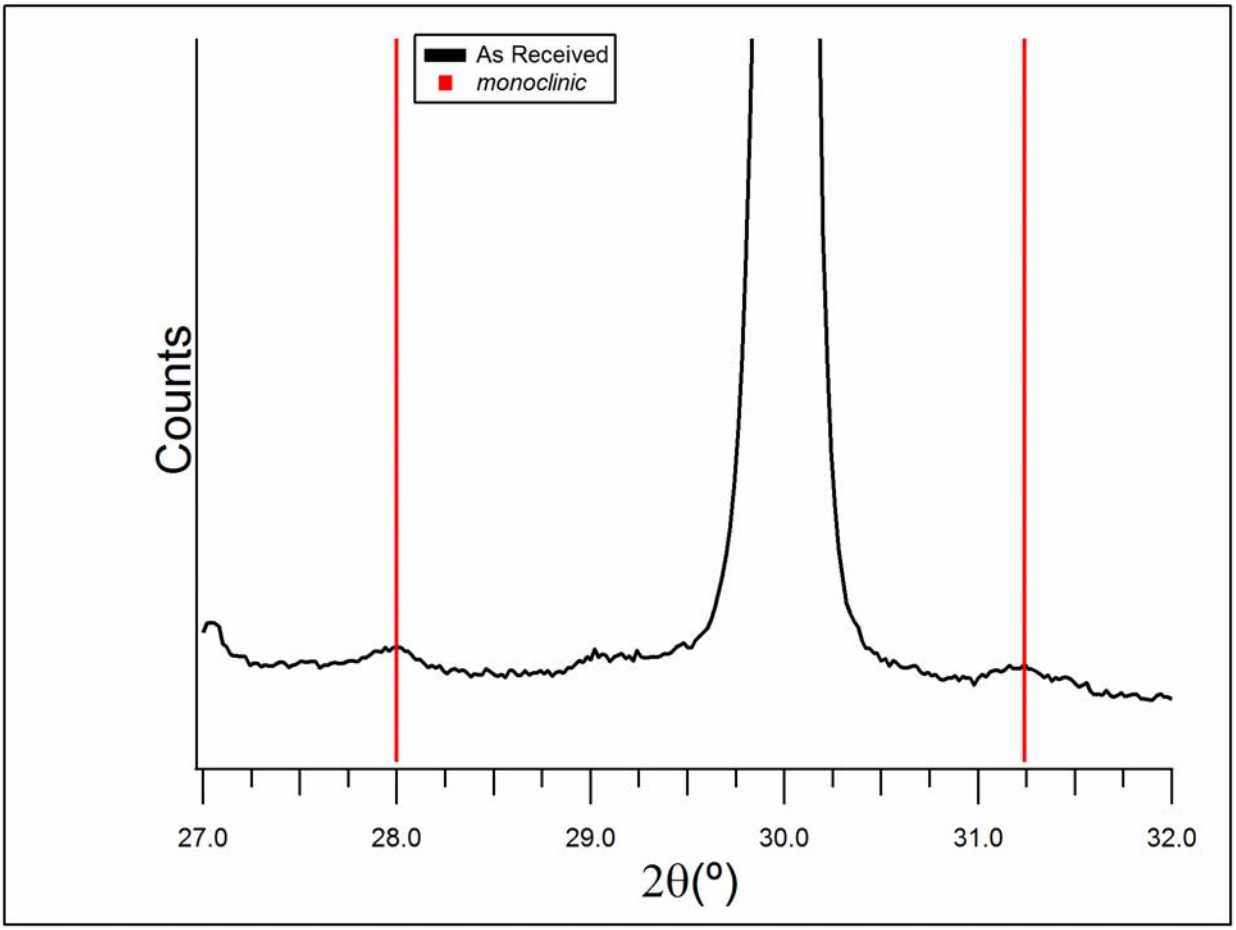

Figure 39: XRD scan for the APS 8YSZ as received state showing the (111) and $(11\bar{1})$ monoclinic peaks.

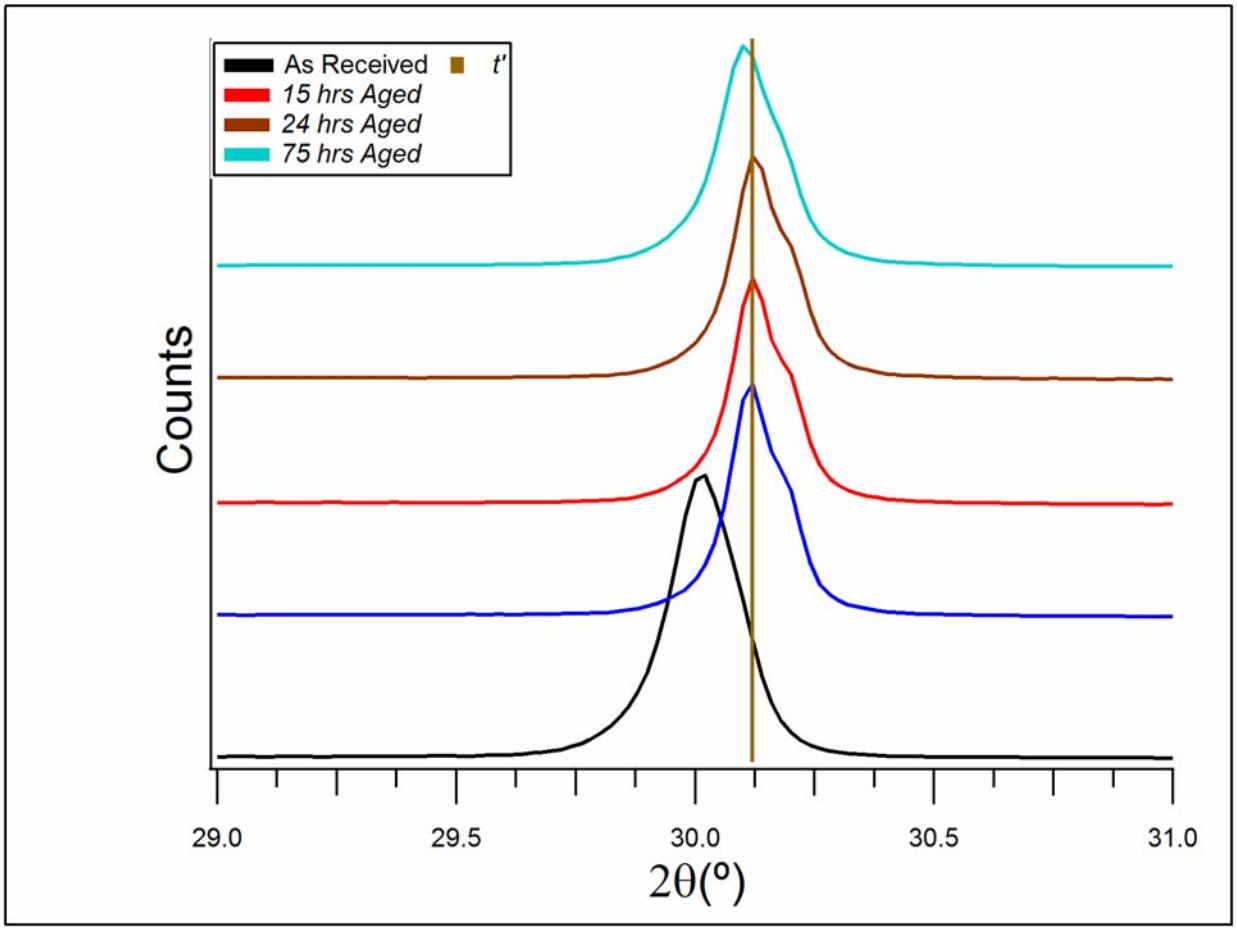

Figure 40: XRD scans for APS 8YSZ for the as received state and various ageing times at the 30.2º peak position.

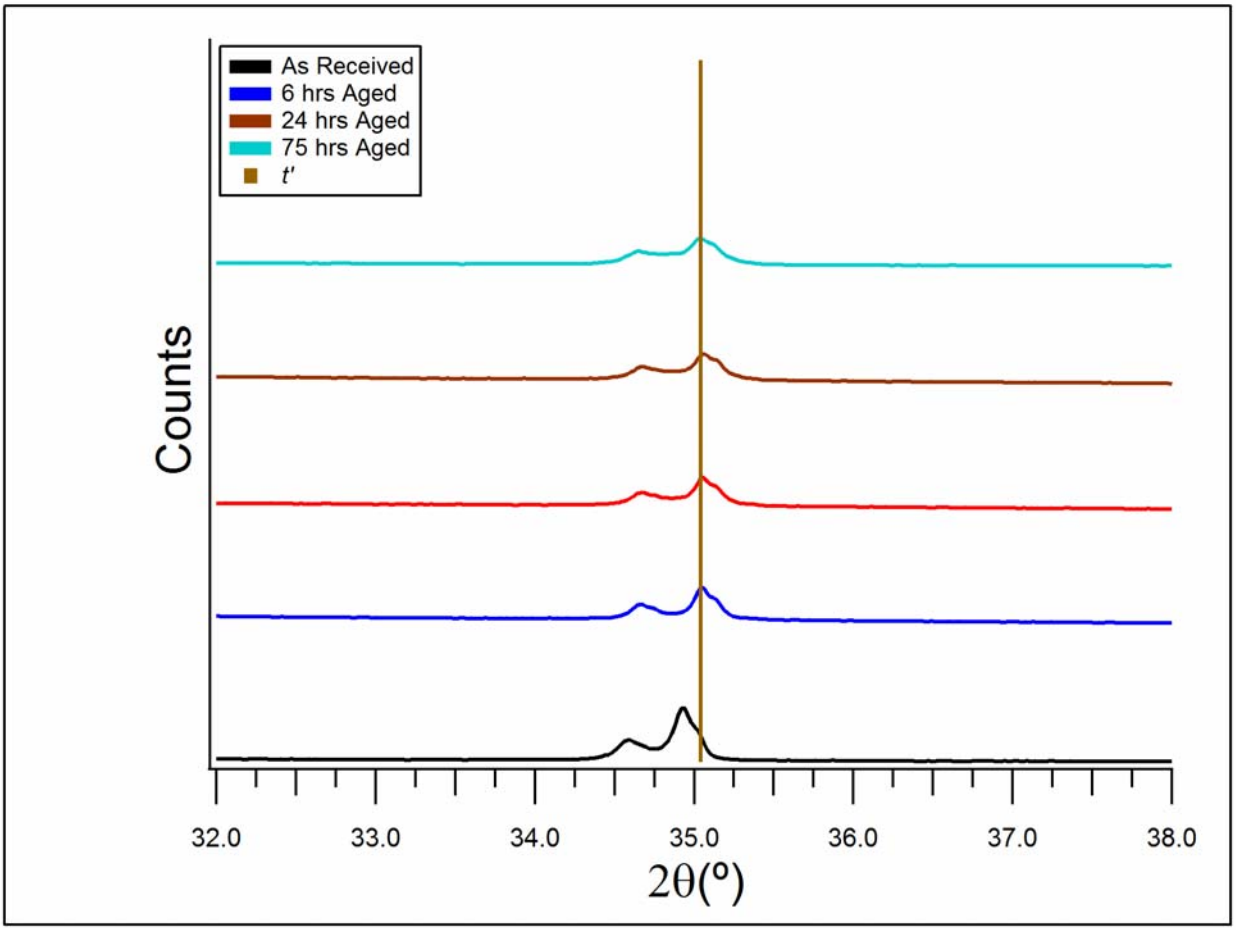

Figure 41: XRD scans for APS 8YSZ for the as received state and various ageing times at the 35.1º peak position.

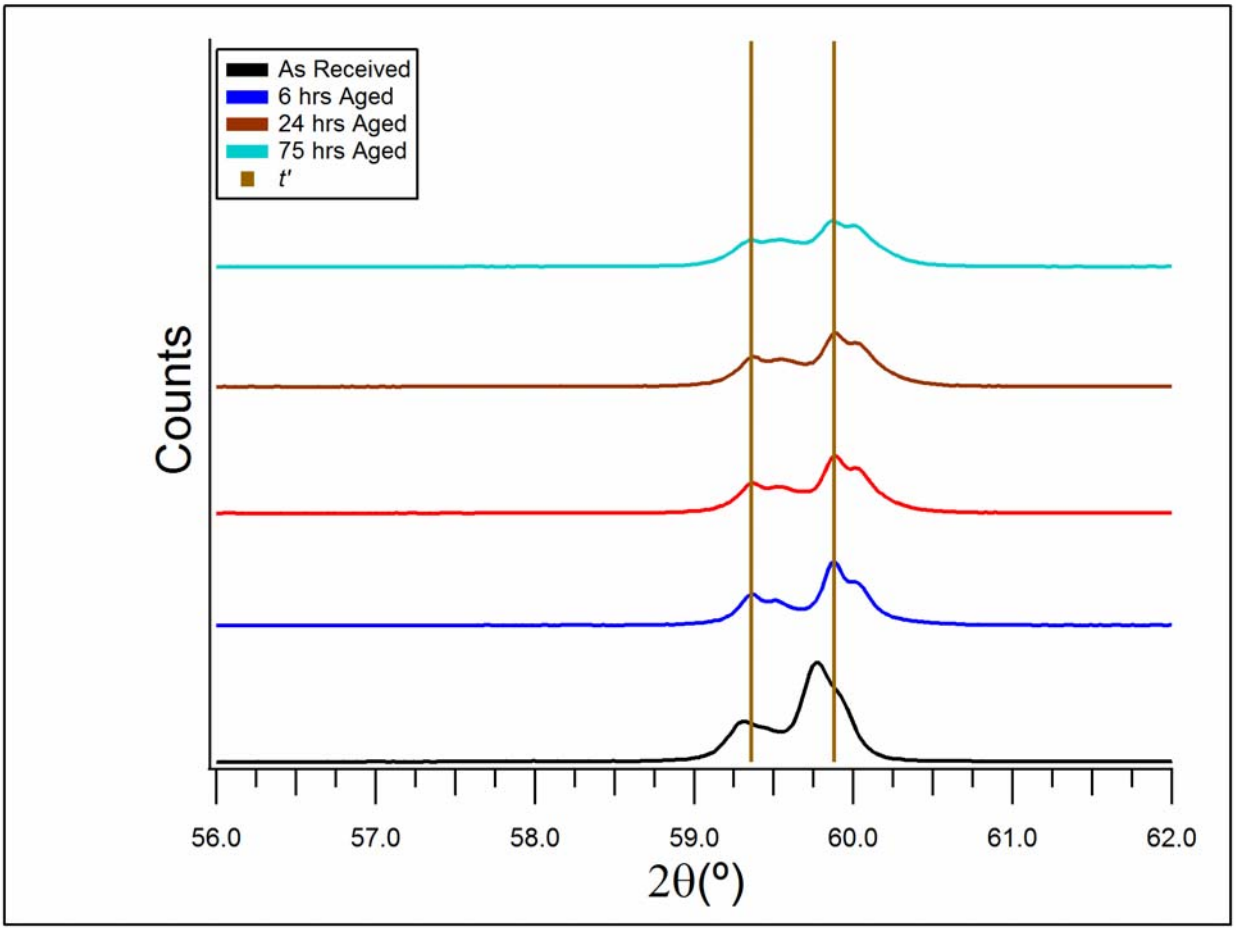

Figure 42: XRD scans for APS 8YSZ for the as received state and various ageing times between the 59-60° peak position.

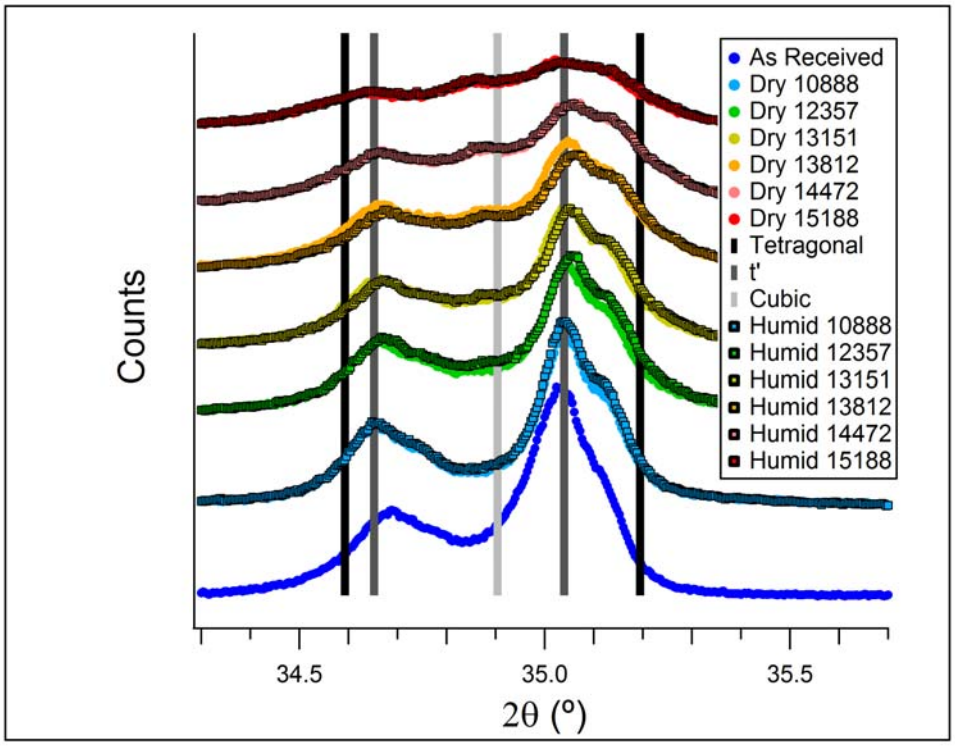

Figure 43: XRD peaks of aged, APS 8YSZ with increasing Larson Miller Parameter for the (002) and (110) tetragonal planes and the (002) cubic plane. The theoretical angular positions and relative intensities are superimposed for the tetragonal, t', and cubic phases.

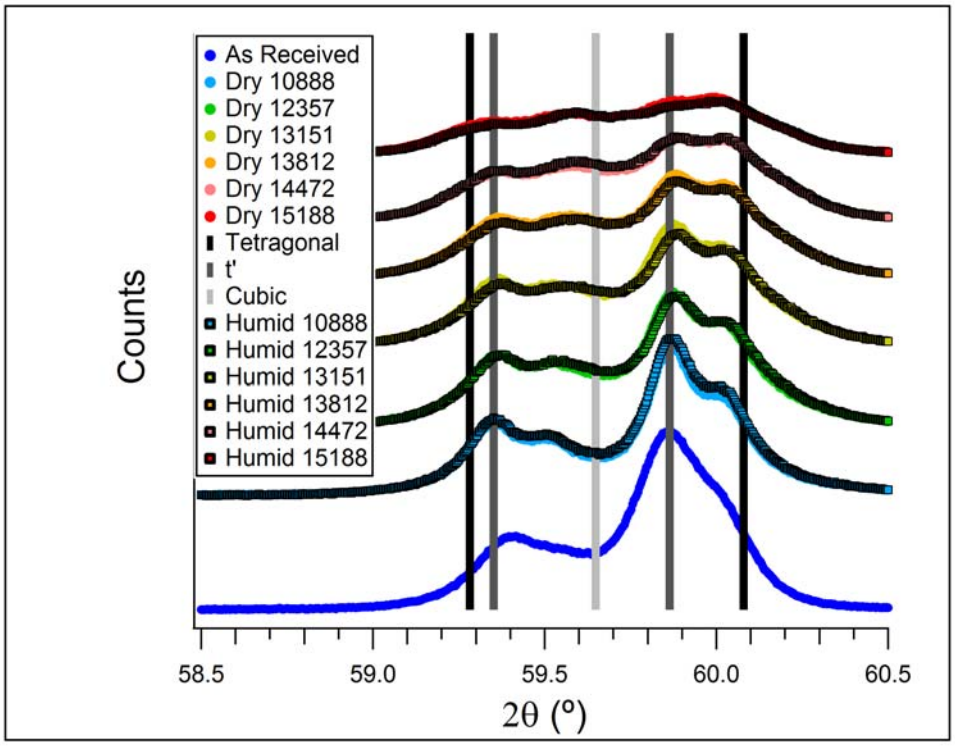

Figure 44: XRD peaks of aged, APS 8YSZ with increasing Larson Miller Parameter for the (013) and (121) tetragonal planes and the (113) cubic plane. The theoretical angular positions and relative intensities are superimposed for the tetragonal, t', and cubic phases.

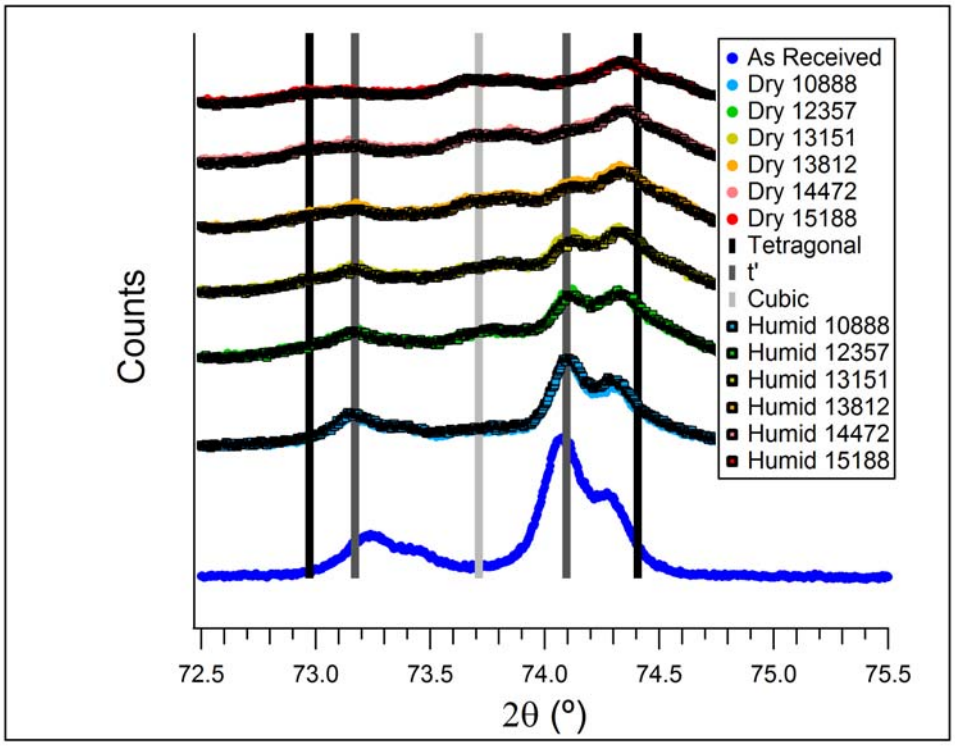

Figure 45: XRD peaks of aged 8YSZ with increasing Larson Miller Parameter for the (004) and (220) tetragonal planes and the (004) cubic plane. The theoretical angular positions and relative intensities are superimposed for the tetragonal, t', and cubic phases.

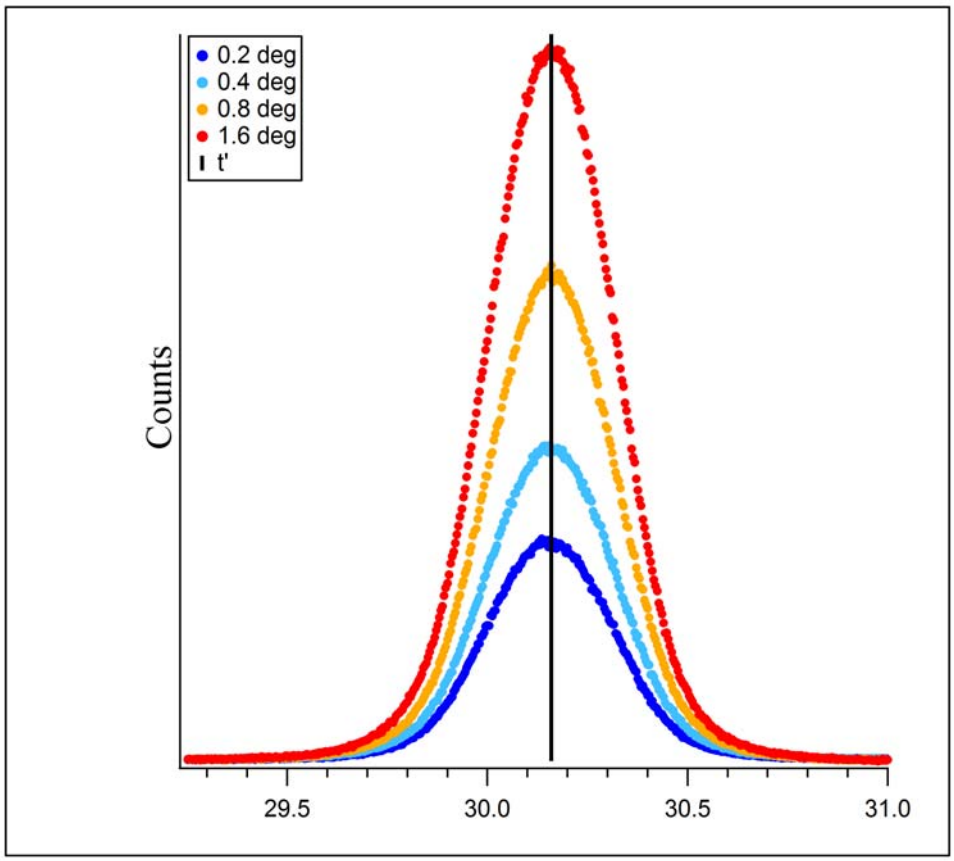

Figure 46: XRD peaks of the 87.7 hrs humid-aged, APS 8YSZ for the (101) tetragonal plane with increasing incident angle.

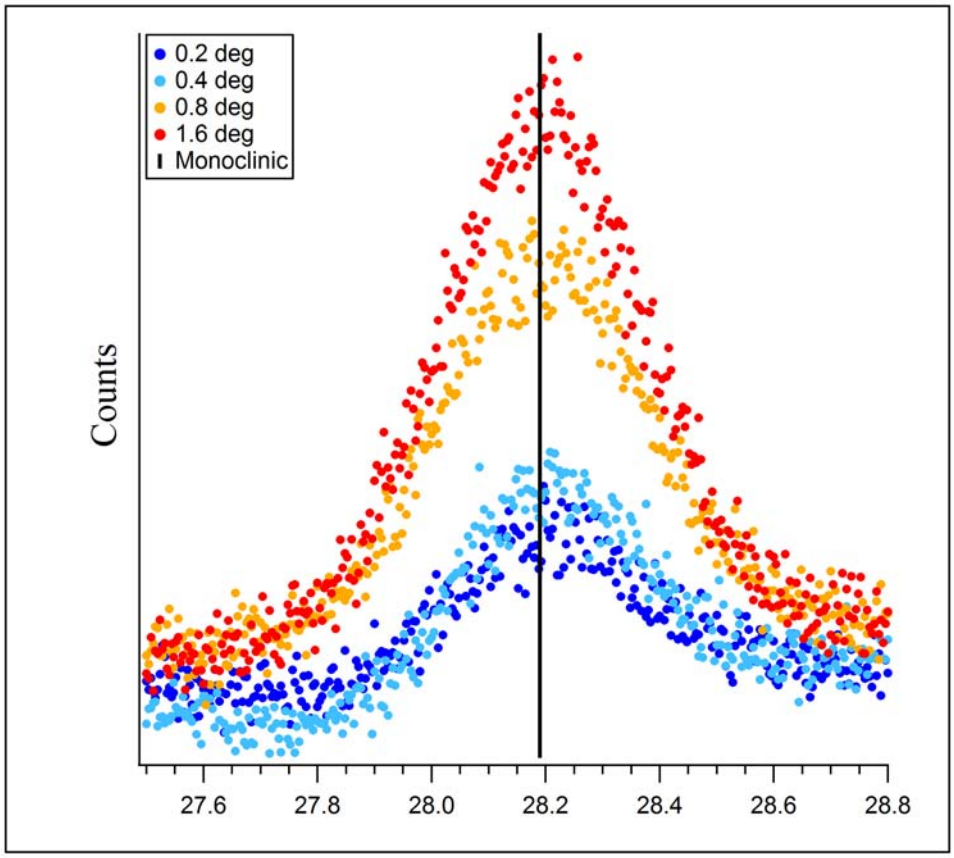

Figure 47: XRD peaks of the 87.7 hrs humid-aged, APS 8YSZ for the $(\bar{1}11)$ monoclinic plane with increasing incident angle.

Figure 48: TBC coatings (as deposited) formed by thermal spray under conditions which give rise to various microstructures: (a) left-most image is that of "standard APS" porous coating; (b) and (c) have increasing levels of segmentation cracking.

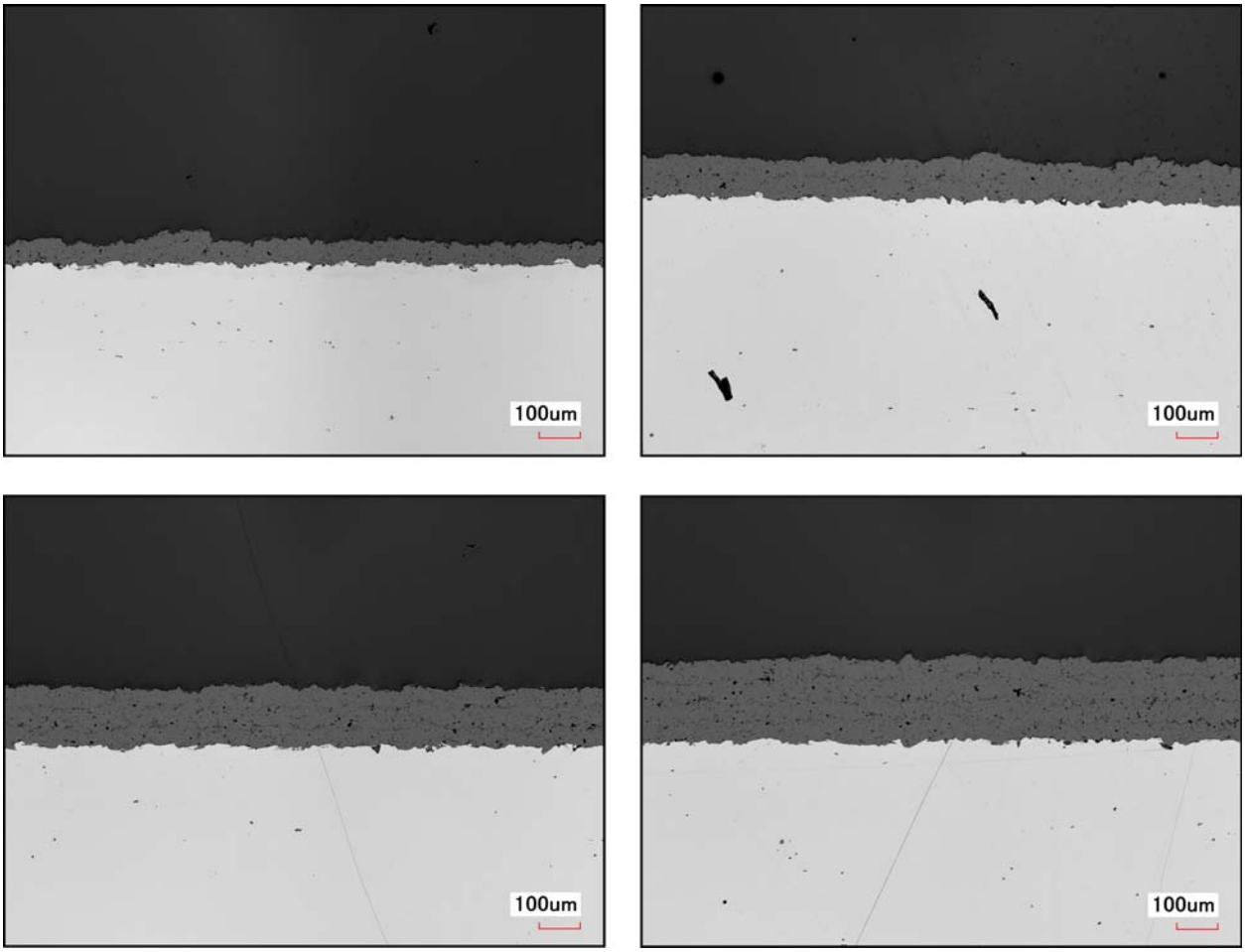

Figure 49: Microstructure development during deposition of 8YSZ TBC coatings with intended segmented coating microstructure. Images show microstructure evolution as a function of spray passes.

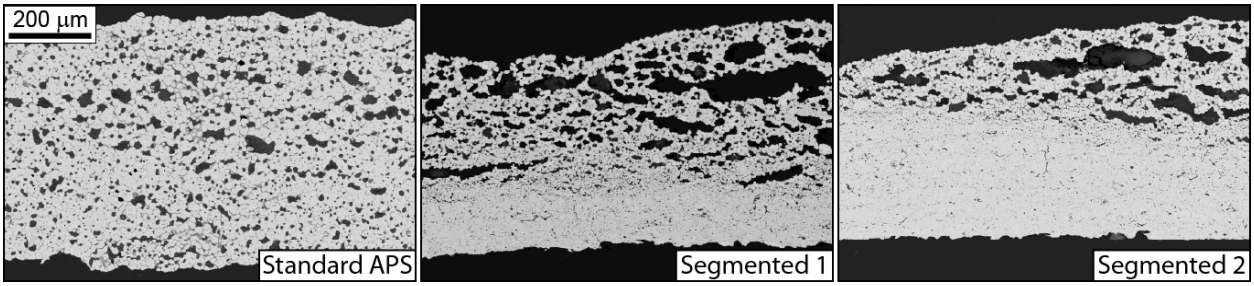

Figure 50: SEM micrographs of the full cross-sectional thickness of a standard APS (left) and two segmented (middle, right) YSZ specimens following infiltration with CMAF. CMAF was applied to specimens from the top.

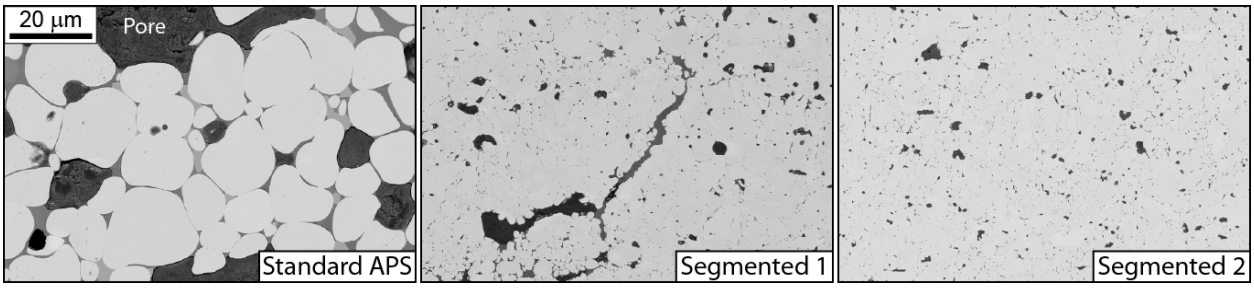

Figure 51: SEM micrographs showing cross-sections from the middle of a standard APS (left) and two segmented (middle, right) YSZ specimens following infiltration with CMAF.

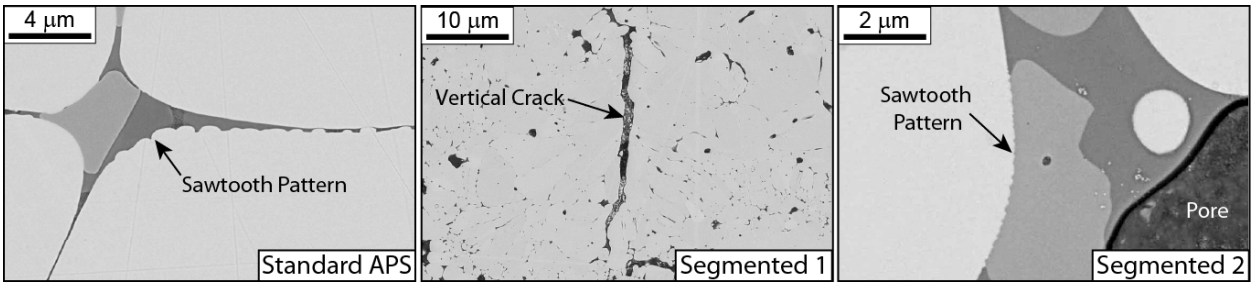

Figure 52: SEM micrographs showing features of note from the middle of a standard APS (left) and two segmented (middle, right) YSZ specimens following infiltration with CMAF.

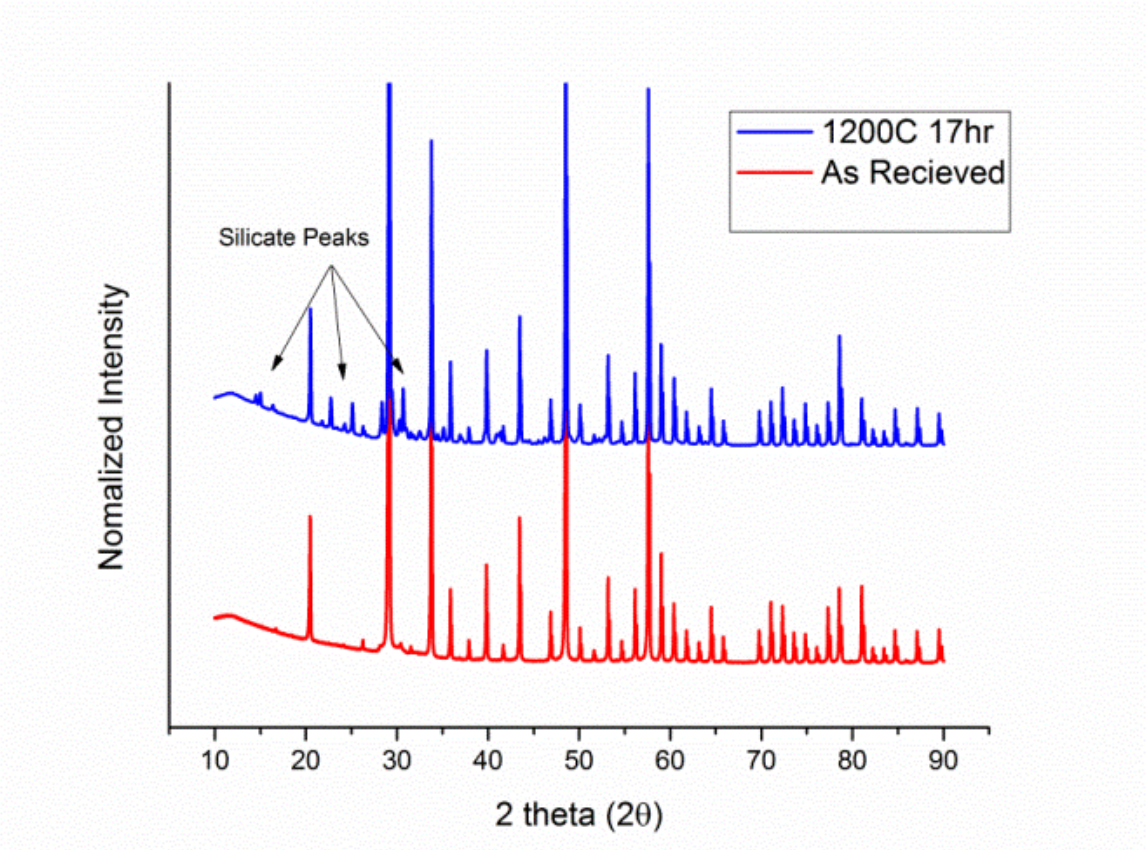

Figure 53: X-ray diffraction highlighting the formation of silicate peaks indicating impurity deposition from the tube furnace walls.

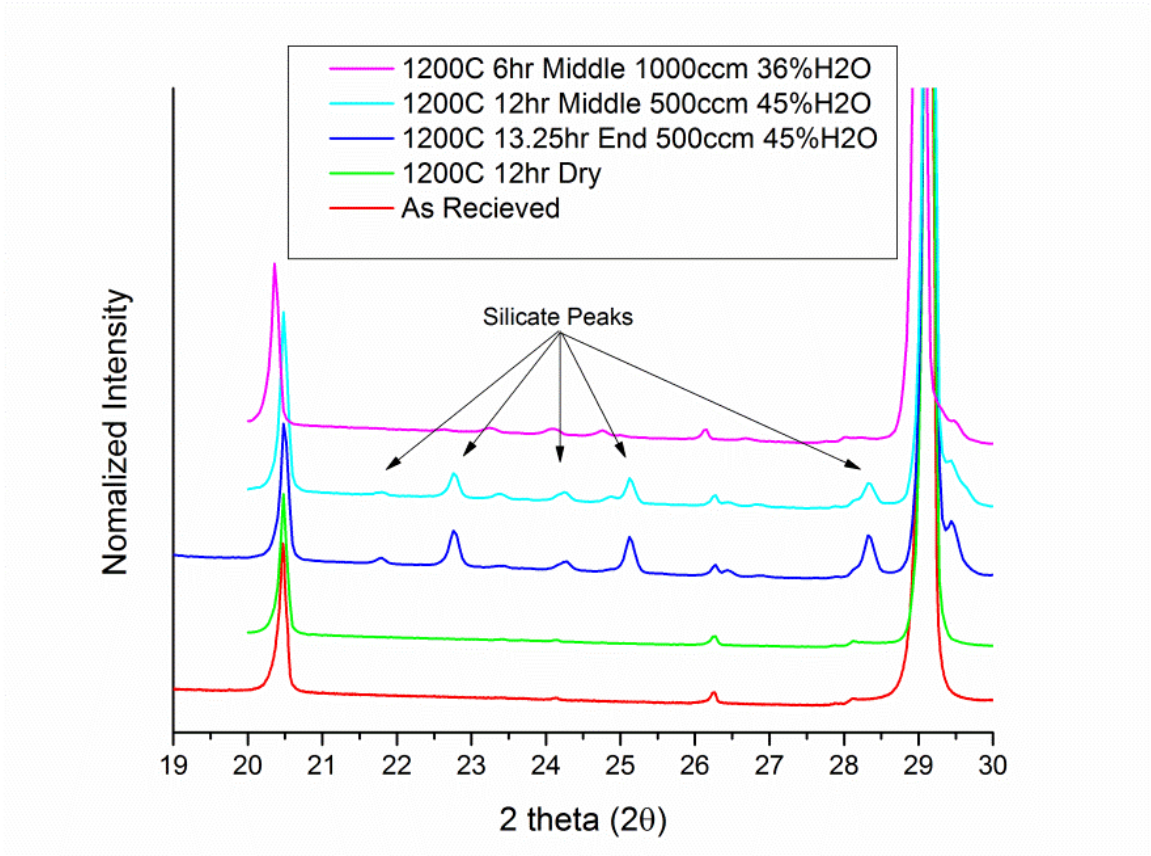

Figure 54: Comparison of Y_2O_3 samples exposed in a quartz tube furnace at 1200°C for 12 hours, with specimens placed at different positions within the zirconia tube. The middle position was 6" from the end.

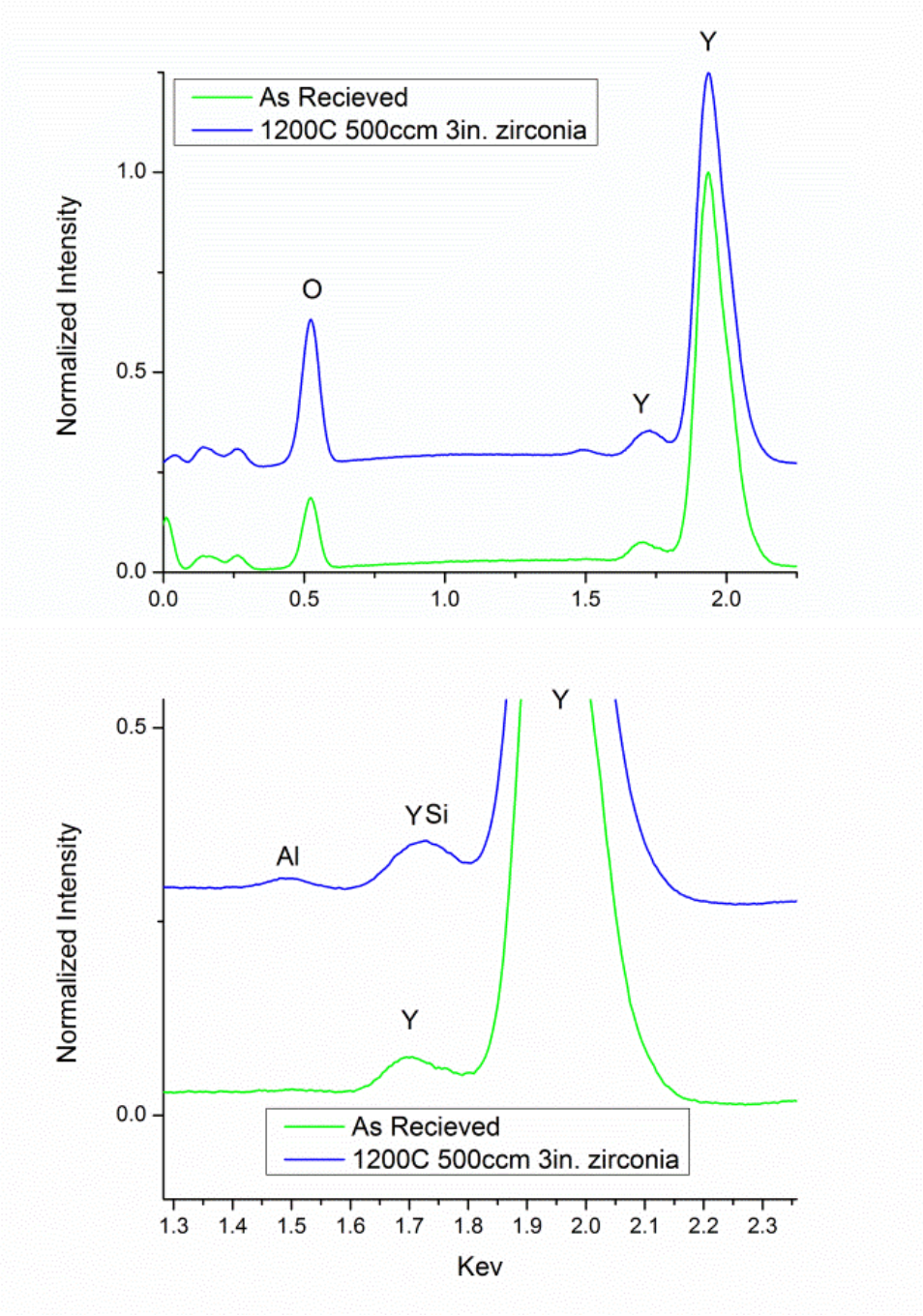

Figure 55: Energy dispersive spectroscopy of an as received sample, and a sample exposed for 12 hours, at 1200°C and 50% water vapor.

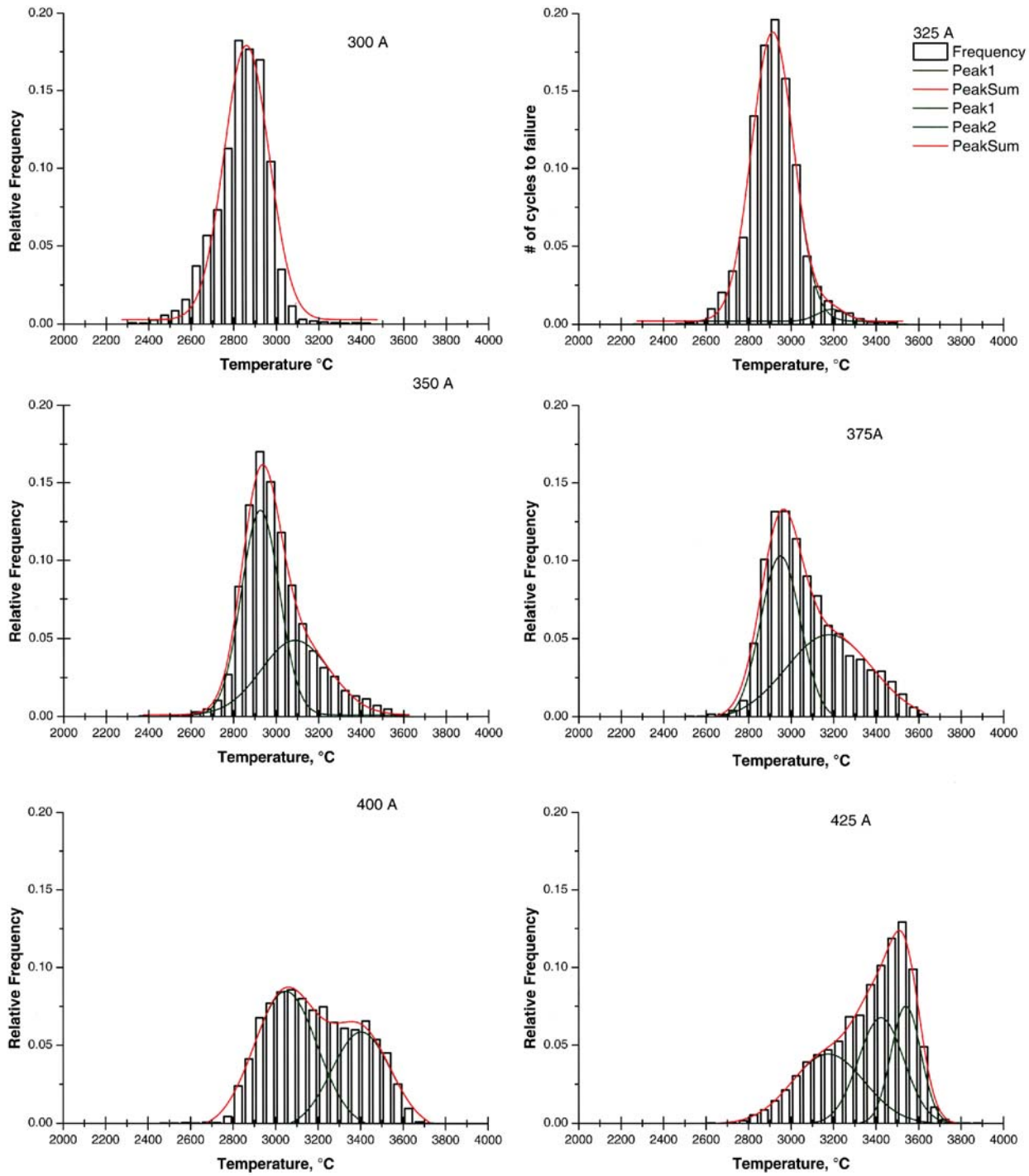

Figure 56: Histograms of particle temperatures during optimization of thermal spray process protocols for Sm-zirconate coatings. The fitting illustrates process conditions at which phase breakdown occurs, and quantifies optimal spray conditions for deposition of phase-pure SZO.

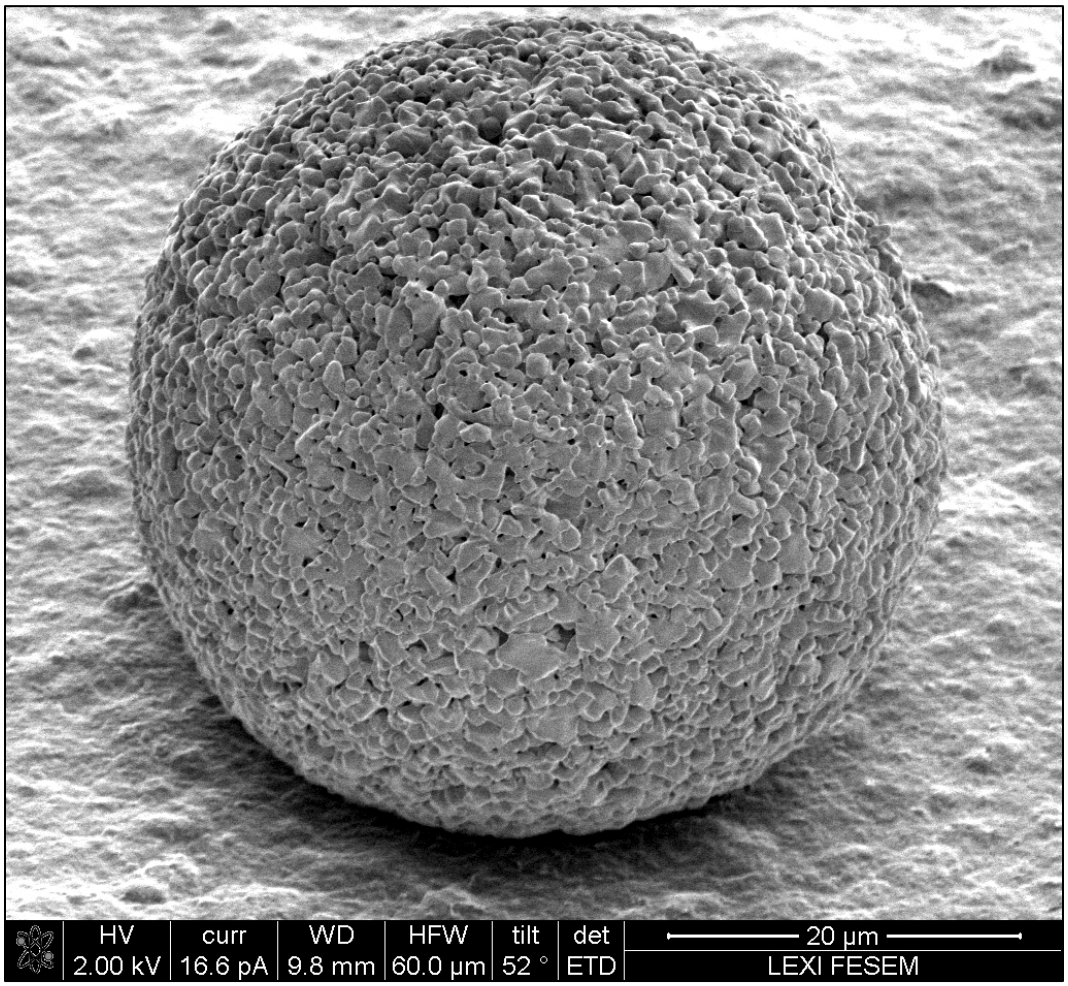

Figure 57: A micrograph of a spherodized granule of $Sm_2Zr_2O_7$, ready for use in thermal spray processing.

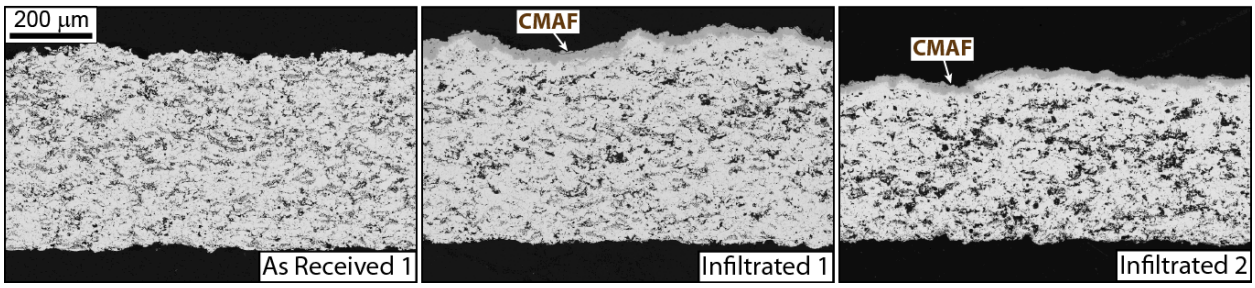

Figure 58: SEM micrographs of the full cross-sectional thickness of an as received (left) and two infiltrated (middle, right) $Sm_2Zr_2O_7$ specimens. CMAF was applied to specimens from the top.

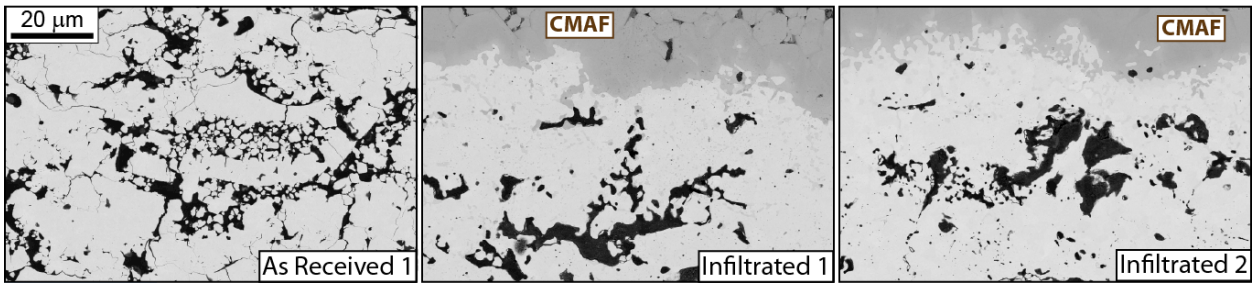

Figure 59: SEM micrographs showing cross-sections from the top portion of as received (left) and infiltrated (middle, right) $Sm_2Zr_2O_7$ specimens.

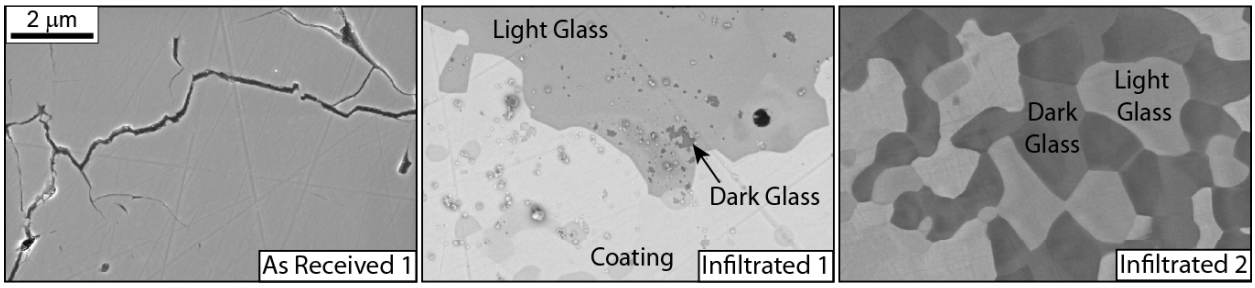

Figure 60: SEM micrographs showing features of note from as received (left) and infiltrated (middle, right) $Sm_2Zr_2O_7$ specimens.

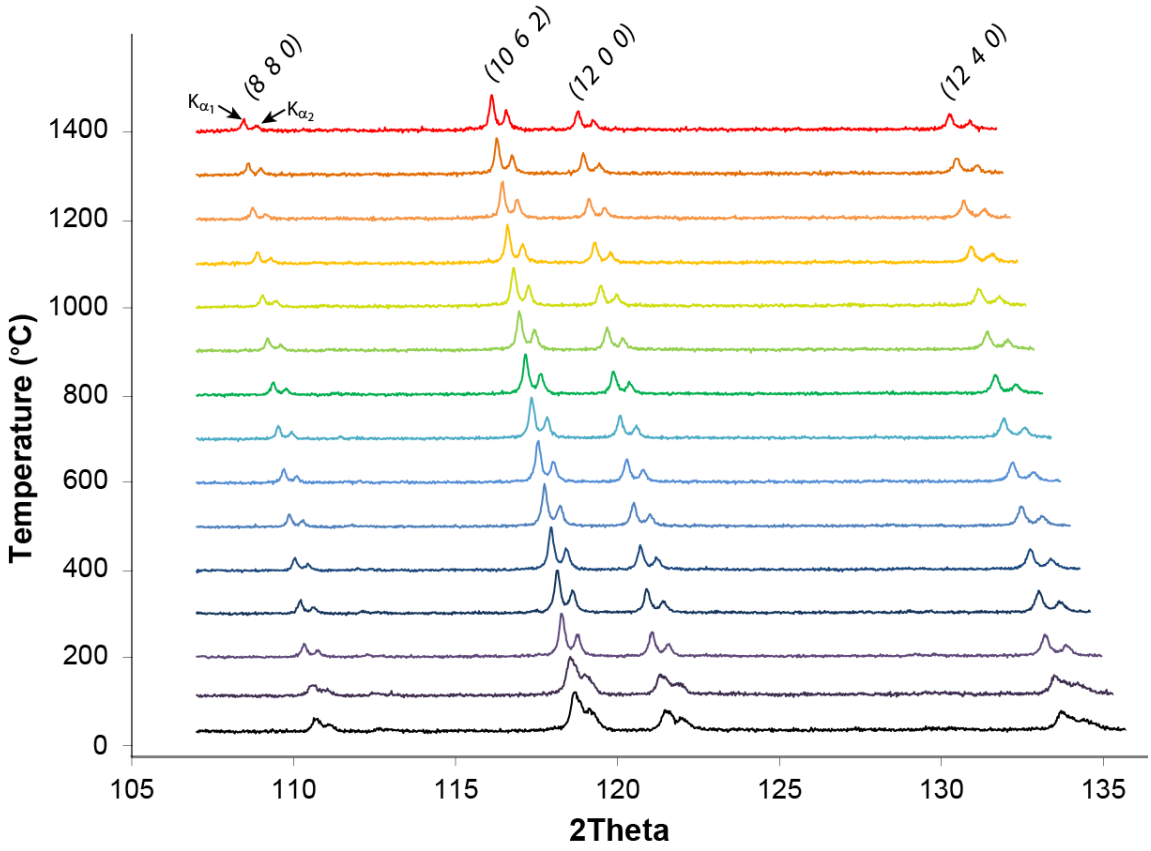

Figure 61: Temperature dependent XRD spectra for $Sm_2Zr_2O_7$, showing peak shifts due to thermal expansion.

(a)

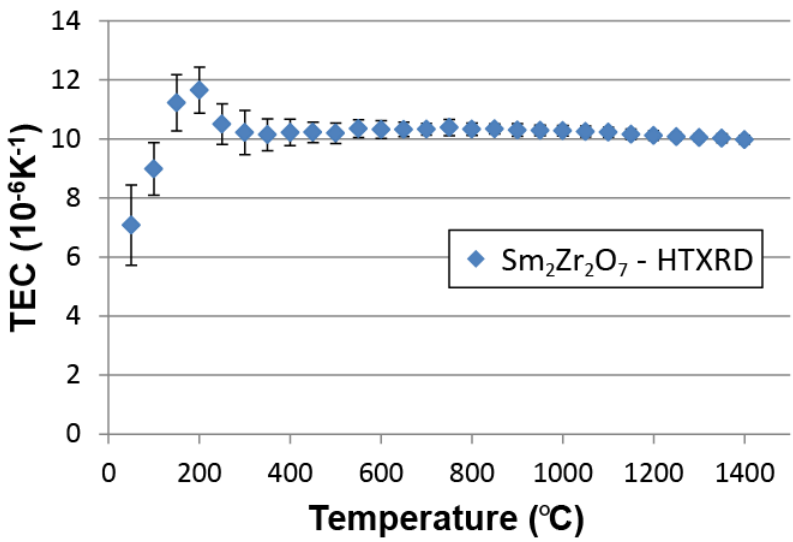

(b)

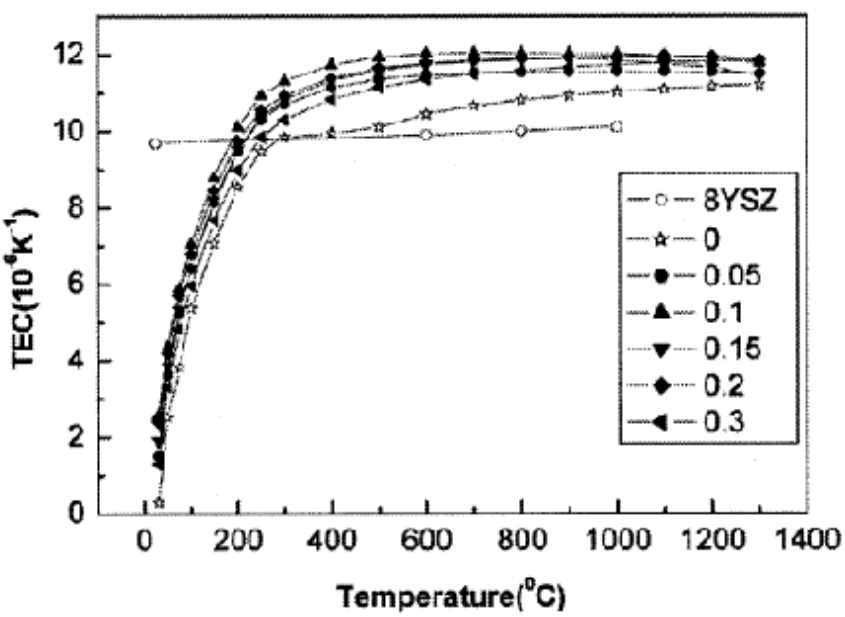

Figure 62: Comparison of TEC data obtained via (a) HTXRD and (b) HT dilatometry [4].

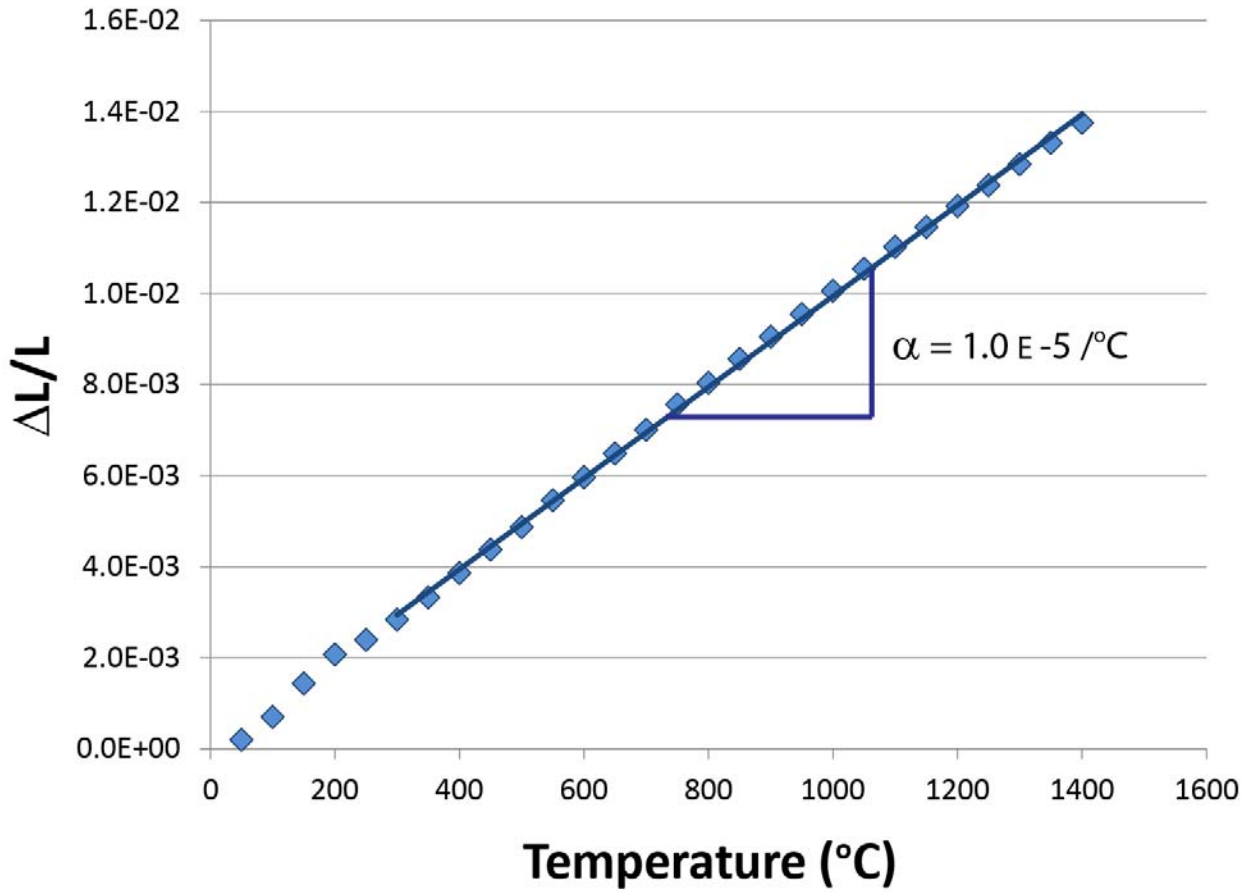

Figure 63: Linear expansion of $Sm_2Zr_2O_7$ via HTXRD.